Development of Microfluidic Platforms for Electric Field-Driven Drug Delivery and Cell Migration

Maryam Moarefian

Dissertation submitted to the Faculty of
Virginia Polytechnic Institute and State University
in partial fulfillment of the requirement for the degree of

Doctor of Philosophy
in
Mechanical Engineering

Danesh K. Tafti, Co-Chair
Luke E. Achenie, Co-Chair
Caroline N. Jones
Rafael V. Davalos
Jiangtao Cheng
Rui Qiao

May 7, 2020

Blacksburg, Virginia

Keywords: Electric Field, Microfluidics, Drug Delivery, Cell Migration

Development of Microfluidic Platforms for Electric Field-Driven Drug Delivery and Cell Migration

ABSTRACT

Recent technologies in micro-devices for investigation of functional biology in a controlled microenvironment are continually growing and evolving. In particular, electric-field mediated microfluidic platforms are evolving technologies that have significant applications in drug delivery and cell migration investigations. Although drug delivery has had several successes, in some areas, it continues to be a challenge; in recent years, the positive impact of electric fields is being explored. The primary objectives of the dissertation are to design, fabricate, and employ two novel microfluidic platforms for drug delivery and cell migration in the presence of electric fields. Description of iontophoretic carboplatin delivery into the MDA-MB-231 triple-negative breast cancer cells and investigation of neutrophil electro taxis are two main aims of the dissertation. Transdermal drug delivery systems such as iontophoresis are useful tools for delivering chemotherapeutics for tumor treatment not only because of their non-invasiveness but also due to their lower systematic toxicity compared to other drug delivery systems. While iontophoresis animal models are commonly being used for the development of new cancer therapies, there are some obstacles for precise control of the tumor microenvironment's chemoresistance and scaffold in the animal models. We employed experimental and computational approaches, the iontophoresis-on-chip and the fraction of tumor killed mathematical model, for predicting the outcome of iontophoresis treatment in a controlled microenvironment. Also, precise control over the cell electromigration is a challenging investigation which we will address in the second aim of the dissertation. Here, we developed a microfluidic platform to study the consequences of DC electric fields on neutrophil electromigration (electrotaxis), which has an application of directing neutrophils away from healthy tissue by suppressing the migration of neutrophils toward pro-inflammatory chemoattractant.

Development of Microfluidic Platforms for Electric Field-Driven Drug Delivery and Cell Migration

GENERAL AUDIENCE ABSTRACT

Recent technologies in the micro-scale medical devices for diagnosis and treatment purposes are continually growing and evolving. Microfluidic platforms are reproducible devices with the dimensions from tens to hundreds of micrometers for manipulating and controlling fluids. In particular, electric-field mediated microfluidic platforms, are developing technologies that have significant applications in drug delivery and biological cell directional movement investigations. Although drug delivery has had several successes, in some areas, it continues to be a challenge. In recent years, the positive impact of electric fields is a significant advancement in drug delivery techniques. Transdermal drug delivery systems such as iontophoresis are useful tools for delivering chemo drugs for tumor treatment not only because of their sensitivity but also to their lower systematic toxicity compared to injection or oral drug delivery. While iontophoresis animal models are conventional for the development of new cancer therapies, there are some obstacles to precise control of the tumor scaffold in the animal models. We also developed a novel microfluidic platform to study the consequences of DC electric fields on white blood cells' (WBC) directional movement, which has an application of directing WBC away from healthy tissue by suppressing the damage of WBC accumulation in healthy organs.

Acknowledgment

I would like to express my special appreciation and thanks to my advisors Dr. Danesh Tafti and Dr. Luke Achenie and to my mentors Dr. Caroline Jones and Dr. Rafael Davalos. I also want to thank the Department of Mechanical Engineering at Virginia Tech, the Department of Biological Science at Virginia Tech, Mary V. Jones graduate fellowship, and Virginia Tech Initiative to Maximize Students development (VT-IMSD) NIH traineeship, Dr. Edward Smith, for the financial support during my studies. I would like to thank you for encouraging my research and for allowing me to grow as a research scientist. I would also like to thank my committee members, Dr. Jiangtao Cheng, Dr. Rui Qiao, for serving as my committee members even though they are busy. I also want to thank you for letting my defense be an enjoyable moment, and for your brilliant comments and suggestions, thank you. I would especially like to thank my colleagues in the Jones Lab, Nidhi Menon, and Udaya Sree Datla, who has always been available to help me in the experiments. A special thanks to my family. Words cannot express how grateful I am to my parents for all of the sacrifices that they have made on my behalf. Your prayers for me were what sustained me thus far. I would also like to thank all of my siblings, who gave me the self-confidence to strive toward my goal without fear.

TABLE OF CONTENTS

LIST OF FIGURES

LIST OF TABLES

LIST OF SYMBOLS

ϕ (J/C) Electrical potential

$\hat{\phi}$ Dimensionless electrical potential

$\vec{\nabla}\,(1/m)$ Gradient operator

$\hat{y}$ Dimensionless transverse rectangular coordinate

$y\,(m)$ Transverse rectangular coordinate

$y_k(m)$ Rectangular kill distance

$H\,(m)$ Half distance between two blood vessels

ϕ_1 (J/C) Electrical potential at $y = H$

ϕ_2 (J/C) Electrical potential at $y = -H$

α Ratio between electrical potentials on the vessel walls

C_D(mol/m^3) The molar concentration of drug

$\hat{C}_D$ The dimensionless molar concentration of drug

C_{D0}(mol/m^3) Concentration of the drug in the blood vessel

t (sec) Time

$\vec{N}_D$(mol/$(m^2 s)$) Total molar drug flux

R_D(mol/$(m^3 s)$) Uptake of the drug by the tumor cells

$D\,(\mathrm{m}^2/\mathrm{s})$ Drug diffusion coefficient

z Charge number of the drug

$F\ (\mathrm{C/mol})$ Faraday's constant

$m\left((\mathrm{mol}\times\mathrm{m})/(\mathrm{N}\times\mathrm{s})\right)$ Drug mobility

$I\ (1/s)$ The cellular uptake rate of the drug

$\vec{\nabla}\bullet(1/m)$ Divergence operator

$\nabla^2\ (1/m^2)$ Laplacian operator

p Relates α the electric potential ratio to Pm_1

q Ratio between the uptake rate of the carboplatin and diffusivity

Pm_1 The ratio between the electric potential and diffusivity

BVF Blood volume fraction

$V_{\mathrm{Total}}\ (m^3)$ Total tumor volume served by blood vessels

$f_{\mathrm{kill}}\left(\mathrm{mol/m^3}\right)$ The fraction of tumor cells killed in the control volume

$f_{\mathrm{kill}}^{\mathrm{M}}\left(\mathrm{mol/m^3}\right)$ The fraction of tumor cells killed in a monolayer cytotoxicity experiment

$V_{\mathrm{Tumor}}\ (m^3)$ Tumor volume served by a single blood vessel

$N_{\mathrm{bloodvessels}}$ Number of blood vessels in the tumor region

$V_{\mathrm{SingleBloodVessel}}\ (m^3)$ Volume of a single vessel

$V_{\mathrm{bloodvessels}}(m^3)$ Volume of blood vessels in the tumor region

r $(\mathrm{kg/m^3})$ Density

T (K) Temperature of the control volumes

$\vec{E}$ (N/C) Applied electric field

CHAPTER 1

Introduction

1.1. Electro transport

Electro Fluid Dynamics (EFD), also known as Electro Hydro Dynamics (EHD) or electrokinetics, is the study of fluid motion under the influence of electric fields. The motion of charged molecules or particles in a fluid is proportional to an applied electric field. Electrophoresis and electroosmosis of charged macromolecules are general frameworks for the transfer of charged species in the fluid flow. In electromigration, size and charge characterization of species play an essential role in the dominancy of electrophoresis and electroosmosis phenomenon. Electroosmosis flow appears in the migration channel due to an electrostatic double layer on the surface of the channel. The charged drug molecule solute transport in the neutral solvent can create an electrostatic double layer on the migration channel's surface. However, in the absence of surface charge and flow in the channel, the electrophoresis movement of the drug molecule is a dominant phenomenon in drug electromigration. Biological cells are more massive than drug molecules. Therefore, another electrostatic double-layer appears on the surface of the polarized cells in the electrolyte solvent, which causes cells electrophoresis movement due to the electrophoretic retardation force on the cell's surface. In the mixture of cells with various sizes, the electrophoretic retardation force creates the separation of the cells [1, 2].

1.1.1. Iontophoresis of charged molecule in an electrolyte solution

Iontophoresis is the transdermal drug delivery by applying an electric field gradient on the skin. The electric field increases the permeability of drug barriers by

electrophoresis [3] and the electroosmotic movement [4, 5] of drug ions. Common cancer electrotherapies such as electrochemotherapy are based on the electroporation phenomenon that increases the porosity of cell membranes by changing their integrity using high-intensity AC electric fields. But recent cancer electrotherapy, iontophoresis treatment, is drug ion delivery via drug electromigration through the skin using the DC/AC electric field and carrier ion electric current. Carrier ions are ions in the bloodstream and electrolyte solution in iontophoresis patches. The electroporation side effects include the disorganization of the stratum corneum, the toxicity induced by pH changes, and decreased viability of healthy tissue. However, iontophoresis can give a better result and fewer side effects by protecting the integrity of the stratum corneum for accessible solid tumors such as breast cancer by using a low-intensity electric field and low drug dosage [6].

The iontophoresis process occurs through three different mechanisms [7]: 1) the ion-electric field interaction provides electrophoretic movement of ions and drives ions out of the blood vessel or endothelial membrane [3, 6]; 2) flow of electric current pass the ions through the membrane pores and voltage-gated ion channels [4, 8]; and 3) electroosmosis produces bulk motion of the solvent itself that carries ions or neutral species [4, 5, 7]. A fundamental, mechanistic understanding of the underlying physical phenomena governing tumor response to interstitial electroosmotic flow and electrophoretic movement of the chemotherapeutics remains elusive. We develop a computational model based on fundamental principles to describe electrical field effects on chemotherapeutics and validate the model with the proposed *in vitro* experiment. The microfluidic experiment is designed for the more realistic and physiologically

relevant condition for bio mimicking three-dimensional iontophoresis drug delivery into the breast tumor by using tumor cell distribution in a heparin-based hydrogel [9].

1.1.2. Cell Migration

Cell migration is an essential cellular event that has an application in biological processes such as wound healing and cell isolation. The electric field gradient is a physical stimulus of cell migration in cellular events. In fluid dynamics, the living cells in the human blood are playing the role of particles inside a carrier fluid. By a related exogenous or endogenous DC electric field, two phenomena occur [10, 11] 1. Intracellular electromigration [8] (electrophoresis and electroosmosis) of ions inside the cell membrane induced by the structural polarity of biological cells. 2. Extracellular electromigration (electrophoresis [12] and electroosmosis) of ions inside an ionized carrier fluid, induced counter-charges on the polarized cell's surface. The movement of these charged cells occurs due to electrophoresis and electroosmotic flow of the carrier fluid (bloodstream). Recently, a novel microfluidic platform was used for quantifying the migration of biological cells, such as neutrophils, under the influence of chemoattractant concentration gradients [13]. However, neutrophil electrophoresis and electromigration has not been addressed yet in recent literature.

1.2. Drug Delivery Model

Ani-cancer drug delivery into solid tumor tissue is a complex process and embraces different spatial and temporal scales. Drug interstitial transport into the dense extracellular matrix (ECM) of the tumor microenvironment (TME) hinders the efficacy of chemotherapy. Multiscale mathematical models can discover ways to increase the efficacy of drugs by penetrating the tumor tissue. We refer the reader to find the power

of the mathematical and biophysical model in several review papers [14-21]. *In silico* simulations are well-suited for testing different physical mechanisms that can enhance the distribution, advection/diffusion, uptake, and reaction of drugs in the tumor region. These models are mostly used for *in vitro* experiments, design, and parameter optimization. Chemotherapy is one of the most commonly used treatments of breast cancer in the last stage of tumor progression. Physiological and biological barriers not only decrease the efficacy of chemical compounds but also delay the compounds from reaching all tumor cells in concentrations necessary to produce a therapeutic effect. The chemotherapeutic agents are often used in combination with other drugs of different pharmacokinetic properties or with other anti-cancer treatments [22] such as electrochemotherapy and iontophoresis to overcome tumor microenvironment drug resistance. However, a validated multiscale model that can be used for tumor response prediction to chemotherapy and DC electric field on drug delivery has not been studied yet. We approach this drug delivery model using analytical and computational models and *in vitro* microfluidic. Drug delivery and control requires interdisciplinary research that requires multiscale models and experiments [23] (**Figure 1.2.1**). State-of-the-art in current interdisciplinary research includes 1. Analytical and Computational Models: (a) Microscale: Computational fluid dynamics model for predicting electric field intensity. (b) Macroscale: Analytical fraction of tumor killed model to predict the outcome of enhancing drug delivery by applying electric fields. 2. Microfluidics Model: iontophoresis-on-chip for controlling: tumor size, tumor type, drug type, drug dosage, drug delivery depth, electric field intensity, electric current intensity, and electrophoresis

movement of ionized drug for enhancing drug delivery. 3. New biomaterial: using heparin-based hydrogel as novel material for representing ECM porosity.

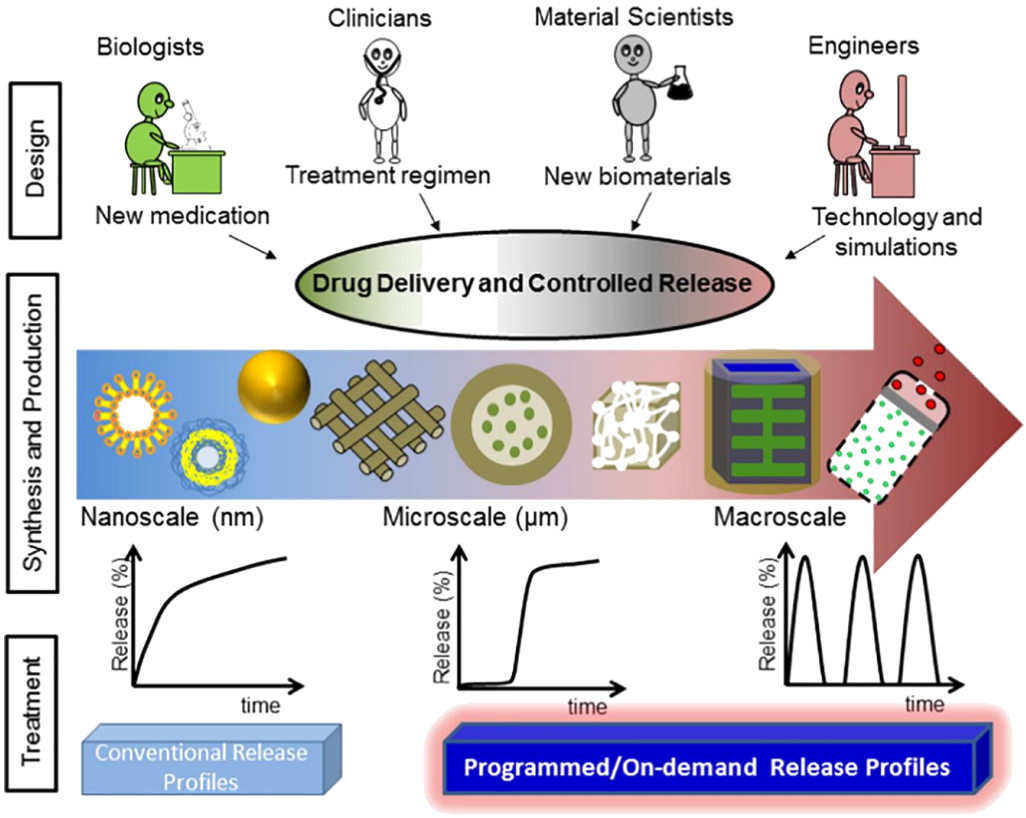

Figure 1.2.1. Drug delivery and control requires interdisciplinary research. Reprinted from Publication "Drug delivery systems for programmed and on-demand release, Vol. 132, Pooya Davoodi et al., Advanced Drug Delivery Reviews, Pages No. 104-138, Copyright (2018)", with permission from Elsevier [23]

1.2.1. Analytical and Computational Models

Predicting drug release in biological tissue has an enormous clinical and industrial potential in the field of pharmacology. Analytical models employ drug delivery mechanistic study for analyzing physical, chemical, and biological transport phenomenon quantitatively. The most crucial advantage of analytical models is predictive power based on real physics, which is better than empirical/semi-empirical

models [24]. These models facilitate the investigation of different physical, chemical, and biological phenomenon separately and recognize the dominant transport phenomenon in drug delivery. On the other hand, computational models can quantitatively analyze drug delivery mechanisms in complex spatiotemporal biological systems.

Researchers have modeled chemotherapy based on physical diffusion [25-27]. Built upon the work of Pascal et al. [28], it has been proven in the reported drug delivery model [29] that the electric field affects drug delivery enhancement. The linear function describing the fraction of cells killed in a monolayer (i.e., neglecting diffusive transport) experiment is detailed in Pascal et al. [28].

In the current study, we show the effect of electrophoretic transport on increasing cationic macromolecule concentration in a porous region using an *in-silico* model validated by an *in vitro* experiment. Then, we use the physics-based mathematical model [29] to perform a sensitivity analysis and parameter optimization to reduce the number of *in vitro* experiments.

1.2.2. Microfluidic (*in vitro)* Models

Microfluidics is the movement of fluids in microdevices with the dimensions of tens to hundreds of micrometers for processing a small amount of fluid (10^{-9} to 10^{-18} liters) [30, 31]. Previously, microfluidics was used as a designed tool for fluid mechanics modeling, theoretical study, and correlation to experimental results [32]. Conventionally, most published work on microfluidics includes microanalytical methods such as valves [33, 34], channels [35, 36], flow sensors [37], gas-phase chromatography (GPC) [38], high-pressure liquid chromatography (HPLC) [39], and

capillary electrophoresis (CE) [40, 41]. Fabrication of microfluidic devices in polydimethylsiloxane (PDMS) by soft lithography made microfluidics more accessible to chemists and biologists working on the benchtop for biomimicking *in vivo* conditions [42]. Soft-lithographic methods which are based on rapid prototyping and replica molding are faster and less expensive microfluidics fabrication methodologies. The accessibility and affordability of microfluidics open a window for various applications such as molecular analysis, clinical diagnosis [43], molecular biology, and microelectronics [30].

1.2.2.1. Organ-on-a-chip and drug delivery

Organ-on-a-chip systems mimic dynamic interaction of *in vivo* microenvironment using microfluidics. Screening the spatiotemporal cellular interaction *in vivo* microenvironment is problematic due to the complexity and uncontrollable nature of cellular and extracellular microenvironments [44]. Precise spatiotemporal control of human physiology, including mechanical, chemical, and electrical signals, is the unique feature of organ-on-a-chip systems. Organ-on-a-chip systems can be designed for a controlled microengineering environment with specific microarchitecture biomaterial for a diversity of applications including human (healthy or diseased organs) *in vitro* models for drug toxicity screening, development, and discovery [45]. For simulating the whole-body response to drugs, there is a need to design 3D biomimetic microfluidic devices emulating human physiological conditions. Human-on-a-chip or multi-organ-on-a-chip connect microscale cell cultures of multiple tissue types via fluidic channels to reproduce the interaction between them. On the other hand, combined multi-organ-on-a-chip (MOC) and pharmacokinetic-pharmacodynamic (PK–PD) model can be a useful

tool to get a more realistic result for drug screening and also have a controlled drug delivery system [46].

1.2.2.2. Three-dimensional cell culture

3D cell culture-based microfluidic devices have been previously reported, which enable the formation of cell spheroids in 3D to mimic the complexity of heterogeneous tumor tissue for cytotoxicity tests of anticancer drugs [9, 46-48]. Marimuthu et al. [49] developed a microfluidic platform for automatic multi-size spheroid formation with constant volume hanging droplets (HDs) from a single cell loading inlet.

A hydrogel vascular network was engineered by researchers to achieve the mass transfer physiological functions in organ-on-a-chip devices. Mu et al. [50] engineered a 3D vascular network in the hydrogel to mimic mass transfer through passive diffusion in a nephron. They fabricated two independents microchannels in the hydrogel, which is useful to perfuse solutions independently. The hydrogel network was fabricated using soft lithography and replicating techniques and was structure-controlled, mechanically stable, and cytocompatibility.

Using hydrogel for anti-angiogenesis drug screening was performed by Kim et al. [51]. They designed and fabricated a quantitative microfluidic angiogenesis screen (QMAS) to monitor and quantify cellular behavior under various drug concentrations. The device consisted of three compartments for mimicking the blood vessel, extracellular matrix, and tumor parts. The confluent endothelial cell (EC) monolayers and the VEGF-supplemented media in the conditioned media channels mimicked tumor cells *in viv*o.

The formation of the capillary network in the hydrogel to mimic the tumor angiogenesis is also the interest of many researchers. Wang et al. [52] developed an advanced 3D microvascular model by integrating vasculogenic and EC lining strategies on one novel microfluidic device. The device included a microenvironment conducive to vascular network development. The microvascular networks in the device had excellent vascular barrier properties and minimal leakage. Yeon et al. [53] described the formation of perfused capillary networks in microfluidic channels. To mimic the interstitial fluid in the regulated angiogenesis network Kim et al. [54] developed a 3D cell culture microfluidic device, which consisted of cell culture channel and the media channels. The device mimicked natural sprouting morphogenesis from the pre-formed microvascular network.

1.2.2.3. Tumor microenvironment on a chip

The second leading cause of death in the United States (US) is cancer, accounting for about 30% of deaths from ages 45 to 65. The global cancer epidemic is growing exponentially and is expected to reach 1,806,590 new cancer cases and 606,520 cancer deaths in the US, nearly 1,600 people per day in 2020 [55]. However, an overall decline of 29% in the mortality rates of the four leading cancers (lung, colorectal, breast, prostate) has resulted in nearly 2.9 million fewer deaths. This decline is due to advances in prevention, early detection, and treatment [56]. Despite significant advances in the prevention of cancer deaths, tumor resistance to chemotherapy is still responsible for chemotherapy failure in cancer treatment. Therefore, there is a need for a biomimetic microengineering platform to recapitulate tumor microenvironment drug resistance. Tumor microenvironment (TME) on a chip is a novel application of *in vitro* microfluidics for drug screening and delivery in human-relevant platforms (**Figure 1.2.2**).

Coculturing cells, generating chemokines, and cytokines gradients mimicking extracellular matrix heterogeneity has been achieved in previous microfluidic device studies [57, 58]. A previous study cocultured three tumor cell lines (SK-OV-3, MKN-74, and SW620) with primary fibroblasts in a biomimetic TME chemoresistance model for reconstituting simultaneous angiogenesis and lymph-angiogenesis on a 3D microfluidic platform [59]. Also, the tumor extracellular matrix was constructed by researchers on a chip for the study of cell invasion and cancer metastasis using hydrogel and other polymer-based biomaterials [9, 60-63].

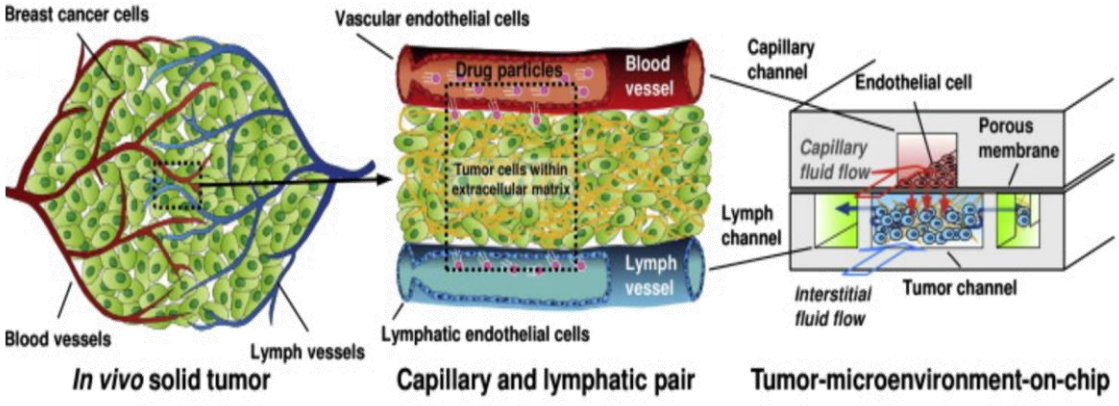

Figure 1.2.2. Tumor-microenvironment-on-chip mimics the 3D tumor vasculature on the microfluidic device for nanoparticle delivery. Reprinted from Publication “Simulation of complex transport of nanoparticles around a tumor using tumor-microenvironment-on-chip, Vol. 194, Bongseop Kwak et al., Journal of Controlled Release, Pages No. 157-167, Copyright (2014)”, with permission from Elsevier [64].

1.2.3. Application of models in clinics

Clinicians are using several methods for drug delivery: 1. Injectable delivery methods. 2. Orally disintegrating tablets. 3. Transdermal drug delivery using controlled-release technologies and localized release of the drug. 4. Targeted drug delivery using nanomedicine and targeted release of drugs to specific sites in the body.

Device assisted transdermal drug delivery [65] is the interest of the current study. Transdermal drug delivery devices use a combination of three main techniques: 1. Drug loaded patch for natural diffusion. 2. Actuated diffusion using electric field, heat, and ultrasound. 3. Drug penetration using microneedles or electroporation. The fourth generation of transdermal drug delivery is using wearable devices for monitoring body conditions, drug dosage, and cell signaling, and programming drug delivery accordingly.

1.2.3.1. Chemotherapy for triple-negative breast cancer

In 2019, out of 12.4% (1 out of 8) of US women diagnosed with invasive breast cancer, around 10-20% of diagnosed breast cancer were triple-negative breast cancer which is lack of three receptors (Hormone epidermal growth factor receptor 2 (HER-2), Progesterone receptors (PR), and Estrogen receptors (ER)), and around 15% of diagnosed triple-negative breast cancer were positive to HER-2 receptor [66]. Currently, the most commonly used treatment for triple-negative breast cancer is chemotherapy [67].

Triple-negative breast cancer is treated with primary chemotherapy in both early and advanced stages. Taxanes (e.g., paclitaxel) are standard chemotherapeutics for triple-negative breast cancer [68, 69]. The paclitaxel drug reacts with the microtubules in the MDA-MB-231 cancer cell and prevents their depolymerization. The mechanism of the reaction was first discovered in 1981 by Kumar [70]. Caplow et al. [71] reported on how to measure the microtubule affinity for paclitaxel. The detailed kinetics can be found in several references [72-74]. It is reported that combined or individual chemotherapy of taxanes drug and platinum-based drug (e.g., carboplatin) represent a potentially promising strategy for triple-negative breast cancer treatment [69, 75-78]. Cisplatin and

Carboplatin are common chemotherapeutic drugs in electrochemotherapy [79] and radiotherapy [80]. Carboplatin activation in cancer therapies was investigated theoretically and experimentally using carbonate buffer and cell culture medium, which contains carbonate and bicarbonate buffer [81, 82]. The final product of activated carboplatin contains *cis*- [Pt $(NH_3)_2(CO_3^{-2})$ (CBDCA-*O*)]$^{-2}$, a negative ion that is suitable for iontophoresis delivery of carboplatin by an applied electric field and an electric current is the interest of the current study.

1.2.3.2. Transdermal chemo drug delivery

Transdermal drug delivery (TDD) is the time-release of the drug through the skin inside the tissue [83, 84]. TDD has four generations [85] (**Figure 1.2.3**) : First-generation: Low-dosage and low-molecular-weight drug diffusion using patches/gel/spray, which is limited by the skin's first layer (stratum corneum). Second-generation: Drug actuated diffusion with external stimuli such as DC electric field (iontophoresis), heat (hyperthermia), and ultrasound through reversibly disturbing stratum corneum without damaging deeper tissues. Third-generation: Drug penetration with microneedles and AC electric field. It is based on delivering macromolecules such as therapeutic protein and vaccine across the skin with novel chemical enhancers, electroporation, cavitation ultrasound, microneedles, thermal ablation, and microdermabrasion [86]. Transdermal drug delivery has many advantages [87, 88], including (1) maintaining a constant drug concentration and eliminates frequent dosing administration and plasma level peaks and valleys, especially when long-term treatment is required, such as chemotherapy. (2) providing convenient, inexpensive, and pain-free self-administration for patients (3) avoidance of the first-pass metabolism and the acidic

environment of the stomach. All of these advantages are suitable for cancer patients who are exposed to chemotherapy for a long-term period. Third-generation transdermal chemo drug delivery, which is thermal ablation and electroporation, is electrochemotherapy cancer treatments used in clinics. However, second-generation transdermal chemo drug delivery, including iontophoresis, is still under investigation for clinical use [89-93].

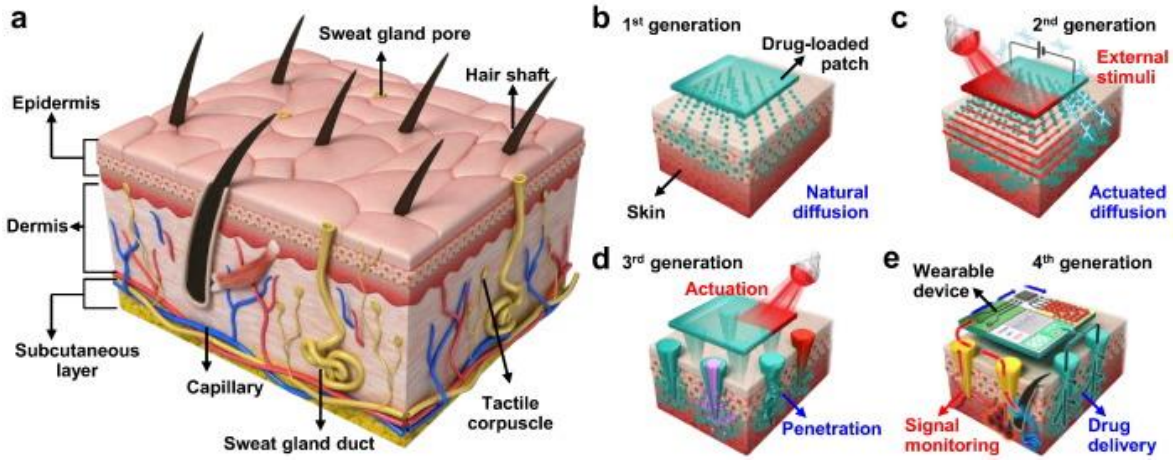

Figure 1.2.3. Generations of transdermal drug delivery. A. Skin schematic. B. The first generation of transdermal drug delivery is natural diffusion. C. The actuated diffusion with an external stimulus is the second-generation transdermal drug delivery. D. Drug penetration with microneedle combined with an actuated diffusion is the third-generation transdermal drug delivery. E. The fourth generation of transdermal drug delivery is the smart bandages for monitoring delivery conditions remotely, and it has been used for both diagnosis and treatment processes. Reprinted from Publication "Device-assisted transdermal drug delivery, Vol. 127, Hyunjae Lee et al., Advanced Drug Delivery Reviews, Pages No. 35-45, Copyright (2018)", with permission from Elsevier [85].

1.2.3.2.1. Electrochemotherapy

Electrochemotherapy is based on the principle of cellular membrane electropermeabilization using low-frequency and low amplitude AC electric field. Electropermeabilization of the membrane at the cellular level facilitates the intrinsic toxicity and cellular uptake of certain drugs such as netropsin and bleomycin with weak

diffusion through the plasma membrane [94-96]. In 2014, Kennedy et al. [97, 98] realized that the introduction of charged molecules to the cell surface would create regions of enhanced transmembrane electric potential in the vicinity of each charged molecule. Subsequently, the effect of the electroporation uptake kinetics of Propidium Iodide (PI) in HL60 human leukemia cells was investigated by Kennedy et al. [97, 98]. Sadik et al. [99] also quantified the electroporation-mediated transport mechanism of Propidium Iodide experimentally. They compared electroporation and electrophoretic types of transport, investigating the delivery of PI into 3T3 mouse fibroblasts. A monolayer of human cerebral microcapillary endothelial cells' (hCMECs) permeability cultured on a permeable polyester membrane was measured optically by the diffusion of fluorescent tracers in Bonakdar et al. [100, 101]. They indicated an increase in blood-brain barrier (BBB) permeability by disrupting hCMECs monolayer under pulsed electric field regimes (Low frequency (~1 Hz, 100 μs), high amplitude (~600 V, 1000 V, 2500 V cm^{-1})). High intensity pulsed electric fields may allow impermeable drugs to reach tumor microenvironment by disrupting the integrity of healthy tissue such as human epidermal membrane (HEM) and blood vessel endothelial membrane. More recently, iontophoresis transdermal chemo drug delivery via low-intensity electric fields has been reported in animal models [4, 102-104] and humans [90].

1.2.3.2.2. Iontophoretic chemotherapy

Iontophoresis mainly provides an electrical driving force for transport across stratum corneum and produces reversible skin permeability via electrophoresis, while weakly charged (**Figure 1.2.4**). Uncharged compounds can be moved by the electroosmotic flow of water generated by the preferential movement of mobile cations

(e.g., Na^+) instead of fixed anions (e.g., keratin) in the stratum corneum [4, 105, 106]. Because iontophoresis applies to some macromolecules up to a few thousand Daltons, it has a potential for delivering some cancer chemotherapeutics macromolecules that carry a charge without primarily changing the skin barrier itself. The most substantial advantages of iontophoresis chemotherapy are the ability to provide control over drug dosing, electrical current, and drug delivery modulation overtime for complex delivery profiles by a microprocessor or the cancer patient. However, the general disadvantage of iontophoresis is the maximum current—and, therefore, the maximum delivery rate—is limited by skin irritation and pain caused by the general inability of iontophoresis to localize its effects on the stratum corneum [88, 107]. The current study investigates Iontophoresis-on-a-chip, which gives better control over drug delivery rate, depth, and cell viability on application with electric fields for pre-clinical drug testing and screening.

Figure 1.2.4. Device assisted transdermal drug delivery in clinics. Reprinted from Publication "Device-assisted transdermal drug delivery, Vol. 127, Hyunjae Lee et al., Advanced Drug Delivery Reviews, Pages No. 35-45, Copyright (2018)", with permission from Elsevier [85].

1.3. Cell migration *in vitro* model

Cell migration plays a critical role in biological processes such as immune response to infection, wound healing [108-110], cell isolation, cell separation [111, 112], cancer metastasis [113-116], and immune-inflammatory responses [117]. Chemical gradients in tissue cause a chemical stimulus [118] (chemotaxis) for cell migration (**Figure 1.3.1**). The observation that cells can follow chemoattractant was first studied by scientists who discovered the mechanisms underlying the attraction of neutrophils to the sites of infection [118]. However, physical gradient in moisture [119-123] (hydrotaxis), light [124-127] (phototoxic), pressure [128, 129] (barotaxis), physical contact [130-132] (thigmotaxis), cellular stiffness [133-139] (mechanotaxis), cellular adhesion [140-143] (hepatotoxic), gravity [144-148] (geotaxis), fluid shear stress [149-153] (rheotaxis), magnetic fields [154-160] (magnetotaxis), and electric fields [8, 110, 161-203] (electrotaxis/galvanotaxis) are essential factors that also induce cell migration in tissue microenvironment. Physiological or externally applied direct current (DC) electric fields is a guiding mechanism for the orientation and directional movements of many cell types, such as fission yeast cells [204], Caenorhabditis elegans [120, 186, 194, 205], a pathogenic bacterium such as Pseudomonas aeruginosa, Escherichia coli, and Dictyostelium [166, 187, 200, 206]. Some cells migrate toward the cathode (e.g., neural stem cells [140, 161, 163, 183, 188, 202], fibroblasts [170, 179, 189], keratinocytes [192, 207-209], rat prostate cancer cells [210, 211], T lymphocyte [138, 174-176, 181], lung cancer cells [167, 169, 180, 193, 212], and many epithelial cell types [110, 185, 192, 197-199, 203, 213]), and other cells migrate to the anode (e.g., corneal endothelial cells [214], breast cancer cells [171, 196], glioblastoma [173, 182],

and human vascular endothelial cells [215, 216]). The directional movement of cells is due to an electrostatic polarity associated with cellular structure and cell-cell/cell-ECM interaction. Developmental polarity is observed along three axes, anterior-posterior, dorsal-ventral, and left-right in biological cells. Such polarities can be established by concentration gradients of secreted proteins and asymmetric organization of cellular components, such as the cytoskeleton [170, 217]. Investigation of biological cell electromigration in polymer-based microfluidics has been the interest of many researchers over two decades [218-220]. Most of these studies focused on separation, sorting, and isolation of cells [111, 112]. However, studying electromigration is an important factor in cell transport in the human body [134].

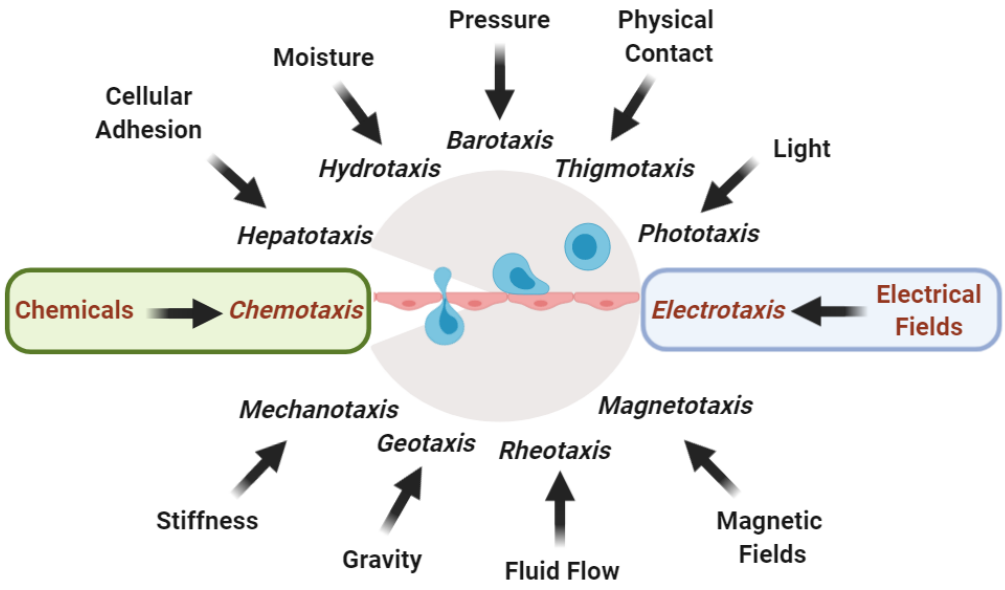

Figure 1.3.1. Phylogeny of migration induced by physical and chemical stimuli. Adapted from Ref. [221], Fig.1.

1.3.1. Chemotaxis

Boyden developed the first *in vitro* cell migration technology in 1962 [222]. In 1977, the Zigmond chamber improved the Boyden chamber by utilizing variations of a

millipore filter assay system and evaluating the migration of polymorphonuclear leukocyte toward fMLP chemoattractant [223]. Mimicking the blood vessels network to study blood circulation was considered by researchers in studying chemotaxis using blood-on-a-chip devices. The application of the blood-on-a-chip devices is the separation of the whole blood component for the functional assays and molecular analysis [224]. Adding branches of microchannels, gradient generators for increasing chemoattractant concentration gradient in cell migration assays is another advancement in microfluidics *in vitro* models [225, 226]. Time-evolving [227-229], high-throughput combinational [230-232], and steady-state [233-237] gradient generators have been developed.

The time-evolving gradient generator consisted of two reservoirs or compartments which are connected with the channel or a valve with no convection shear flow between the source and the sink compartments. The cells are cultured in the bridge or the compartment and migrate according to the concentration gradient. Abhyankar et al. [228] created a stable chemical gradient without fluid flow in a microfluidic device. This device contained a membrane-covered source region and a vast volume sink region connected by a microfluidic channel. The steady-state gradient generators facilitate the stable concentration gradient for long term investigation. Ye et al. [235] developed a high content screening device to measure the cellular response of human liver carcinoma to several drugs varying in concentration. The high-throughput combinational gradient generator facilitated monitoring dose and cellular responses in delivering the combinatorial mixtures of different chemoattractants. Liu et al. [232] fabricated three-dimensional microfluidic networks that were employed as a chip-based cell culture

device with an integrated combinatorial mixer. Due to the continuous laminar flow in the steady-state gradient generator, shear stress over the cells, and flushing away, potentially important cell-secreted factors could not be avoided [238]. Using the hydrogel in the cell culture chamber can reduce the effect of flow on cell deformation by stabilizing the cell growth environment. Recent developments in microfluidics chemotaxis assays make it even closer to *in vivo* models. Cell-cell interactions during chemotaxis [239], self-guidance of cells in migration maze [240-242], and 3D hydrogel migration channels [243] are recent improvements in chemotaxis on-chip models.

1.3.2. Electro-taxis

Cellular response to electric fields varies among cell types and the diverse experimental conditions. Cellular electrotactic behavior along the direction of the cathodal or anodal electric potential induced by cell polarity and alteration in the cellular signaling pathway [199, 244, 245]. Cell polarity plays an essential role in proper biological function. Siegrist et al. [246] showed that some cell-intrinsic cues such as microtubule cytoskeleton and asymmetric subcellular compartmentalization of proteins could induce cell polarity. Cell polarization with an applied electric field, extrinsic cue, is a cause of cell orientation and migration toward signaling of electrotaxis. The electrical polarization is due to several hypothetical mechanisms (**Figure 1.3.2**): 1. Electrophoretic redistribution of membrane components and a drag force from electroosmosis at the membrane. 2. Electro-osmotic forces at the membrane, attracting a mobile double layer at the cell surface to produce mechanical work and asymmetrically activate a force sensor for a local signal. 3. Electroosmotic blood flow and electrophoretic movement of blood ions also electrophorese membrane

components. 4. Asymmetric ion distribution on the cells' surface opens the voltage-gated ion channels.

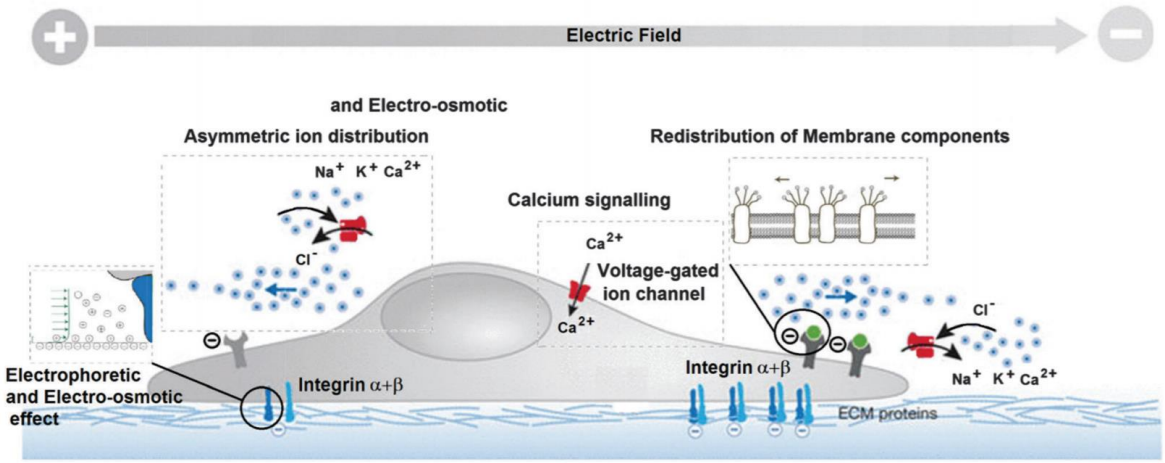

Figure 1.3.2. The visual schematization of a hypothetical mechanism by which cells respond to electric fields. Reprinted from Publication "Influence of electrotaxis on cell behavior, Cortese, Barbara, et al., Integrative Biology, Pages No. 817-830, Copyright (2014)", with permission from Elsevier [247].

These different mechanisms indicating the effects of electric fields on cellular electrotactic behavior are cell-specific. Thus, there is a need for cell electrotaxis experimental investigation on the cell-type basis. In 2004, Pu et al. showed the electric fields of 3 V/cm induced robust Golgi polarization and directional migration in epithelial cells. The wide array of studies of different cell types, cellular microenvironment, and electric field intensity utilized the use of microfluidics in electrotaxis investigation. The range of 0-5 V/cm electric field intensity was used in microfluidics electrotaxis by researchers [125, 177, 180, 181, 248-250].

To recognize *in vivo* complexity of neutrophil migratory pattern and decision-making is essential to recapitulate chemoattractant and electric field gradients more accurately *in vitro* experimental model. Measuring individual cell velocity and directionality *in vivo* requires precise control of tissue spatiotemporal microenvironment.

Microfluidic chemotaxis assay assists researchers to address neutrophil migration in spatiotemporally controlled chemo gradients [239-242]. Also, microfluidics electrotaxis assay has various advantages such as reduction of joule heating, facilitation of high through-put investigation, and precise control of electric fields, cells, and reagents [191]. Dual gradient microfluidic platform has been used to study neutrophil chemotaxis with coexisting pro-inflammatory and pro-resolution signals by previous researchers [251-253]. Researchers are interested in investigating the effect of co-existing chemotaxis and electrotaxis on cell migration [174]. Lymphocyte chemotaxis [249], electrotaxis [175, 181], and co-existing chemotaxis and electrotaxis [176] show the migration of T-cells toward the cathode. The study of T-cells migration suggested higher electrotactic attraction of T-cells toward cathode of DC electric fields in the presence of a competing CCL19 chemoattractant gradient. However, a microfluidic device for quantifying neutrophil time-dependent migration pattern and decision making with co-existing electrotaxis and chemoattractants (pro-inflammatory (LTB_4) and pro-resolution (fMLP)) has not been studied yet. In this study, we designed a novel four-sided microfluidic platform for studying neutrophils' migration decision making toward fMLP or LTB_4 in the presence of an electric field gradient. Recent microfluidics electrotaxis assays [167, 174-176, 178, 180, 181, 191, 192, 213, 250] used electric field intensity between (4V-20V) to reach the target of 0.4V/cm-4V/cm electric potential gradient for inducing cell electromigration in microchannels. The endogenous electric field experimentally measured in wound healing was 0.4V/cm-2V/cm, and many clinical trials reported a significant increase in the rate of wound healing from 13% to 50% [254]. On the other hand, exogenous electric fields of higher intensities used for transdermal drug delivery

[255], increase the permeability of cell membrane [256], and a therapeutic tool for restoring tissue integrity in severe injuries with the exogenous electric field of less than 4 V/cm.

1.4. Application of *in vitro* cell migration in Sepsis and ARDS clinical investigation

ARDS (Acute Respiratory Distress Syndrome) a respiratory disease due to the injured lung's alveolus that causes low blood oxygen. Lungs alveoli are tiny air sacs that take up oxygen from the breath and keep the body's metabolism active. In ARDS, fluid builds up inside the alveoli of the lungs, and the surfactant breaks down. Injured alveolus has damage to the bronchial epithelium, which cause the inflammatory response and activation of neutrophils inside the alveolus. Also, the inflamed endothelial cells on the damaged alveolus' blood vessel walls cause inflammatory migration of neutrophils inside. On the other hand, sepsis is the systematic inflammatory response of the immune system to infection. Sepsis is an autoimmune disorder, which is the most common cause of ARDS. Also, people with ARDS have a higher risk of developing infections, which are the trigger of sepsis autoimmune disorder. Both ARDS and sepsis cause damage to healthy organs and tissues due to environmental and genetic triggers, another disease, or a significant injury. In sepsis, cases are more complicated. Two competitive cases in sepsis are 1. Decreasing the inflammatory response of the immune system. 2. Preventing the excessive suppression of the immune system from keeping it healthy enough for fighting the infection. The first competitive case has been made for a pathogenic role of excessive immunity, the so-called 'cytokine storm in inflammation,' and the second competitive case has been made by anti-inflammatory, the immune

response through immunosuppressive or self-resolution [257]. Until recently, most clinical therapy on sepsis was focused on blocking the initial hyperinflammatory cytokine-mediated phase. Improved clinical treatments have resulted in surviving the first hyper-inflammatory phase and entering the second extended immunosuppressive phase. Deaths in this immunosuppressive phase are typically due to failure to control the primary infection or due to the acquisition of secondary hospital-acquired infections, often with opportunistic pathogens [258]. Recent studies provide a general view of the host-pathogen interaction and inappropriate inflammatory response. However, there is a lack of agreement as to the key to innate immune mechanisms [257]. Neutrophils are 60-70 percent of white blood cells and play an essential role in the innate immune mechanisms. The ability of microfluidics to facilitate precise control of the immune system microenvironment makes it an appropriate tool for studying the role of neutrophils migratory patterns in the immune-inflammatory response to infection. Loading patient samples in microfluidic assays and priming the device with a variety of chemoattractant can facilitate sepsis or ARDS clinical diagnosis in the future (**Figure 1.4.1**) [242].

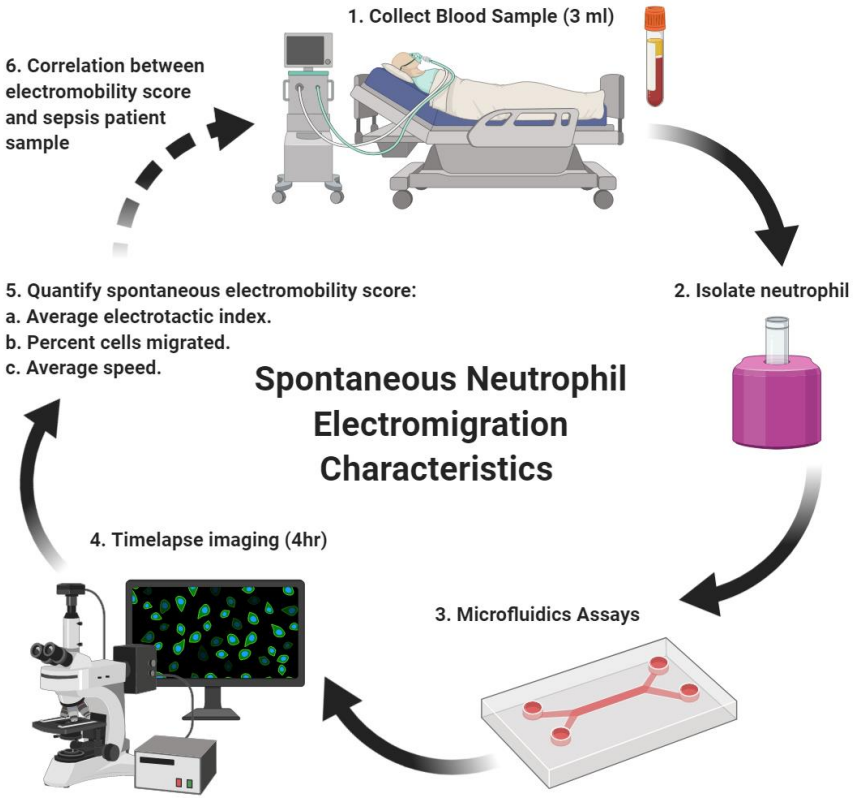

Figure 1.4. 1. Five steps of quantifying spontaneous neutrophil electromigration score for clinical diagnosis of sepsis. Adapted from Ref. [242], Fig. 1.

Immunotherapies can protect the body over an extended period without substantial toxicity in comparison with chemo or radiation therapies. Active immunotherapy stimulates the body's immune system to identify and target pathogens, while passive immunotherapy uses synthetic antibodies. The most significant obstacles in immunotherapy treatment are the optimization of vaccine clinical trials and the high costs. Microfluidics and mathematical models can be engineering tools for vaccine and drug optimization before a clinical trial. The ability of microfluidics to control the immune system microenvironment and facilitate cell-cell interactions make them more accurate tools for the active investigation of the body's immune system and potential testing immunotherapies for inflammatory diseases.

1.5. Dissertation overview

The current work aims to quantify, through mathematical modeling and microfluidics platforms, the effect of DC electrical field on iontophoretic carboplatin delivery and neutrophil migration toward chemoattractant gradient.

Carboplatin delivery investigation is obtained by modeling the concentration distribution of the chemotherapy drug, carboplatin, delivered transdermally, under the influence of the DC electric field with model validation using microfluidics *in vitro* experiments for four cases: (1) computational/*in silico* modeling of ionic macromolecule concentration profile in a porous medium with and without electrophoretic transport (2) validation of a computational model (case 1) with the *in vitro* microfluidic experiment. (3) continuum mathematical modeling of functions that predict the fraction of tumor killed obtained using the methods described in Pascal et al. [28, 29] based on concentration profiles of carboplatin delivery with and without DC fields. (4) validation of fraction of tumor killed model solved analytically (case 3) with microfluidics *in vitro* experiment.

Neutrophil migration study is conducted by two sets of *in vitro* microfluidic models: (1) studying the effect of electric field gradient on neutrophil migration by quantifying the neutrophil's electromigration pattern toward electric field signals. (2) studying the effect of co-existing chemokines and electric field gradient on neutrophil migration by quantifying neutrophils' electromigration pattern toward LTB_4 and fMLP.

While several simplifying assumptions compared to *in vivo* animal/human models (e.g., microfluidic 3D platforms mimic the *in vivo* cell systems in a simple manner, no electroosmotic flow and heat generation) were included in the models described here, this research builds a foundation in developing predictive *in vivo* and clinical models that

quantify chemo-delivery and immune system response to DC fields, which is currently absent in the body of work in this field. The application of electrical fields can also generate heat and electroosmotic flow within the tumor microenvironment and wound site that can enhance perfusion of chemotherapy drugs and neutrophil electromigration, among many other beneficial effects.

The mathematical model was built for the first time for predicting the outcome of iontophoresis cancer treatment. The microfluidic *in vitro* model (iontophoresis-on-chip, IOC) is the first *in vitro* approach of mimicking iontophoresis cancer treatment. However, both mathematical and microfluidics models should be improved to represent the *in vivo* microenvironment features. The IOC device has the capability of adding an epidermal membrane between two layers, and 3D cancer spheroids co-cultures with fibroblast inside the heparin-based hydrogel nourished by the epidermal growth factor. Some assumptions in mathematical modeling, such as neglecting electroosmotic transport, can be relaxed in future model development. The computational fluid dynamic model of electroosmotic flow and electroosmotic drag flow on the cellular membrane coupled with the mass transfer model has the application of modeling cell electromigration. The synergy between the mathematical model and the microfluidic experiment facilitates the simultaneous development of both techniques for mimicking novel biomedical devices for precision iontophoresis treatment. Future work can relax some of these assumptions to obtain more realistic results that can be applied to clinical investigation. The final chapter in this dissertation presents the conclusion and future application of our models on iontophoresis chemotherapy, sepsis electro-immunotherapy, smart bandage, and cancer immuno-iontophoresis chemotherapy.

CHAPTER 2

Iontophoresis increases carboplatin cytotoxicity in a microfluidic breast cancer model

2.1. Abstract

Iontophoresis employs low-intensity electrical voltage and continuous constant current to direct a charged drug into the tissue. Iontophoretic drug delivery has been recently used for cancer treatment *in vivo*. However, there is a strong need to control precisely and modulate the low-intensity electric fields in cell culture systems to optimize the physiology of iontophoretic drug delivery to tumors. Here, we present an iontophoresis-on-chip (IOC) platform to precisely quantify increases in electrically responsive carboplatin drug delivery and similar anti-cancer efficacy. In this study, a heparin-based hydrogel was used to model the extracellular matrix, and MDA-MB-231 triple-negative breast cancer (TNBC) cells were cultured as single cells in the microfluidic device. The transport of the drug through the hydrogel was modeled based on diffusion and electrophoresis of charged drug molecules in the direction of an oppositely charged electrode. The drug concentration in the tumor extracellular matrix was computed using finite element modeling of transient drug transport in the heparin-based hydrogel. The model prediction was then validated using the IOC platform by comparing the measured and predicted concentration of a fluorescent cationic dye (Alexa fluor 594®) with the molecular weight close to the TNBC gold standard drug, paclitaxel. Our results demonstrate that 50 mV DC electric field and 3 mA electrical current significantly increase drug delivery and the percent dead tumor cells by 48.12%±14.33 and 39.13%±12.86, respectively (n=3, p-value<0.05). The IOC platform and mathematical drug delivery model of iontophoresis may be promising tools for the precise delivery of chemotherapeutic drugs into solid tumors. Further improvements to the IOC platform can be made by adding a layer of epidermal cells to model the skin.

2.2. Introduction

Intravenous chemotherapy has been the traditional method of administering cytotoxic agents to cancer patients. Unfortunately, the maximum potential effect of these cytotoxic agents has been limited because of systemic toxicity and poor tumor perfusion. In an attempt to improve the efficacy of cytotoxic agents while mitigating their side effects, many groups report clinical use of electric fields to improve drug delivery. Iontophoresis, the technique delivers chemotherapy to select areas, reducing the risk of damaging healthy tissue by localizing the treatment.

2.2.1. Iontophoresis drug delivery using low-intensity electric fields

Employing electric fields to enhanced drug delivery for cancer treatment has been studied for decades. Most studies focus on cellular level electropermeabilization via high-intensity pulsed electric fields [94-96, 259-262]. Iontophoresis treatment is the drug delivery through the skin and blood vessel membrane using DC electric field and electric current [263-265]. Iontophoresis enhances drug delivery by electrophoresis, the movement of charged drug molecules in the tumor extracellular matrix surrounding tumor capillaries without disturbing the integrity of HEM, and changing the skin and blood vessel membranes permeability. During cancer treatments, iontophoretic devices are implanted proximal to the tumor or on the skin of the patient with external control of power and drug flow [7, 89, 266]. Iontophoretic delivery of chemotherapeutic drugs into the tumor microenvironment is still not well-defined [267, 268]. Iontophoresis enhances drug delivery by three mechanisms: 1) the ion-electric field interaction provides electrophoretic movement of ions and drives ions out of the blood vessel or endothelial membrane; 2) the electric field and flow of electric current increases permeability of the blood vessel

membrane; and 3) electroosmosis produces bulk motion of the solvent itself, which carries ions or neutral species, with the solution 'stream' [7]. To date, most *in vitro* [269, 270] and *in vivo* [271, 272] studies focus on the second mechanism, overcoming human epidermal membrane (HEM) drug resistance by using iontophoresis with a short electric field delivery duration. However, after passing HEM, controlled and predictable rates and distance of drug delivery in tumor extracellular matrix (ECM) using iontophoresis techniques are necessary. Physiological and biological barriers of ECM not only decrease the efficacy of chemical compounds but also delay the compounds from reaching tumor cells in concentrations sufficient to exert therapeutic effect [89, 90]. In our study, we set the flow rate to zero (eliminating mechanism 3) and focus on defining the first mechanism (electrophoresis) only. To model the iontophoresis, we need to define: 1) ECM porosity; 2) drug concentration; 3) cell density; 4) drug charge. In our model, we chose 70% porosity to represent the average blood vessel fraction *in-vivo* tumor [273, 274]. We set the drug concentration to less than the effective dose of 90% (ED90), which we measured in both the standard well plate and microfluidic device (**Fig. S.1A**). In our study, we change cell density (single cells vs. spheroids). We also compare an ionized drug [81, 82] (carboplatin) to the gold standard non-ionized drug (paclitaxel).

2.2.2. Drug delivery and a fraction of cells killed mathematical model

In this prospectus, we aim to reduce the number of microfluidics experiments by merging mathematical models with *in vitro* experiments. The mathematical model enables us to eliminate trial and error associated with experimentally adjusting parameters such as DC electric field intensity. Anti-cancer drug delivery into the solid tumor tissue is a complex process and embraces different spatiotemporal scales. Continuum models are

mostly used for the *in vitro* design of experiments and parameter optimization. Continuum physics-based models can also help researchers to define ways to use existing drugs more efficiently in the multiscale environment of the tumor. Drug interstitial transport into the dense extracellular matrix (ECM) and tumor microenvironment hinder the transport process [14-21, 275]. Computational/*In silico* simulations are well-suited for testing combinations of various physical laws (e.g., diffusion and electrophoresis) for finding drug concentration profiles in the tumor region. Researchers have modeled chemotherapy based on physical diffusion laws [25-27]. Kim et al. [276] reviewed the spatiotemporal mathematical model and application of models in predicting drug distribution inside cancerous tissue for overcoming drug delivery bio barriers for treatment optimization. They also discussed methods of validating mathematical models with experimental data to provide a better understanding of drug transport processes. Drug delivery into solid tumor tissue is a complex process and embraces different spatiotemporal dynamics. Interstitial transport into the dense extracellular matrix (ECM) and tumor microenvironment hinder the transport process [14-21, 275]. *In silico* simulations are well-suited for testing combinations of various physical laws (e.g., diffusion and electrophoresis) for estimating drug concentration profiles in the tumor region [25-27]. However, the fundamental mathematical model that incorporates the physics of electrophoresis transport is not well defined in previous studies. Based on the work of Pascal et al. [28], it has been demonstrated in the electrokinetics drug delivery model [29] that the application of the electric field enhances drug delivery in both micro and macro scales. However, a validated electrokinetics model [277] that can be used for the

prediction of tumor response to chemotherapy in the presence of an applied DC electric field has not been reported.

Carboplatin dosage in clinics is predicted using the Calvert formula [278]. Calvert formula formulated by glomerular filtration rate (GFR) and targeted area under the curve (AUC) reflected the concentration of carboplatin over time in the body that clinicians targeted for a specific patient. Several research studies questioned the accuracy of the Calvert formula in carboplatin dosage formulation [279, 280]. Application of computational fluid dynamic model for carboplatin dosage over time for a particular area under the curve prediction presented in a current study. Computational fluid dynamics (CFD) model predicts the concentration of carboplatin in the extracellular matrix over time and the percentage of decrease in time duration of reaching targeted dosage using the applied electric field. CFD model has an application in the prediction of carboplatin dosage in adjuvant cancer treatment. Many researchers have modeled chemotherapy delivery to tumors with and without electric fields. However, the fundamental mathematical model that incorporates the physics of electrophoresis transport is not defined well in previous studies. Based on the work of Pascal et al. [28], it has been proven in the reported drug delivery model [29] that the electric field affects drug delivery enhancement. However, validated pharmacokinetics and pharmacodynamics (PKDP) model [277] for tumor response prediction to chemotherapy and electric field and the special effects of applied DC electrical field on drug delivery has not been reported.

2.2.3. Three-dimensional tumor microenvironment in a microfluidic platform

3D cell cultures offer a bridge between the unrealistic 2D dish and the complex but difficult to control (and more expensive) animal model. 3D cell cultures, as compared to

2D, more closely mimic tissue and organ structure while allowing for more control, reliability, and reproducibility (e.g., for drug delivery), as compared to the animal model. Traditional 2D models consist of a flat, thin monolayer of cells and typically focus more on growth conditions, proliferation, and population [281, 282]. 3D cell cultures, on the other hand, allow for the study of dynamic processes (e.g., cellular migration, interactions, and metabolism) [281, 283]. Also, because of the unrealistic growth conditions in 2D cultures, cells tend to exhibit abnormal behavior, such as flattened shape, altered cellular responses, loss of differentiation [284, 285]. Protein and even genetic expression are different in 3D cultures from that in 2D cultures [281]. Spheroids grown in 3D models show more realistic growth patterns than the homogenous cell layer in 2D. 3D cultures also exhibit more excellent stability and longer lifespans and can be cultured for more extended periods than in 2D models, and also contributes to more realistic depictions of growth, pathology, and drug sensitivity [284]. For these reasons, much of the research has shifted to using 3D cell cultures in tumor modeling and drug delivery. While research done with 2D cultures improved insight into disease pathology and drug mechanism, the data is often not reproducible *in vivo* [281, 283, 284], with a 95% drug failure rate [286]. Microfluidic devices offer a wide range of uses in cell culturing, from growing single cells to tissues and even “organs on a chip [281].” Devices used for 3D cultures can range from simple to complex, allowing for a wide range of experimental conditions and procedures. Typical models for growing 3D cultures include growing spheroids on top of a matrix, within a matrix, and in a scaffold-free suspension [281]. Advances in microfluidic devices have significantly added to 3D cell culturing; these devices allow for precise control of the microenvironment (spatiotemporal aspects and chemical gradients) and can

more closely mimic in vivo physiological conditions (e.g., exhibiting laminar flow) [284]. Microfluidic devices are relatively cheap and require small amounts of precious biomaterial. They offer flexibility in design and experimental control, real-time analyses, and controlled co-culturing [286]. Microfluidic devices can also reduce shear stress (thus reducing cell damage), control spheroid size, and provide better oxygen supplies compared to conventional approaches [287, 288]. Typical challenges with microfluidic usage include the handling of such small quantities and sophisticated operational control and device design [286]. Mimicking the real biological systems using down to up approach can overcome these challenges. Down to up approach is about controlling a few parameters in a simple device, then modifying the device to achieve a real biological system in the *in vitro* model. Controlling the physics of drug transport phenomena is a unique application of a microfluidic device that facilitates precision drug delivery and adjuvant cancer treatment. The microfluidic platform is a manageable device for coupling with computational modeling of drug transport due to its capability of controlling the flow rate, electric field intensity, and drug concentration. In this study, we are explicitly considering controlling DC electric field intensity and drug concentration for electrophoresis drug delivery into the tumor spheroids and single cells. An appropriate and accurate microenvironment for spheroid growth is crucial for studying cellular interactions; inappropriate interactions between the cell and its microenvironment leads to aberrant cell behavior, as seen in tumor progression [289]. The microenvironment is composed of many types of cells such as immune cells, fibroblasts, endothelial cells, adipocytes, and the extracellular matrix (ECM) [290]. The ECM is made of fibrous proteins and proteoglycans with polysaccharide side chains [290, 291] and offers dynamic

structural support to organs, tissues, and cells. The ECM's function outside of support, such as influencing cell signaling behavior, adhesion, and serving as a growth factor reservoir [290], is not as well understood but holds many consequences for development, pathology, and drug treatments. ECM has also been shown to be a stem cell niche, playing a role in tissue homeostasis, development, and regeneration [283, 292]. ECM influences tumor cell proliferation and metastasis by blocking immune cells from reaching the tumor and by supplying tracts (fibers) for tumor cells to migrate elsewhere; it is known to affect the onset of angiogenesis as well as resistance to cell apoptosis, further contributing to the severity of tumor growth. ECM can also increase interstitial fluid flow, hampering effective drug delivery [290]. When modeling ECM for 3D cell culture, it is vital to capture all of its dynamic and complex functions. The material must be structurally supportive and conducive to cell growth and metabolism, allow for nutrient and gas exchange, and allow for cell signaling and other biochemical processes; Composition as well as geometrical (e.g., shape) [293] and mechanical (e.g., stiffness) aspects of ECM reproduced in vitro. For these purposes, various biomaterials have been employed to mimic ECM and provide scaffolding for spheroid formation [289], including hydrogels (cross-linked networks of hydrophilic polymer chains [294]) and nanofibrils [283]. Hydrogels can also respond to unique stimuli, such as pH and temperature, depending on its composition [295]. Hydrogels' classification is either natural or synthetic. Natural hydrogels, such as silk fibers, hyaluronic acid, collagen, agar, and fibrin, occur in ECM in vivo [289, 296]. A downside to using natural hydrogels is that their exact composition may vary between batches, and some of their properties (e.g., mechanical) are not well understood. Synthetic hydrogels, such as poly(acrylamide), poly(dimethylsiloxane), and

heparin-based hydrogel as compared to natural ones, are generally more reproducible, more easily manipulated and controlled [296], and offer more variability in chemical and mechanical properties [295]. Natural-synthetic hybrid hydrogels are also in use and offer the biocompatibility [289] of the natural hydrogel but the increased controllability of synthetic [296]. Recently, cancer research has taken to studying the effects of ECM and its role in chemoresistance. ECM proteins create a barrier around the tumor cells that block drug delivery. Many other aspects of the tumor microenvironment (TM), such as oxygen availability, acidity, and several stromal cells, also contribute to tumor growth and chemoresistance. Novel treatments target not only the tumor cells themselves but also the TM [297]. In this study, 3D cell culture in the heparin-based hydrogel was used to examine the ECM chemoresistance and overcoming the ECM drug resistance by the applied electric field. The tumor-microenvironment-on-chip (T-MOC) was developed by Kwak et al. [64] for drug delivery into a tumor microenvironment. They studied the effect flow in tumor capillaries, which was made by the endothelial cell membrane and interstitial flow in the tumor region on nanoparticle delivery enhancement. The upgraded microfluidic design in a current study has the facilitates optimization and controlling the spheroid size, drug concentration, ECM porosity, and iontophoresis drug delivery mechanism for precision drug delivery in cancer treatment.

Microfluidic technology has recently emerged as a promising tool to generate biomimetic tumor models. Microfluidic devices using pulsed electric field excitation for electroporation were studied over a decade [100, 101, 298, 299]. Morshed et al. [300] used low-intensity pulsed electric field excitation (20 V pulse-excitation with pulse-widths between 0.5 to 5s) for cell lysis and cell membrane electroporation. The low-intensity

electric field between 50-200mV was also used by Ionescu-Zanetti et al. [301] to deliver impermeable exogenous anionic fluorescent molecules Calcein (Invitrogen, MW=622) and Oregon Green Dextran (OGD, Invitrogen, MW=70,000) molecules into the single Hela cell post-electroporation. To our knowledge, this is the first time that a group has reported iontophoretic delivery of chemotherapeutic drugs on-chip.

Electrically-controllable drug delivery from polyelectrolyte hydrogels has been reported *in vitro* and *in vivo* [302, 303]. Although, to the best of our knowledge, this is the first time that a group has reported iontophoretic delivery of chemotherapeutic drugs on-chip. In our device, we validate the application of a 50-mV electric field to an ECM of 70% porosity in increasing drug delivery in the tumor's single cells (**Figure 2.2.1**). In this study, we vary the drug type (charge). In the future, our device can also vary flow, ECM porosity, cell density (single vs. spheroid), and the electric field intensity. Controlling the physics of drug transport phenomena in the presence of applied electric field is a unique application of microfluidic platforms that can facilitate iontophoretic delivery of chemotherapies *in vitro* and *in vivo*. In this study, we control low-intensity DC electric fields for electrophoresis drug delivery into the tumor's single cells. We quantify the effect 50mV DC electric field and 3 mA electric current on percent dead cells mathematically and experimentally using a mass transfer model and a microfluidic platform. The fabricated device (iontophoresis-on-a-chip) mimics the tumor extracellular matrix by MDA-MB-231 single cells in the heparin-based hydrogel, the lymph capillary (drug sink), and the blood capillary (drug source). In the current study, first, we used a physics-based mathematical model [29] for sensitivity analysis and parameter optimization to reduce the number of *in vitro* experiments. To prove the chosen electric field intensity 50mV from the sensitivity

analysis, we showed the effect of electrophoresis transport on increasing ionic macromolecule delivery in the heparin-based hydrogel. The results of macromolecule electrophoresis delivery validated a transient electrokinetics drug release computational model. Next, anionic drug delivery (carboplatin) into single cells was quantified using the iontophoresis on a chip device and a physics-based model, validated by an *in vitro* limiting case experiment (single cells case, capillary inside the tumor region). The overall physiology of the iontophoretic transdermal drug delivery into the tumor vasculature and the relevant drug delivery route to the tumor's single cells are shown in **Figure 2.2.1.**

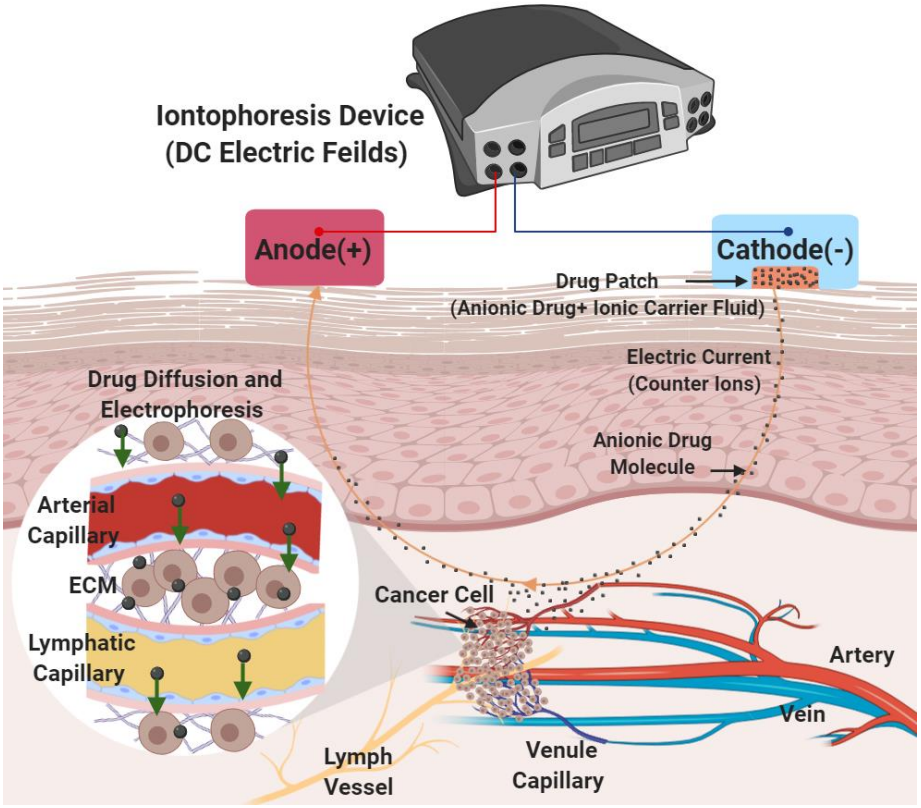

Figure 2.2. 1. Iontophoretic transdermal drug delivery into the tumor vasculature *in vivo* schematic shows the *in vivo* transport of anionic drug from the artery to the tumor from where it is eventually drained into the lymph vessel. Iontophoretic transdermal drug delivery includes insertion of the cathode along with the drug patch on the skin from where the anionic drug molecules move to the tumor facilitated by the transport of the counter-ions (from carrier solvent) to the anode.

2.3. Material and Methods

2.3.1. Design and fabrication of a microfluidic iontophoresis platform

The reported microfluidic device mimics the tumor vasculature by providing the top layer's drug source as arterial capillaries and two side channels in the bottom layer as lymph capillaries **(Figure 2.3.1A&B).** Sterile stainless-steel acupuncture needles with a diameter of 0.12 mm (Kingli, China) were used as electrodes to construct the DC electric field circuit. The layout of the layers composing the platform was drawn using CAD software (AutoCAD, Autodesk Inc.). Two layers of photoresist composed the culture chamber master mold: (i) The first layer consists of a central channel (1.5 mm wide) and has the role of supplying the media for cells, which were encapsulated in the bottom layer hydrogel; (ii) The second layer consist of a cell culture chamber with the dimension of 3X3 mm^2, two sink microchannels with the dimensions of 0.5X3 mm^2, two electrophoresis microchannels with the dimensions of 0.5X5 mm^2, and 15 ports for microchannel sinks with the dimensions of 0.15X0.15 mm^2. Master molds were fabricated in a cleanroom environment employing the conventional photolithography technique [304]. Briefly, the pattern of each layer was transferred on SU8-2100 photoresist (MicroChem, USA), previously spin-coated on 4". Silicon wafers. The device was washed with Phosphate Buffered Saline (PBS) after oxygen plasma bonding and then incubated for 10 minutes for remaining PBS evaporation to eliminate electroosmotic flow in a microchannel. Also, the hydrogel loading channel inlets were blocked by sterilized PDMS stoppers to exclude the gravitational flow effect in the microfluidic device. The percent two layers' microfluidic device was made of polydimethylsiloxane (PDMS) with a 10:1 mixing ratio of the monomer and curing agent (Sylgard 184, Dow Corning, MI). To fabricate the PDMS

layers, we first made a 350-400 µm thick molds of negative photoresist, SU8-2100, with the established soft lithography techniques. Replication molding was used to fabricate the microfluidic device using PDMS (polydimethylsiloxane) [305] (Sylgard 184; Dow Corning, Waltham, MA). PDMS pre-polymer was prepared by mixing the PDMS and curing agent with a 10:1 weight ratio. The PDMS prepolymer was then degassed in the desiccator and poured onto prepared silicon mold. We then poured the PDMS into the mold and cured it in the Thermoscientific oven (Heratherm OMS60) at 65°C for 6 hr. Next, we aligned two layers using the Nikon SMZ-1 stereo microscope. Then, I bonded two layers with oxygen plasma bonding. After bonding two layers, the inlets and outlets were punched using a 0.75 mm biopsy puncher. The bottom layer was bonded to the Pyrex glass using Nordson MARCH (AP-300) oxygen plasma bonding for mechanical stability then place on an 80°C hot plate for 45 min.

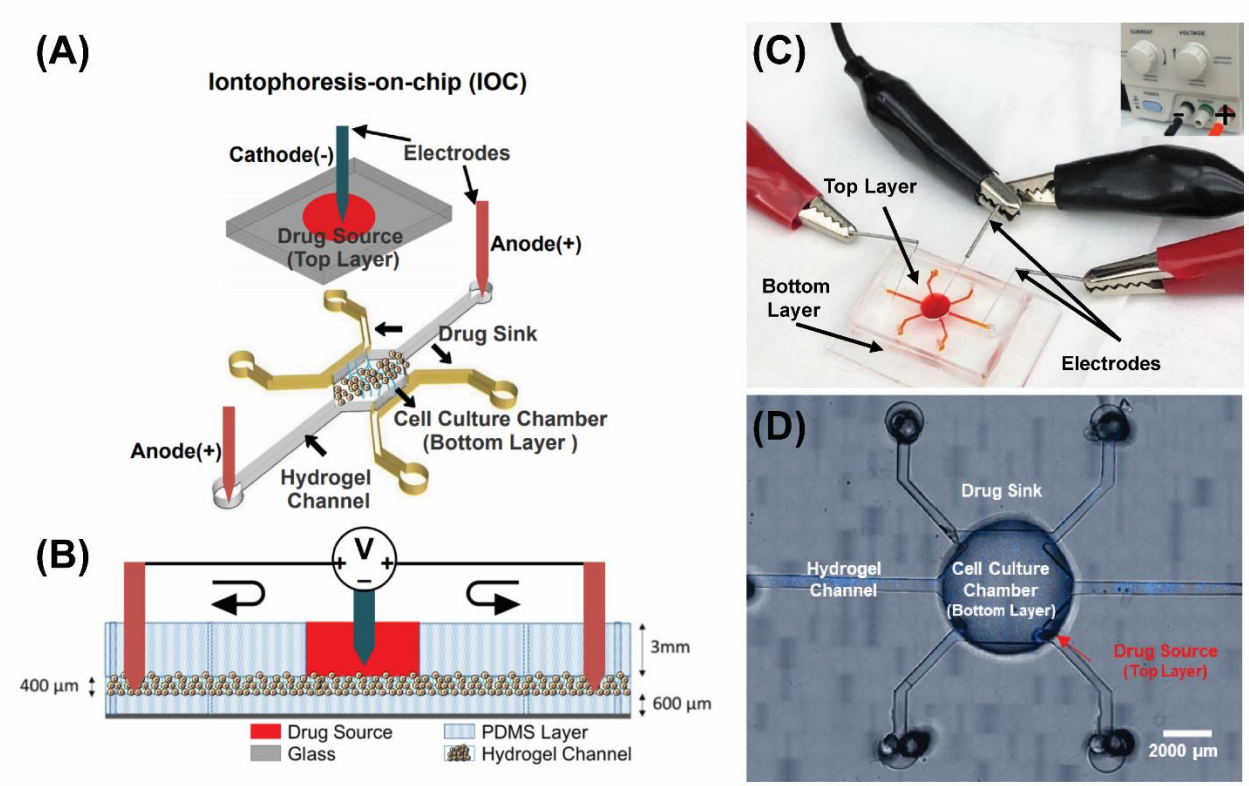

Figure 2.3. 1. Iontophoresis-on-chip (IOC) for quantifying iontophoretic delivery of chemotherapeutic drugs *in vitro*. (A) Microfluidic experiment setup, three-dimensional top view of the microfluidic device, negative electrode inserted in drug source well, and positive electrodes added to the bottom layer tumor region. **(B)** Side view of the open microfluidic device and the electric field circuit. **(C)** Image of the experimental setup and applying DC electric field for drug delivery from a top layer into the tumor region in the bottom layer. (**D)** Microfluidic device designed to measure iontophoresis drug delivery. The bottom layer includes 1) Drug sink. 2) Cell culture chamber for MDA-MB-231 cells (blue, Hoechst stain). 3) Electrophoresis channels for drugs to deliver from a cell culture chamber to side channels through electrophoresis and diffusion. The top layer is the drug source deliver from a cell culture chamber to side channels through electrophoresis and diffusion. The top layer is the drug source.

2.3.2. Hydrogel Polymerization

HyStem-HP Hydrogel Kit w/ PEGSSDA (ESI BIO GS315P) was used to prepare heparin hydrogel. The kit is composed of lyophilized solids of Heprasil® (thiol-modified sodium hyaluronate with thiol-modified heparin), Gelin-S® (thiol-modified gelatin) and PEGSSDA™ (disulfide containing polyethylene glycol diacrylate), as well as degassed deionized water (DG Water). Gels were prepared as per the manufacturer's directions.

Seeding density and drug concentration optimization experiments were done on 384 well-plates with 0.06 cm^2 growth area, which is approximately the growth area of the fabricated microfluidic device (0.09 cm^2) (**Figure 2.3.2 B**). We used 2.32 ml hydrogel volume and 14.4 ml cell medium volume for the 72-hour experiment. The drug was applied after 48 hr of incubation. The cells were stained using a live and dead cell assay (Abcam 115347) after 72 hours of incubation. Dose-response curves of paclitaxel and carboplatin were obtained using 10K cell density, a 30 microliter of heparin-hydrogel. The result from the dose-response curve of paclitaxel showed (11 nM) concentration is the effective paclitaxel dose 90% (EC90) and carboplatin dose-response curve showed (12 nM) concentration for the maximum fraction of cells killed (85%) (**Figure 2.3.2 A**). So, we chose (2 nM), which is less than an effective dose of 90% (EC90) for both chemotherapeutics drugs (paclitaxel and carboplatin) in the microfluidic *in-vitro* environment (**Figure 2.3.2 B**).

2.3.3. Cell culture and encapsulation in hydrogel

Human triple-negative breast cancer (TNBC) invasive ductal carcinoma cell line (MDA-MB-231, American Type Cell Culture HTB-26) were used in this study. Gibco™ Dulbecco's Modified Eagle's Medium F-12 (DMEM/F-12) containing high glucose and GlutaMAX™ supplemented with 10% (v/v) fetal bovine serum (FBS) and 1% (v/v) penicillin-streptomycin (100 units/ml penicillin and 0.1 mg/ml streptomycin) was used as a complete culture medium for MDA-MB-231 cells. The encapsulated breast cancer cell line MDA-MB-231 was studied using heparin hydrogel in complete media (DMEM + 10% FBS+1% P/S). For cell encapsulation, the cell pellet was resuspended in the Heprasil, Gelin-S mixture before adding the PEGA cross-linker with the density of 10K in 30 microliters of the hydrogel. Working Paclitaxel (sigma) and Carboplatin (sigma)

concentrations are (2 nM), which have around 71% of cells killed without applied electric field (**Figure 2.3.2 A**). We used cells on top of the gel, and encapsulating cells inside the gel methods for 3D cell culture in the microfluidic device. The encapsulated cells in the hydrogel were introduced into the device through manual injection using a syringe and tubing until a uniform distribution of cells was attained in the cell culture chamber.

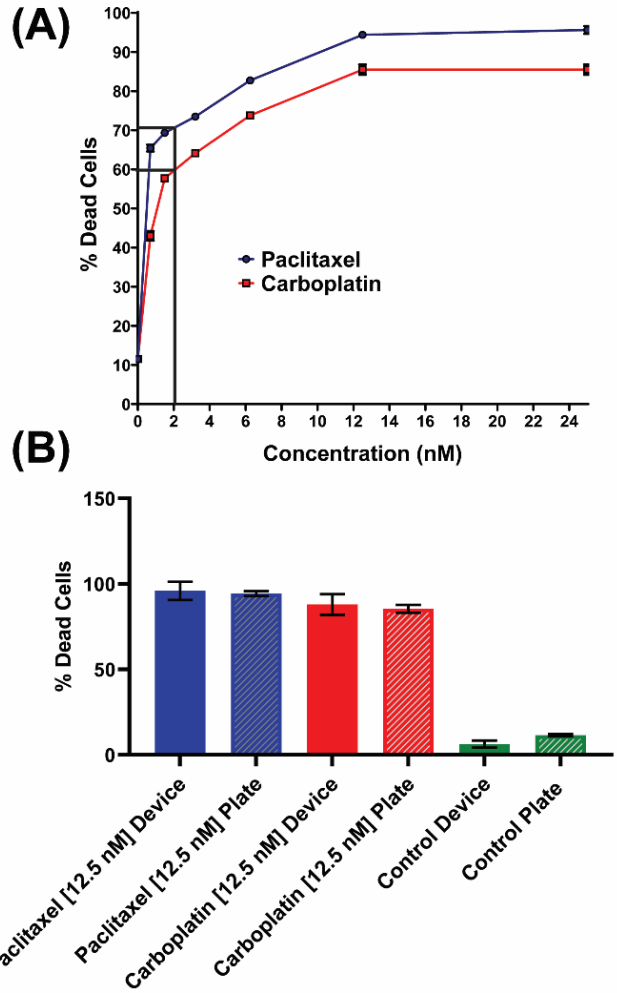

Figure 2.3. 2. Optimal chemotherapeutic drug concentration for hydrogel drug delivery. **(A)** Dose-response curve of carboplatin and paclitaxel for seeding density of 20K cells in 30 µl heparin-based hydrogel. **(B)** The graph shows the consistency in percent dead cells using 12.5 nM paclitaxel and carboplatin treatments in both microfluidic *in vitro* experiment and 384 well-plates.

The experiment was conducted for a total of 72 hours, where the cells were initially seeded and allowed to grow for 48 hours and then treated with drug [2 nM] and electric field (50 mV) for about 5 hours. The electric field was discharged after 5 hours; however, the cells are left in the drug solution for an additional 19 hours. Finally, the cells were stained with a live-dead cell stain (Abcam 115347) at the end of 72 hours of initial cell seeding.

2.3.4. Electrokinetics and mass transfer model

There is a strong need to control precisely and modulate low-intensity electric fields in cell culture systems to more accurately model and optimize the physiology of drug delivery observed *in vivo*. For reducing the number of *in-vitro* experiments, we employed a physics-based model for predicting the minimum electric field intensity to affect the maximum fraction of cells killed by simulating the effect of iontophoresis on carboplatin delivery. The model prediction is validated with a biomimetic three-dimensional microfluidic experiment by comparing the measured and predicted percentage of dead cells.

Laplace's equation was used to describe the potential electric field and electrophoretic transport in the system under study.

$$\nabla^2 \varphi = 0 \qquad (1)$$

where $\varphi$is electric field potential. By simplifying equation (1) in Cartesian coordinates, assuming the blood vessel is long (i.e., 5000 µm) in the x-direction (**Figure 2.4.2 B**), the applied electrical field varies in y-direction.

$$\frac{d^2\varphi}{dy^2} = 0, \qquad (2)$$

where y is the transverse coordinate. In dimensionless form, equation (2) becomes,

$$\frac{d^2\hat{\varphi}}{d\hat{y}^2} = 0, \tag{3}$$

where$\hat{y}$is dimensionless transverse coordinate, $\frac{y}{H}$, $\hat{\varphi}$ is the dimensionless electrical potential $\frac{\varphi}{\varphi_2}$ where φ_1 is electrical potential at $y = H$ and φ_2 is electrical potential at $y = -H$. Boundary conditions for equation (3) are described mathematically by Dirichlet conditions of known electrical potentials on the vessel walls. In the future, using the Neumann boundary condition instead of the Dirichlet boundary condition gives us a more realistic model to mimic the minimum natural concentration at the blood vessel membrane. Solving equation (3) with these boundary conditions leads to a linear function for the electrical potential within the tumor bounded by two blood vessels:

$$\hat{\varphi} = \frac{\alpha-1}{2}\hat{y} + \frac{\alpha+1}{2}, \tag{4}$$

where α is the ratio between electrical potentials on the vessel walls and is a dimensionless parameter, $\frac{\varphi_1}{\varphi_2}$.

For finding the drug concentration profile over time in the tumor extracellular matrix, we used the molar species continuity equation [306]:

$$\frac{\partial C_D}{\partial t} = -\vec{\nabla} \bullet \vec{N}_D, \tag{5}$$

where C_D is the molar concentration of drug, $t$is time, $\vec{N}_D$ is the total molar drug flux. Under the assumption of no convection, the total molar flux is equal to the summation of contributions due to diffusion and the applied electrical field:

$$\vec{N}_D = -D\vec{\nabla}C_D + zF\mu C_D\vec{\nabla}\varphi, \tag{6}$$

where D is the drug diffusion coefficient, z is the ionized carboplatin valence, F is Faraday's constant [1], μ is the carboplatin mobility. By combining equations (5), (6):

$$\frac{\partial C_D}{\partial t} = D\nabla^2 C_D - zF\mu\vec{\nabla}\cdot\left(C_D\vec{\nabla}\varphi\right). \quad (7)$$

Equation (7) was solved computationally using the finite element method in the COMSOL Multiphysics® v. 5.4 (COMSOL, Inc., Stockholm, Sweden). The computational domain is the electrophoresis channel (**Figure 2.4.2 A).** The diffusion coefficient of macromolecules is calculated using the Stokes-Einstein equation [307]:

$$D_{Dye\_water} = \frac{9.96\times10^{-16}T}{\mu_{water}(V_{Dye})^{1/3}}, \quad (8)$$

where V_{Dye} is the fluorescent dye molar volume, *T* is the solution temperature, and $\mu_{water}$is water viscosity. The effective diffusion coefficient of fluorescent dyes in the heparin-based hydrogel is used for the estimation of the effective diffusion coefficient of the drug in the extracellular matrix (ECM). Johansson obstruction model [308] for the effective diffusion coefficient of gels is used in the current study:

$$D_{effe} = D_{Dye\_water}\, exp(-0.84\beta^{1.09}), \quad (9)$$

where β is effective radius defined in equation (10):

$$\beta = (1-\varepsilon)(\frac{r_s+r_f}{r_f})^2, \quad (10)$$

where ε is heparin hydrogel porosity which is 70 percent, r_s fluorescent dye molecular radius, and $r_f$is a heparin hydrogel fiber radius.

The concentration profile of carboplatin in the tumor microenvironment was calculated using a mass transfer model. An additional term models the uptake of the drug into the tumor cells in the continuity equation. To describe the transport of carboplatin

from the blood vessels into the surrounding cancer cells, the control volume (**Figure 2.4.1 A**), we use the molar species continuity with reaction term:

$$\frac{\partial C_D}{\partial t} = -\vec{\nabla} \cdot \vec{N}_D + R_D, \tag{11}$$

where R_D describes the uptake of the drug by the tumor cells. We assume the drug uptake is governed by first-order kinetics,

$$R_D = -\lambda C_D, \tag{12}$$

$$\lambda = \frac{D}{L^2}, \tag{13}$$

where $\lambda$is the cellular uptake rate of the drug. By combining equations (6), (11), and (12):

$$\frac{\partial C_D}{\partial t} = D\nabla^2 C_D - zF\mu\vec{\nabla} \cdot \left(C_D \vec{\nabla}\varphi\right) - \lambda C_D. \tag{14}$$

Equation (14) is a microscopic equation of carboplatin transport in the tumor, assuming uptake, diffusion, and electrophoresis transport are present. For finding the drug concentration in a steady-state condition, one-directional transport, and dimensionless form, equation (14) becomes,

$$\frac{d^2\hat{C}_D}{d\hat{y}^2} - p\frac{d\hat{C}_D}{d\hat{y}} - q\hat{C}_D = 0, \tag{15}$$

where $\hat{C}_D$ is the ratio of the local concentration of carboplatin in the tumor tissue and that in the blood vessel (source), $\frac{C_D}{C_{D0}}$. Boundary conditions for solving ordinary differential equation analytically [309], equation (15), are specified concentrations equal to the concentration of drug in the blood on the blood vessels walls, the boundaries of the system under study:

$$\hat{C}_D(\hat{y} = 1) = 1, \tag{16}$$

$$\hat{C}_D(\hat{y} = -1) = 1, \tag{17}$$

solving equation (15) with these boundary conditions leads to:

$$\hat{C}_D = \frac{sinh(m_2)}{sinh(m_2 - m_1)} e^{m_1 \hat{y}} + \frac{sinh(m_1)}{sinh(m_1 - m_2)} e^{m_2 \hat{y}}\ , \tag{18}$$

For predicting percent of dead cells using a mathematical model, we present the novel physics-based model. The model is based on the fraction of cells killed in the monolayer surrounded one blood vessel. The linear function describing the fraction of cancer cells killed in a monolayer (i.e., neglecting diffusive transport) experiment is detailed in Pascal et al. [28]. Moarefian et al. [29] upgraded a model by adding diffusive and electrophoresis transport. The volumetric average of this function was used to determine the fraction of cells killed over the area of the tumor between two blood vessels (drug source) **(Figure 2.4.1 A)**.

In the current study, Pascal et al.'s approach for predicting the fraction of tumor cells killed in a monolayer is modified for Cartesian coordinates:

$$f_{\text{kill}} = \frac{2 \cdot l \cdot w}{V_{\text{Total}}} \cdot \int_{H - y_k}^{H} f_{\text{kill}}^{M}(C_D(y)) \cdot dy, \tag{19}$$

where H is half the distance between two blood vessels or the height of the control volume **(Figure 2.4.1 A)**. Where y_k is the killed distance from the center of control volume between two blood vessels to the tumor region surrounded one blood vessel l is the rectangular control volume length, $w$is the rectangular control volume width, $f_{\text{kill}}^{M}(C_D(y))$ is the fraction of cells killed in a monolayer cytotoxicity experiment.$C_D(y)$ is the local concentration of the drug. V_{Total} is the total volume of the rectangular domain surrounded one blood vessel,

$$V_{\text{Total}} = \frac{V_{\text{Tumor}}}{N_{\text{bloodvessels}}} = \frac{V_{\text{Tumor}}}{V_{\text{bloodvessels}}} \times \frac{V_{bloodvessels}}{N_{\text{bloodvessels}}} = \frac{1}{\frac{V_{\text{bloodvessels}}}{V_{\text{Tumor}}}} \times \frac{V_{\text{bloodvessels}}}{N_{\text{bloodvessels}}} = \frac{V_{singlebloodvessel}}{\frac{V_{\text{bloodvessels}}}{V_{\text{Tumor}}}} = \frac{V_{singlebloodvessel}}{BVF} \quad (20)$$

whereV_{Tumor} is the tumor volume, $N_{\text{bloodvessels}}$number of all blood vessels in a tumor, BVF is blood vessel fraction which is the volume of all blood vessels to the tumor volume, and $V_{\text{bloodvessels}}the$ volume of blood vessels in the tumor region, which is the tumor's void volume responsible for drug supply (**Figure 2.4.1 A**). In this study, BVF is 0.7. By combining (19) and (20), we obtain:

$$f_{\text{kill}} = \frac{2BVF}{H} \bullet \int_{H-y_k}^{H} f_{\text{kill}}^{M}(C_D(y)) \bullet dy \quad (21)$$

Assuming a linear function describing the fraction of cancer cells killed in a monolayer, fraction of cells killed in the rectangular case studied:

$$f_{\text{kill}}^{M}(C_D(y)) = f_{\text{kill}}^{M}(C_D(H)) \cdot \frac{C_D(y)-C_D(H-y_k)}{C_D(H)-C_D(H-y_k)}, \quad (22)$$

where $C_D(H)$ or C_{D0} is the concentration of drug in the blood vessel (maximum drug concentration and $C_D(H-y_k)$ or $C_{Dk}$is the concentration of drug at the kill depth (minimum drug concentration). Equation (21) in the dimensionless form:

$$f_{\text{kill}} = 2BVF.\int_{1-\hat{y}_k}^{1} f_{\text{kill}}^{M}(C_D(\hat{y})).d\hat{y},$$

(23) where $\hat{y}_k$is the dimensionless killed distance from the blood vessel wall, $\frac{y_k}{H}$. $\hat{y}$is dimensionless position $\frac{y}{H}$.

Based on the work of Moarefian et al. [29] in rectangular coordinate and modifying control volume and boundary conditions, a function for a fraction of cells killed for the rectangular case is obtained using equations (18),(22), and (23):

$$f_{kill} = 2BVF.f_{kill}^{M}(C_{D0})\frac{m_2\,sinh(m_2)(e^{m_1}-(1+m_1\hat{y}_k)e^{m_1(1-\hat{y}_k)})+m_1\,sinh(m_1)(e^{m_2}-(1+m_2\hat{y}_k)e^{m_2(1-\hat{y}_k)})}{m_1m_2(sinh(m_2-m_1)+sinh(m_1)e^{m_2(1-\hat{y}_k)}+sinh(m_2)e^{m_1(1-\hat{y}_k)})}$$

(24)

where m_1 and $m_2$are:

$$m_1 = \frac{p+\sqrt{p^2+4q}}{2}, \quad (25)$$

$$m_2 = \frac{p-\sqrt{p^2+4q}}{2}, \quad (26)$$

where$p = \frac{zF\mu}{2D}(\varphi_2 - \varphi_1) = Pm_1(1-\alpha)$,$q = \frac{\lambda H^2}{D}$, and $Pm_1 = \frac{zF\mu\varphi_2}{2D}$. The roots of m_1 and m_2 are always real because (q) is always positive. Three non-dimensional numbers relate to the physics of uptake, diffusion, and electrophoresis drug transport. Pm_1 is the ratio between the electric potential and diffusivity, q is the ratio between the uptake rate of the carboplatin and diffusivity, and p relates α the electric potential ratio to carboplatin diffusivity.

2.3.5. Drug delivery model optimization and sensitivity analysis

Sensitivity analysis of the electric field potential at blood vessel wall between 0 and 70mV showed 43.01 mV as the optimum electric field intensity to obtain 79 percent fraction of cells killed. Independent variables of the mathematical model described in equation 22 are shown in **Table 2.3.1.**

Table 2.3. 1. The fraction of cells killed model independent variables

Independent variable	Symbol	Value
Carboplatin mobility [310]	$m\left((\mathrm{mol}\times\mathrm{m})/(\mathrm{N}\times\mathrm{s})\right)$	$5.1\mathrm{X}10^{-10}$
Carboplatin diffusion coefficient [310]	$D\ (\mathrm{m}^2/\mathrm{s})$	$6.1\mathrm{X}10^{-6}$
Carboplatin bulk density [311]	$\rho\ (\mathrm{kg/m}^3)$	18.01
The cellular uptake rate of carboplatin[312]	$I\ (1/s)$	91.66
Tumor depth	$H(m)$	0.0004
Faraday's constant [1]	$F\ (\mathrm{C/mol})$	$9.65\mathrm{X}10^{5}$
Carboplatin valence [81]	z	2

The dependent variables used for sensitivity analysis of the analytical solution are shown in **Table 2.3.2** with their sensitivity range and the optimal values for obtaining the maximum fraction of cells killed. Three non-dimensional numbers and electric potential in the tumor region were optimized using GRG (Generalized Reduced Gradient) nonlinear solver [313]. The optimal value of φ_2 (electric field intensity) was instrumental in eliminating multiple microfluidic *in-vitro* experiments for electric field intensity optimization.

Table 2.3. 2. The fraction of cells killed model dependent variables and optimization

Dependent variable	Definitions	Sensitivity range	Optimized value (f_{kill} max)
$\boldsymbol{q}$	$\frac{\lambda H^2}{D}$	0.1-50	14.2
$\boldsymbol{Pm_1}$	$\frac{zF\mu\varphi_2}{2D}$	0-6	3.47
$\boldsymbol{\alpha}$	$\frac{\varphi_1}{\varphi_2}$	0.01-100	50.00
$\boldsymbol{\varphi_2}$		0-70 mV	43.01 mV

2.3.6. Transports of macromolecule into the heparin-based hydrogel

The first setup experiment was used to find the ionized fluorescent dye concentration profile with and without applying 50mV/cm DC electric field for finite element modeling validation. We loaded heparin-based hydrogel in the bottom layer, closed the outlets to eliminate gravitational flow, placed the device under a Nikon TiE time-lapse microscope, and allowed the hydrogel to solidify (10-15 min). 30 µl of dye was added to the top layer, and live imaging was started simultaneously. Live images were taken every 1 minute for 5 hours in two 1 mm^2 x-y planes in well and channel with a distance of 1.2 mm. The fluorescence intensity was measured over 10 different depths (40 µm) within the hydrogel (400 µm). The average intensity is the average intensity of over 1 mm^2 x-y plane. The final average intensity is the average of x-y plane intensities in 10 different hydrogel depth. For converting average dye intensity to dye concentration, the calibration curve was used (**Figure 2.3.3**). The experimental result of Alexa fluor 594® concentration versus time validated the finite element model of dye concentration (diffusion and electrophoresis delivery with 50mV/cm electric potential gradient) in the hydrogel porous region.

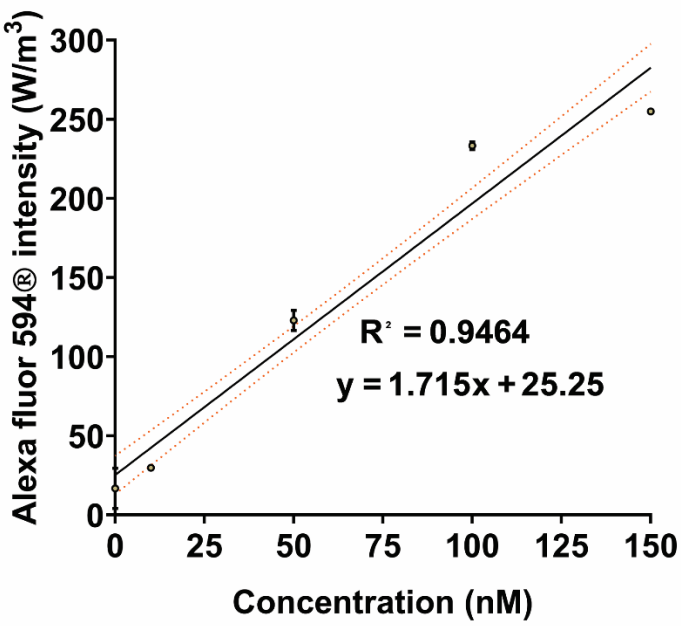

Figure 2.3. 3. Alexa fluor 594® calibration curve. The graph shows the linear regression between dye intensity and dye concentration.

2.3.7. Confocal microscopy and image processing

Confocal microscope (ZEISS LSM 880 with Airyscan) fitted out with a ZEISS Axiocam 503 mono camera, and the computerized stage was used to take fluorescent images. The microscope was controlled using the ZEN software (Carl Zeiss Microscopy GmbH, Germany). Images were processed in ImageJ (NIH, Bethesda, MD). The change in intensity over hydrogel depth was then acquired in several planes in the 3D cell culture chamber. The fluorescent light intensities from FITC (green) and TRITC (red) were adjusted in ImageJ to calculate the fraction of cells killed or the percentage of dead cells. The percentage of dead cells was obtained by dividing the number of dead cells (red) to that of the total number of cells (red + green) in each x-y plane along hydrogel depths.

The confocal microscopy setup was used to measure the maximum fraction of cells killed with and without applying the 50mV DC electric field to quantify the effect of

electrophoresis delivery of carboplatin for maximizing cells percent dead. Results from the confocal images were used for a fraction of cells killed model [29] validation (**Figure 2.4.4 C**). We processed the entire experiment (n=3) in five days, each n processed in three days. Three days' experiment procedure includes cell culture, apply drug and electric field, and staining (**Figure 2.3.4**).

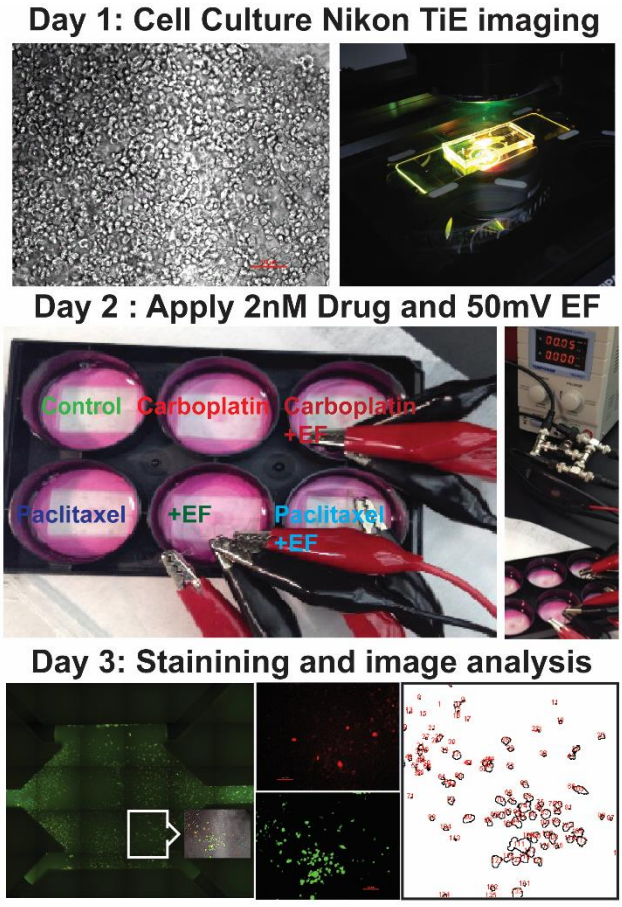

Figure 2.3. 4. Microfluidics drug delivery experimental procedure

2.3.8. Microfluidics *in-vitro* experiment statistical analysis

Statistical analyses were performed using Prism version 8.1.2 (332) software (GraphPad Software, La Jolla, CA) with a confidence level of $\alpha = 0.05$. Two-way analysis of variance (ANOVA) was used to test for differences in the number of dead cells after

electrophoresis treatment (n= 3). When results of ANOVA were significant, Tukey post hoc comparisons were used to examine differences among treatment groups. Data are presented as arithmetic mean ± SD.

2.4. Results and Discussion

The combined mathematical and experimental approach includes five steps. First, we used a physics-based mathematical model [28] sensitivity analysis and parameter optimization to reduce the number of *in vitro* experiments. Second, we showed the effect of electrophoresis transport on increasing cationic macromolecule concentration (Alexa fluor 594®) in the porous region (heparin-based hydrogel) using *in-silico* model validated by a microfluidic *in-vitro* experiment. Third, the iontophoresis-on-a-chip device was used for carboplatin and paclitaxel deliveries into MDA-MB-231 single cells using a 50mV electric field (EF) and 3mA electric current. Fourth, the *in-vitro* experimental results were used to validate the fraction of cells killed model. Finally, encapsulated spheroids in heparin-based hydrogel were exposed to carboplatin iontophoresis delivery using the iontophoresis-on-a-chip device.

2.4.1. Model optimization and sensitivity analysis

Conducting any experiments generate a large body of numbers and parameters. A thoughtful presentation of experimental results helps to render them concisely and understandably. The advantage of dimensional analysis is reducing the number of variables we need to investigate in the experimental design. Three non-dimensional numbers and electric potential in the tumor region were optimized using GRG (Generalized Reduced Gradient) nonlinear solver [313].

The first non-dimensional number. $Pm_1 = \frac{zF\mu\varphi_2}{2D}$ is the ratio between the electric potential and the diffusion coefficient. We consider the problem of maximizing fraction of cells killed function subject to varying non-dimensional numbers. Pm_1 is the function of electric potential in the tumor region. Except for φ_2, other terms in Pm_1 are constant properties of carboplatin. At large Pm_1 (3.47), the electric potential φ_2 has the highest value (43.01 mV); therefore, the fraction of cells killed is maximized (79%) (**Figure 2.4.1B**). The results show the positive effect of electric potential on the fraction of cells killed that could overcome the limitation of the low diffusion coefficient of the carboplatin. As Pm_1decreases, the fraction of cells killed decreases due to a decrease in φ_2. When Pm_1 is zero, the result indicates the fraction of cells killed (37%) without applying electric fields.

The direction of electrophoresis can be opposite to the direction of drug diffusion. The second non-dimensional number is α which is the ratio of electric potential in the drug source to the electric potential in the tumor. The fraction of cells killed decreases when α is close to 1, i.e., when there is no electric potential gradient. Therefore, $a=1$ $\left(f_1 = f_2\right)$ the fraction of cells killed is minimized (44%) (**Figure 2.4.1C).** As α increases $\left(f_1 > f_2\right)$, the electrical potential gradient is in the opposite direction to the concentration gradient, so the fraction of cells killed decreases. Note that $\alpha = 1/50$ means f_2 is 50 times more than f_1 at which the fraction of cells killed is maximized (79%).

The non-dimensional number is analyzed to examine the fraction of cells killed based on drug uptake rate and diffusion. q is the ratio of the drug uptake rate to drug diffusion. Since q is always positive, the model always increases (monotonic) with different values of positive q. At small q values (0.16), the carboplatin diffusion dominates over the uptake

rate. High carboplatin diffusion can occur due to a decrease in tumor drug uptake rate. Therefore, the number of cells killed at high carboplatin uptake (q=14.2) leads to a maximized fraction of cells killed (55%) and a decrease in tumor drug resistance **(Figure 2.4.1D)**. When q is smaller (0.16), the uptake rate of carboplatin (carboplatin consumption) is slower than carboplatin diffusion (carboplatin penetration), so the fraction of cells killed has the lowest value (2.5%). The fraction of cells killed is not going to be larger than a certain amount by increasing the value of q which depends on the properties of the drug. Therefore, applying an electric field to enhance chemotherapy delivery is essential to get the maximum fraction of cells killed (79%). The model investigated diffusion and electrophoresis drug transport into single cells. Increasing the electric field intensity increase the fraction of cells killed; however, new physics of transport such as joule heating and electroosmotic flow should be added to the model for an accurate prediction.

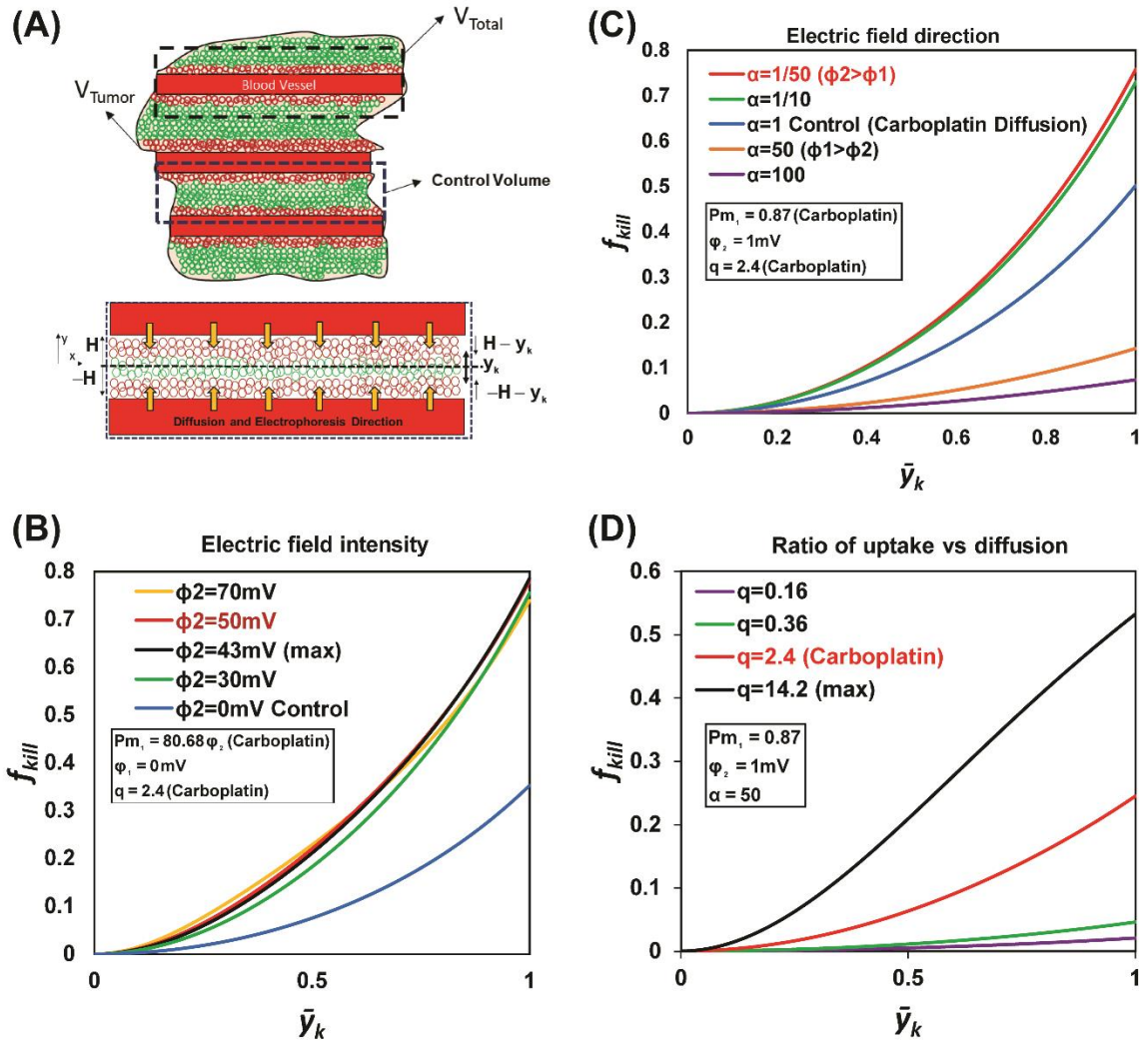

Figure 2.4.1. Mathematical model sensitivity analysis of the fraction of tumor cells killed model. (A) The schematic illustrates the volume of the analytical domain under study (V_{Total}), which is a sum of the volume of a single blood vessel and the surrounding tumor mass (V_{Tumor}). V_{Tumor} includes both the live and the dead tumor cells, represented by the green and red circles, respectively. $V_{control}$ depicts the volume between two consecutive blood vessels and is used as the control volume for the mathematical model, with idealized system boundaries ($H, -H, H - y_k, -H - y_k$). **(B)** The graph shows the variation in the fraction of tumor cells killed (f_{kill}) over a dimensionless kill distance y_k, for different values of Pm_1 and electric field intensities. The sensitivity analysis predicted 43 mV as the optimum electrical voltage required for maximizing the fraction of tumor cells killed (0.79). **(C)** The graph shows the variation in the fraction of tumor cells killed (f_{kill}) over a dimensionless kill distance y_k, for different values of α (which is the ratio of electric potential in the drug source (f_1) to the electric potential in the tumor (ϕ_2)). When ϕ_2 is 50 times more than ϕ_1, the diffusion and electrophoretic movement of the charged drug molecules are in the same direction, and the fraction of tumor cells killed is maximum (0.75). (**D)** The graph shows the variation in the fraction of tumor cells killed (f_{kill}) over a dimensionless kill distance y_k, for different values of *q* (the ratio of the drug uptake rate to the drug diffusion). For carboplatin *q*=2.4, where the fraction of cells killed is 0.25.

2.4.2. Delivery of cationic fluorescent dye into the hydrogel using the low-intensity electric field

Sensitivity analysis and electric potential gradient optimization show 43.01 mV electric potential resulted in the maximum fraction of cells killed (70%-80%). Based on mathematical model sensitivity analysis, we used 50 mV electric field intensity for drug delivery experiments on single cells and spheroids. Finite element modeling and validation of macromolecule transport in the hydrogel was computed. To examine our hypothesis using a 50mV electric field in a transient condition. Alexa fluor 594® cationic dye diffusion and electrophoresis delivery were investigated in 3 hours' experiment, and transient continuum mass transfer model. The *in-silico* simulation and *in-vitro* experiment proved an increase in average dye intensity by applying a 50mV electric potential gradient in the electrophoresis microchannel (**Figure 2.4.2 A**)**.** The finite element model of concentration profile in the microchannel was validated with an *in-vitro* experiment of Alexa fluor 594® cationic dye diffusion and electrophoresis delivery (**Figure 2.4.2 C**)**.**

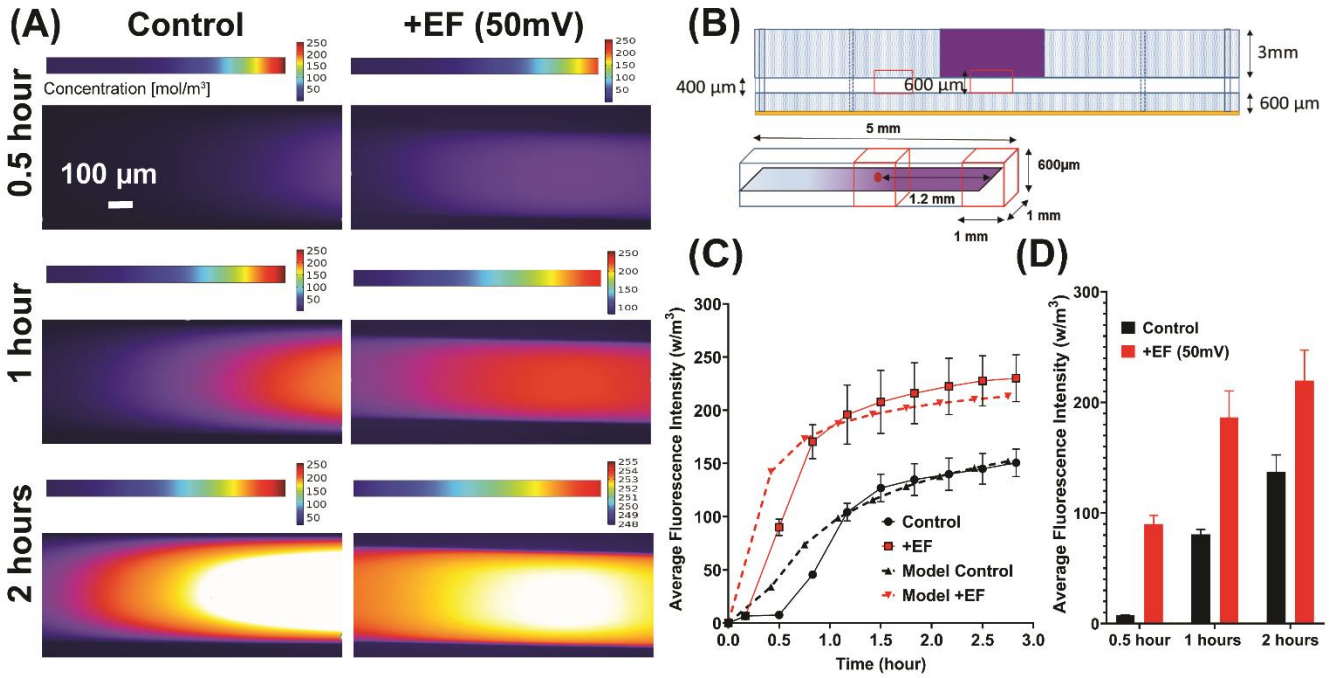

Figure 2.4. 2. Low-intensity electric fields increase cationic macromolecule transport into the hydrogel. (A) Snapshots comparing the transient concentration of the Alexa fluor 594® dye in the hydrogel channel at 0.5, 1 and 2-hour time points under the following conditions: **Left:** Diffusion only (Top: finite element model result, Bottom: experimental result); **Right:** Diffusion and electrophoresis at 50mV electric fields (Top: finite element model result, Bottom: experimental result). (**B)** The representative of the regions in the cell culture chamber and hydrogel channel of the device, for the measurement of dye transient concentration (Top: experimental regions, Bottom: computational domain). (**C)** The graph shows the validation of finite element model results for the dye transient concentration obtained experimentally by measuring average fluorescence intensity in the hydrogel channel under the following conditions: (i) Control (diffusion only), (ii) Diffusion and electrophoresis at 50mV electric fields. (**D)** Summary of the average fluorescence intensity of Alexa fluor 594® dye at 0.5 hours, 1 hour and 2-hour time points under the same conditions as C. Graph show an increase (48.12%, n=46, p-value<0.0001) in the average fluorescence intensity of the dye by applying 50mV electric potential gradient in the hydrogel microchannel after 2 hours.

2.4.3. Low-intensity electric field increases Carboplatin cytotoxicity in breast cancer single cells

Drug concentration optimization showed that 1.5nM-3.2nM paclitaxel and carboplatin have around 59% and 71% percent dead, respectively (**Figure 2.3.2 A**). We specified the low-intensity electric field to be 50mV based on model sensitivity analysis and drug concentration less than EC90 (2 nM) based on dose-response curves. A significant difference was observed in percent of dead cells by applying a 50mV electric field and 3mA electric current for 3 hours (**Figure 2.4.3 A&C**). The percent dead cells increase is 22% (p-value<0.05) in cell culture chamber (**Figure 2.4.3 B**) and 39.13% (p-value<0.05) in electrophoresis microchannel (**Figure 2.4.3 D**).

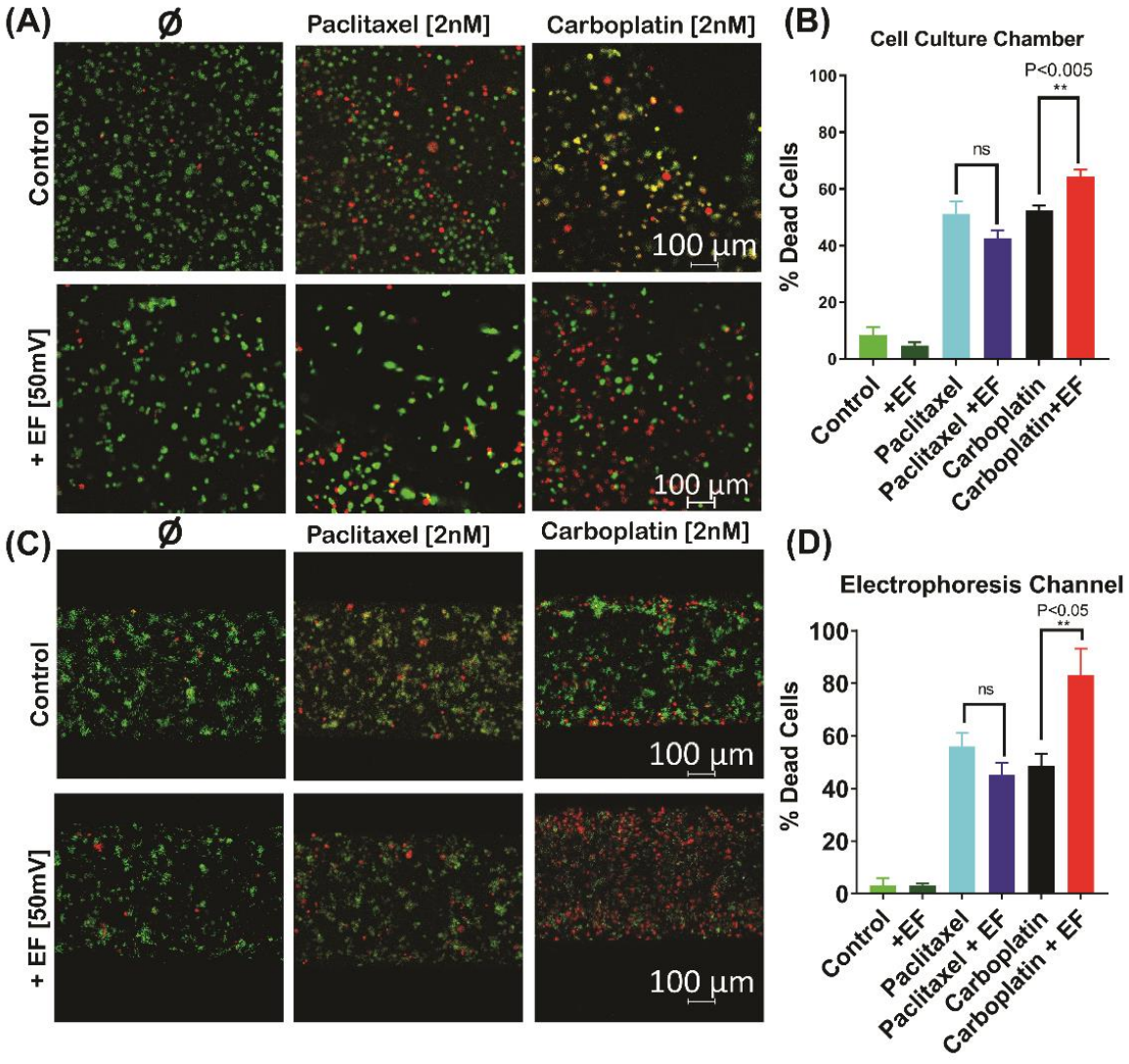

Figure 2.4. 3. Low-intensity electric field increases the delivery of carboplatin to single tumor cells. Confocal microscope images showing the live-dead cell staining of single tumor cells when exposed to the following treatments: cell culture medium, DMEM/F-12 (no drug); paclitaxel [2 nM] (non-ionized drug); and carboplatin [2nM] (anionic drug), with and without electric field (50 mV) in the device's **(A)** cell culture chamber and **(C)** hydrogel channel. Graph shows the percent dead tumor cells when exposed to the following treatments: (i) control (cell culture medium, DMEM/F-12 (*no drug, no electric field*), (ii) cell culture medium, DMEM/F-12 (*no drug, with electric field (50mV)*),(iii) paclitaxel [2 nM] (*non-ionized drug, no electric field*), (iv) paclitaxel [2 nM] (*non-ionized drug, with electric field (50mV)*), (v) carboplatin [2nM] (*anionic drug, no electric field*), and (vi) carboplatin [2nM] (*anionic drug, with electric field (50mV)*), in the device's **(B)** cell culture chamber and **(D)** hydrogel channel, respectively. Tumor cells that are treated with [2 nM] carboplatin in the presence of 50 mV electric field showed the least viability of all the treatments, with dead cell percent about 64% (n=3, $p<0.05$) in cell culture chamber and 83% (n=3, $p<0.05$) in hydrogel channel.

2.4.5. The fraction of cells killed model validation with the *in vitro* experiment

The fraction of cells killed model was developed to facilitate the prediction of iontophoresis outcome. The *in vitro* results of percent dead cells versus hydrogel depth were used for model validation (**Figure 2.4.4 A**). Summary of results in percent of dead cells at a different distance from the bottom of the chamber showed an increase in percent dead cells by administering electrophoresis carboplatin delivery (**Figure 2.4.4 B)**. The validated fraction of cells killed model showed an increase in percent dead cells by applying 50 mV electric field and 3mA electric current for 3hr experimentally and mathematically **(Figure 2.4.4 C)**.

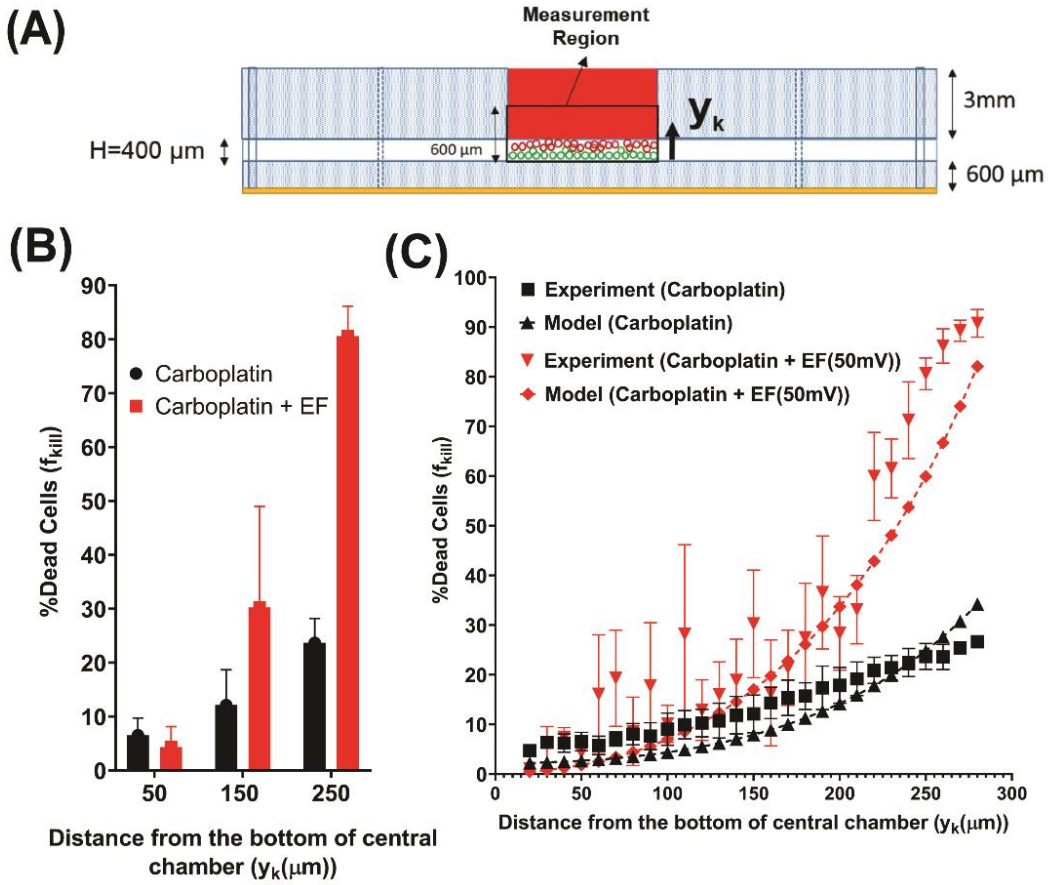

Figure 2.4. 4. The percent dead tumor cells model validation shows that low-intensity electric field promotes iontophoretic delivery of carboplatin into breast cancer cells. (A) The representative of the experimental measurement region in the cell culture chamber of the device, for calculating the percent dead tumor cells when treated with [2 nM] carboplatin with and without electric field (50 mV). (**B)** The graph shows an increase in percent dead tumor cells that are seeded at 50 µm,150 µm, and 250 µm distance from the bottom of the cell culture chamber and treated with [2 nM] carboplatin with and without electric field (50 mV); the difference in the percent dead cells when treated with [2 nM] carboplatin with electric field is significantly higher at 250 µm (closest to drug source) compared to other distances. **(C)** Percent of dead tumor cells model validation with the *in vitro* experiment shows an accurate correlation between model and experiment (**Table 2.4.1**).

The correlation between the fraction of cells killed model and *in vitro* experiment was measured using five different methods [314] (**Table 2.4.1**). The correlation between predicted and observed cationic dye concentration in the hydrogel was calculated using the same statistical methodologies.

Table 2.4. 1. Drug delivery models and *in vitro* experiment correlation

	FAC2 Factor of two	**FB** Fraction of bias	**RNMSE** Root normalized mean square error	**GM** Geometric mean bias	**GV** Geometric mean bias-variance
	$0.5 < \frac{C_{model}}{C_{exp}} < 2$	$\frac{2(\overline{C_{exp}} - \overline{C_{model}})}{\overline{C_{exp}} + \overline{C_{model}}}$	$\sqrt{\frac{\overline{(C_{exp} - C_{model})^2}}{\overline{C_{exp}}\,\overline{C_{model}}}}$	$\exp\left(\overline{\ln\left(\frac{C_{exp}}{C_{model}}\right)}\right)$	$\exp\left(\overline{\left(\ln\left(\frac{C_{exp}}{C_{model}}\right)\right)^2}\right)$
Ideal Value	1	0	0	1	1
Concentration +EF	1.398	-0.006	0.004	1.113	1.107
Concentration Control	1.351	-0.053	0.054	0.872	1.088
%Cells dead +EF	0.7	0.2	0.3	1.6	1.9
%Cells dead control	0.7	0.02	0.3	2.1	1.4

Our results demonstrate that a 50mV DC electric field and 3mA electric current increases drug delivery by 48.12% and increases cell death by 39.13%. Our obtained experimental results validated our recent drug transport model [29]. We see FB (fractional bias) equal to 0.02 in which positive FB indicates under prediction, RNMSE (root normalized mean square error) [315] equal to 0.3 indicates low scattering from mean. Overall, the statistical analysis indicates a strong correlation between model and microfluidic experiments.

2.5. Author Contributions

MM, and CNJ designed the experiments and device, edited the manuscript, and the work was done under CNJ supervision. MM, and CNJ conceived the experiment(s). MM designed iontophoresis-on-chip, conducted the experiments, developed the electrokinetics models, and analyzed the data. DKT, RVD, and LEA contributed to microfluidic device design and computational model. All authors have read and approved the article.

2.6. Funding

Research materials and equipment for this study were funded by CNJ startup funds from the Department of Biological Sciences at Virginia Tech. MM was supported by the VT-Initiative for Maximizing Student Development (IMSD) (NIGMS 2R25GM072767-05A1) and the Department of Mechanical Engineering at Virginia Tech. This publication was supported in part by the Open Access Subvention Fund (OASF) at Virginia Tech.

2.7. Acknowledgments

The authors would like to thank Dr. Jiangtao Cheng for kindly providing us the electrical instruments required for the experimental work. We also acknowledge support from the Fralin Life Sciences Institute of Virginia Tech for facilitating confocal imaging and Micro & Nano Fabrication Laboratory at Virginia Tech's Bradley Department of Electrical and Computer Engineering for master molds fabrication.

2.8. Conflicts of interest

There are no conflicts to declare.

CHAPTER 3

Electrotaxis-on-chip to quantify neutrophil migration towards electrochemical gradients

3.1. Abstract

Cell migration is an essential phenomenon in most physiological processes, such as immune responses to infection and wound healing. Immune cells are known to migrate towards both chemical (chemotaxis) and physical stimuli. Electrotaxis, a physical stimulus, is the electric field gradient inducing directional cell migration in the cellular microenvironment. The magnitude and direction of the electric field can be more precisely and quickly changed than most other guidance cues such as chemical cues in clinical investigation. Recent *in vivo* and *in vitro* studies show an intense migration of T-cells toward the cathode of a DC electric fields in the presence of a competing chemoattractant gradient. The migration of T-cells toward the cathode implies that electrotactic attraction is dominant over chemotactic cues in lymphocytes migration. Here, for the first time, we show that this concept also applies to neutrophils, the most abundant innate immune cell. Also, chemokines such as LTB_4 increase the chemotactic activity of neutrophils toward the inflamed site (e.g., lungs in respiratory diseases), and fMLP is a highly potent neutrophil chemoattractant toward the cite of infection. In this study, we investigate three scenarios 1) Neutrophil migration toward the cathode of a DC electric field. 2) Reducing neutrophil migration towards an inflammatory chemoattractant (LTB_4) and perpendicular electric field gradient. 3) Increasing neutrophil migration towards an infection with parallel pro-resolution chemoattractant (fMLP) and electric field gradient. The electric field values were chosen based on reported endogenous electric field gradient in injury (<100 mV or 0.66 V/cm), and external applied electric fields (<600mV or 4 V/cm) in the leucocytes electromigration *in vitro* experiment settings. Results indicates a significant electromigration (n=4, p-value<0.005) of dHL60s toward cathode without chemotaxis and a significant decrease in the migration of dHL60s toward LTB_4 by applying 400mV (n=4, p-value<0.05) and 600mV (n=4, p-value<0.05) DC electric fields gradient. Also, electromigration of dHL60s toward pro-resolution chemoattractant (fMLP) and cathode demonstrate a significant increase in dHL60 migration toward fMLP and cathode of DC electric field by applying strength of 40 mV (n=4, p-value<0.005), 80 mV (n=4, p-value<0.001), 200 mV (n=4, p-value<0.005), 400 mV (n=4, p-value<0.005), and 600mV (n=4, p-value<0.001) .

3.2. Introduction

Directional cell movements toward attractive and away from repulsive signals are notably critical in almost all physiological processes. Physiological and externally applied electric fields [8, 110, 161-203] (electrotaxis/galvanotaxis) are essential factors for inducing cell migration in the tissue microenvironment. Signaling pathways involved in the electrotaxis phenomenon are still not fully understood. However, recent studies demonstrate electro-migration (electrophoretic and electroosmotic) of cell surface receptors, voltage-gated ion channels in cells for calcium signaling [316], and asymmetric ion distribution and electromigration of ions inside the cell are some cellular mechanism of sensing and responding to cellular electric field gradient [317].

Neutrophils are the immune system's first responders against pathogenic infection after chronic wounds and injuries and linking innate and adaptive immunity in inflammatory immune responses. Endogenous DC electric field (dcEF) plays an important role in wound healing [110, 198, 201], tissue regeneration [11, 318, 319], and embryogenesis [320]. In addition to chemical stimuli (neutrophil chemoattractant), the endogenous DC electric field may influence neutrophil migration to the infectious (**Figure 3.2.1A**), there were no previous studies on the migration of neutrophils toward the cathode of an electric field. The migration of T-cells toward the cathode implies the investigation of the same concept in neutrophils. In the current investigation, we quantified the significance of neutrophil migration toward the cathode. We were able to increase neutrophil migrating towards pro-resolution signals (fMLP) (parallel field) as well as direct neutrophils away from pro-inflammatory signals (LTB_4) (perpendicular field).

LTB_4 and fMLP induce a respiratory burst in human neutrophils [321]. N-Formyl-Met-Leu-Phe (fMLP), a mimic of N-formyl oligopeptides that are released from bacteria, is a potent neutrophil chemoattractant at the site of infection. Also, fMLP induces cytokines (e.g., TNFα) release by macrophages in microbial infection, which is the cause of self-limited tissue barrier against the inflammatory response of neutrophils [322, 323] (**Figure 3.2.1**). We hypothesize the effect of exogenous and endogenous electric field gradient for enhancing the pro-resolution chemotaxis effect of fMLP and facilitating the pro-resolution migratory pathway for neutrophils (**Figure 3.2.1C**). On the other hand, LTB_4 is the lipid leukotriene B_4 and the pro-inflammatory pathway for neutrophils, which cause the neutrophil inflammation in healthy tissue such as skin and lungs. Neutrophil accumulation in the lungs causes damage to healthy endothelial and epithelial cells. It would be beneficial to redirect neutrophil to electro taxis signals, and the neutrophil migration induced by the externally applied electric field may be an alternate migratory pathway for neutrophils to reduce neutrophil migration towards an inflammatory chemoattractant (LTB_4) (**Figure 3.2.1B**).

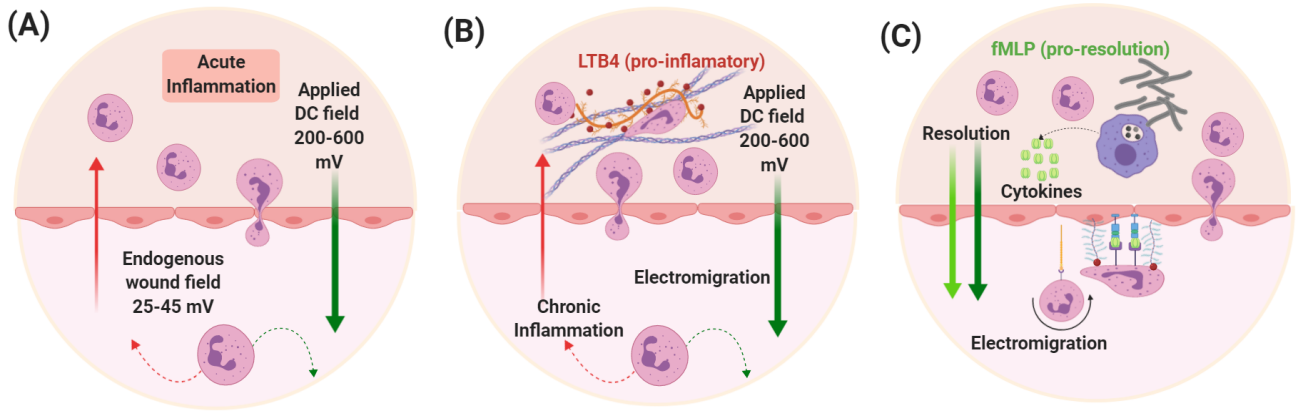

Figure 3.2.1. Chemotaxis and electro-taxis in sepsis. (A) Electromigration of neutrophils toward wounds' endogenous electric fields and externally applied electric fields. **(B)** Decision making of neutrophils towards an inflammatory chemoattractant (LTB_4) and perpendicular electric field gradient. **(C)** Decision making of neutrophil towards an infection with parallel pro-resolution chemoattractant (fMLP) and electric field gradient.

To recognize *in vivo* complexity of neutrophil migratory pattern and decision-making is essential to recapitulate chemoattractant and electric field gradients more accurately *in vitro* experimental model. Measuring individual cell velocity and directionality *in vivo* requires precise control of tissue spatiotemporal microenvironment. Microfluidic chemotaxis assay assists researchers to address neutrophil migration in spatiotemporally controlled chemo gradients [239-242]. Also, microfluidics electrotaxis assay has various advantages such as reduction of joule heating, facilitation of high through-put investigation, and precise control of electric fields, cells, and reagents [191]. Dual gradient microfluidic platform has been used to study neutrophil chemotaxis with coexisting pro-inflammatory and pro-resolution signals by previous researchers [251-253]. Researchers are interested in investigating the effect of co-existing chemotaxis and electrotaxis on cell migration [174]. Lymphocyte chemotaxis [249], electrotaxis [175, 181], and co-existing chemotaxis and electrotaxis [176] show the migration of T-cells toward the cathode. The study of T-cells migration suggested higher electrotactic

attraction of T-cells toward cathode of DC electric fields in the presence of a competing CCL19 chemoattractant gradient. However, a microfluidic device for quantifying neutrophil time-dependent migration pattern and decision making with co-existing electrotaxis and chemoattractants (pro-inflammatory (LTB_4) and pro-resolution (fMLP)) has not been studied yet. In this study, we designed a novel four-sided microfluidic platform for studying neutrophils' migration decision making toward fMLP or LTB_4 in the presence of an electric field gradient. Recent microfluidics electrotaxis assays [167, 174-176, 178, 180, 181, 191, 192, 213, 250] used electric field intensity between (4V-20V) to reach the target of 0.4V/cm-4V/cm electric potential gradient for inducing cell electromigration in microchannels. The endogenous electric field experimentally measured in wound healing was 0.4V/cm-2V/cm, and many clinical trials reported a significant increase in the rate of wound healing from 13% to 50% [254]. On the other hand, exogenous electric fields of higher intensities used for transdermal drug delivery [255], increase the permeability of cell membrane [256], and a therapeutic tool for restoring tissue integrity in severe injuries with the exogenous electric field of less than 4 V/cm.

3.3. Materials and Methods

3.3.1. Device Design and Fabrication

A novel microfluidic competitive chemotaxis chip (μC3) previously reported in our study [13] is designed with two chemoattractant reservoirs that enable the formation of a chemoattractant gradient. The adopted design (Electro-Chemotaxis-On-Chip (ECOC)) includes highlight that you added an electric field to this design. ECOC device consists of four parts: (i) Control reservoir (blue) contains the complete cell medium (**Figure 3.2.2**

Ai). (ii) fMLP chemoattractant reservoir (green) (**Figure 3.2.2 Aii**). (iii) LTB_4 chemoattractant reservoir (red) (**Figure 3.2.2 Aiii**). (iv) Anode reservoir (black) contains the complete cell medium (**Figure 3.2.2 Aiv**). (v) Central cell-loading chamber for loading neutrophil (**Figure 3.2.2 Av**). (vi) Four linear migration channels connecting the central cell-loading to reservoirs for quantifying neutrophil electromigration (**Figure 3.2.2 Avi**). **Figure 3.2.2 B** demonstrates the device and experimental design. The TRANS and DAPI images of the microfluidic device were taken by Nikon TiE microscope with 20X objective, and stained dHL60 by Hochstein (DAPI fluorescent DNA stains) were loaded inside the device (**Figure 3.2.2 C**). The COMSOL simulations showed electric potential (**Figure 3.2.2 Di & Dii**) in the migration channels.

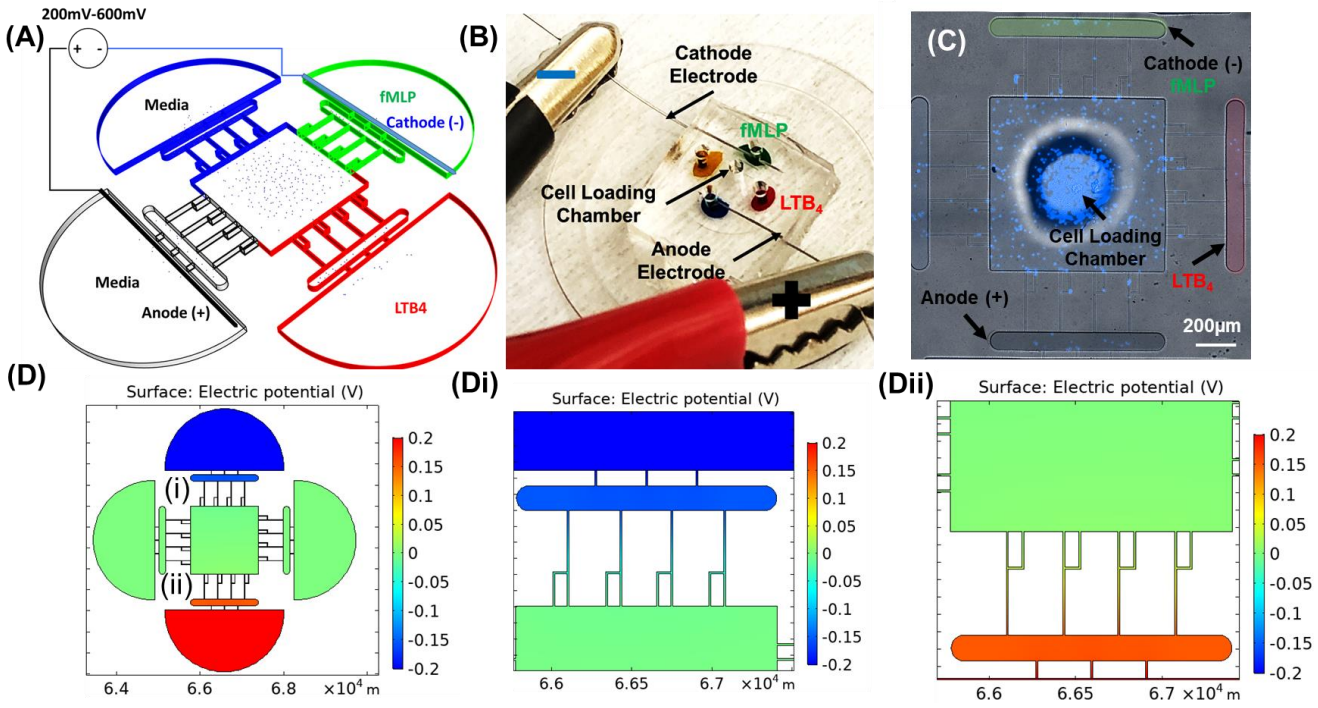

Figure 3.2.2. Electro-Chemotaxis-On-Chip (ECOC) microfluidic platform A. Microfluidic device design (i) Control reservoir (blue) contains a complete cell medium. (ii) fMLP chemoattractant reservoir (green). (iii) LTB_4 chemoattractant reservoir (red). (iv) Anode reservoir (black) contains a complete cell medium. (v) Central cell-loading chamber for loading neutrophil. (vi) Four linear migration channels connecting the central cell-loading to reservoirs for quantifying neutrophil electromigration. **B**. PDMS based microfluidic device, LTB_4 chamber color-coded with a red food dye and fMLP chamber color-coded with a green food dye. The anode chamber is black, and the media chamber is brown color-coded. Stainless still electrodes were inserted in the cathode and the anode chamber. The cell loading chamber is at the center of the device. **C.** Nikon TiE microscope 20X image of the microfluidic device and stained dHL60 by Hochstein (DAPI fluorescent DNA stains) **D.** The electric potential gradient in the migration channels. (i) Cathodic channels. (ii) Anodic channels.

A microfluidic device for quantifying neutrophil migration pattern was designed and fabricated using standard photolithography techniques [304]. Two standard photolithography techniques were used to create a silicon mold from two separate masks, chemoattractant wells, and migration channels. Mask aligner (Karl Suss MA-6 Mask Aligner) was used to align two separate masks. Replication molding techniques facilitate the fabrication of PDMS (polydimethylsiloxane) microfluidic device [305]. Mixing the

PDMS and curing agent with a 10:1 weight ratio prepared PDMS pre-polymer (Sylgard 184; Dow Corning, Waltham, MA). The PDMS prepolymer was then degassed in the desiccator and poured onto prepared silicon mold. The PDMS was cured at 65°C for 8hr. After curing, the inlets and outlets were punched using a 0.75 mm biopsy puncher. Finally, PDMS device was bonded to a glass slide using nitrogen plasma bonding (Nordson MARCH (AP-300)) for mechanical stability and place on an 80°C hot plate for 45 min.

3.3.2. Cell preparation and loading

Human promyelocytic leukemia cells (HL60 CCL-240, American Type Culture Collection ATCC, Manassas, VA) were used in this study. Iscove's Modified Dulbecco's Medium (IMDM, ATCC, Manassas, VA) supplemented with 10% fetal bovine serum (FBS, ATCC, Manassas, VA) were used as a complete media for HL60 cells. Cells were cultured (90% confluent) in complete media and incubated at 37°C in 5% CO_2. 1.5% Dimethyl sulfoxide (DMSO, Sigma-Aldrich, St. Louis, MO) was added to $1.5X10^6$ cells. mL^{-1} of HL60s and incubate for 4-5 days to differentiate cells to a neutrophil-like state (denoted as dHL60 cells). dHL60s were spun down (130G) at RT for 7 min before the experiment and resuspended in fresh media. Then, the central cell-loading chamber for loading neutrophil (**Figure 3.2.2 Av**) was filled by dHL60 cells (4000K cell/40 µL) using a gel loading pipette tip. Devices were washed with 1X PBS (Thermo Fisher Inc.) twice; then, plates were filled with complete media before the experiment. Complete media were changed before time-lapse imaging. Viability of dHL60 cells loaded into the microfluidic platform was>90% viable, as confirmed by live and dead cell staining assay after 8 hours of time-lapse imaging with 600 mV and without chemotaxis assay (**Figure 3.2.3**).

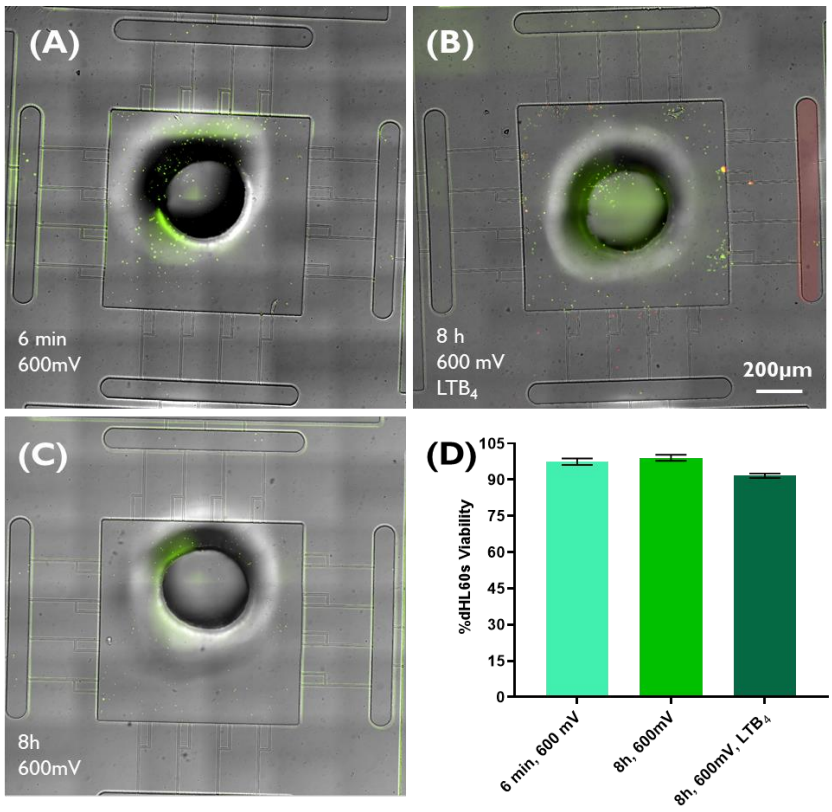

Figure 3.2.3. Viability of dHL60s by applying 600 mV electric field for 8h. **(A)** Live/dead image at t= 6 min. Stained dHL60s by live and dead cells fluorescent assay (Abcam, Cambridge, MA) illustrated high percent viability at the beginning of the experiment (t= 6 min). **(B)** Live/dead image at t= 8h under the effect of an electrochemical gradient. Stained dHL60s under the effect of two conditions: 100µm of LTB_4 chemoattractant and the 600-mV electric field gradient demonstrated the high percentage of viability. **(C)** Live/dead image at t= 8h under the effect of the electric field gradient. Stained dHL60s under the effect 600-mV electric field gradient indicated the high percentage of viability. **(D)** The quantification of percent viability of dHL60s under three different conditions. dHL60 viability in the microfluidic device (n = 2) proved after 8 hours of migration experiment, dHL60 cells loaded into the microfluidic platform were >90% viable.

3.3.3. Electrotaxis assay and experiment setup

Complete media (IMDM+10% FBS) salt bridge was used to connect electrotaxis wells in the microfluidic device. Sterile stainless-steel acupuncture needles (Kingi, China) with a diameter of 0.12 mm were placed at the inlet and outlet of the electrotaxis wells to deliver DC electric field, and stainless-steel wires (Zoro, Inc.) were used to construct electric field circuit. Electrodes were fixed using Epoxy glue (Devcon Inc.), and devices were washed stay in 1X PBS (Thermo Fisher Inc.) for 30 min twice and washed

twice for removing any toxicity from Epoxy glue. Optimal electric field intensities were chosen to induce maximal dHL60 cell migration for both endogenous DC field and applied DC field. The characteristic length of the current microfluidic device is 5 cm. Therefore, we chose the range of electric field from 0 mV to 600 mV electric field intensity to address reported intensities in clinical and in vivo investigations (0.4 V/cm-4 V/cm). The electro taxis conditions include 1. An endogenous electric field gradient in injury (<100 mV). 2. External applied electric fields (<600mV).

3.3.4. Chemotaxis Assay

Fibronectin is a large and the most abundant glycoprotein in the extracellular matrix [13]. In has been used in previous microfluidic-based studies for increasing cell adhesion [6]. Microfluidic channels were coated using 50 µL fibronectin (Sigma-Aldrich, St. Louis, MO) [10 µg/mL] to mimic the extracellular matrix (ECM) neutrophil adhesion promotion. After adding fibronectin on top of the device, the device was then placed in a vacuum desiccator for 10 min and an additional 45 min to 1 hour at the room temperature for fibronectin adsorption to the glass and PDMS channel surfaces. The drop of fibronectin should cover all punches to let the air displaced by fibronectin solution in PDMS channels. The 6-well plates were filled with 4.5 ml of 1X PBS. Chemoattractants Leukotriene B4 (LTB_4, Cayman Chemical, Ann Arbor, MI) and (N-Formylmethionine-leucyl-phenylalanine (fMLP, Sigma-Aldrich, St. Louis, MO) were diluted using complete media (IMDM+10%FBS). Ten microliters of each chemoattractant solution (fMLP, [10 µM] and LTB_4, [100 µM]) were then loaded into the chemoattractant reservoirs. The first set of experiments are without chemoattractant. In the second set, LTB_4 chemoattractant was loaded using gel loading pipettes. The third

set of experiments was with fMLP chemoattractant. Clinically relevant optimal chemoattractant concentrations previously reported [6] for inducing maximal dHL60s migration.

3.3.5. Live microscopy and image processing

Nikon TiE fully-automated microscope equipped with a Plan Fluor 10x Ph1 DLL (NA = 0.3) lens and 37°C with 5% carbon dioxide incubator was used for time-lapse imaging experiments. NIS-elements (Nikon Inc., Melville, NY) software facilitates image capturing and analysis conducted by using ImageJ. Images were recorded using a bright-field channel at six-minute intervals for 8 hr. Live/dead images were captured using FITC (green) and TRITC (red) fluorescent channels. The number of cells per channel migrating toward chemoattractant, cathode, and anode reservoirs, was quantified as followed: (1) Control (no gradient) (2) Electrotaxis (3) Co-existing chemotaxis and electrotaxis. We used dHL60s cell type as neutrophils. DC electric field variations are: 0 mV, 40 mV, 80mV, 200 mV, 400 mV, and 600 mV. Low-intensity DC fields (0 mV, 40 mV, and 80mV) mimic endogenous DC fields, and high-intensity (200 mV, 400 mV, and 600 mV) mimics applied DC fields. We used two chemoattractant: (1) LTB_4 (pro-inflammatory): [100 µM]. (2) fMLP (pro-resolution): [10 µM].

3.3.6. Statistical analysis

Prism version 8.1.2 (332) software (GraphPad Software, La Jolla, CA) with a confidence level of $\alpha = 0.05$ was used for statistical analyses. Pair t-test comparison was used for comparing a control condition to electric field gradient conditions (n= 4) as well as dHL60 viability in the microfluidic device after 8 hours of migration experiment (n = 2). Data are presented as arithmetic mean ± SD.

3.4. Results and Discussion

3.4.1. Effect of DC electric fields gradients on dHL60s electromigration

First, we inspected the effect of electric field gradients on the dHL60s (denoted as neutrophil) loaded in the central chamber of the device. Five different electric field intensities were investigated in this section to simulate endogenously (<100 mV) and externally applied electric fields (<600mV). In the absence of an electric field (denoted as EF), control condition, neutrophils had a significantly low migration, less than ~5 cells per channel, into the four side-chambers. After electric field gradient stimulation, neutrophils migrated toward the cathode more strongly. Examining the effect of externally endogenous EF (<100mV) intensities showed a significant migration of neutrophils toward cathode at 40mV (n=4, p-value=0.0006) and 80mV (n=4, p-value=0.0026) electric field gradients. Also, 40mV electric field gradient indicated more significant migration than 80mV. On the other hand, 600mV (n=4, p-value=0.0003) indicated the most significant migration toward the cathode in the range of externally applied electric fields (**Figure 3.4.1 C**). Migration toward media was significantly low, less than ~5 neutrophils per channel, which is expected due to the elimination of electrical signal and chemical stimuli (**Figure 3.4.1 D**). The most critical finding of neutrophil directional movement during electrotaxis is the low migration of neutrophils toward the anode, less than ~5 neutrophils per channel, and significant migration toward the cathode, more than ~20 cells per channel (n=4, p-value<0.005), which indicated the neutrophils' positive polarity. However, the neutrophil induced polarity by applied electric fields needs a single-cell analysis and molecular investigation.

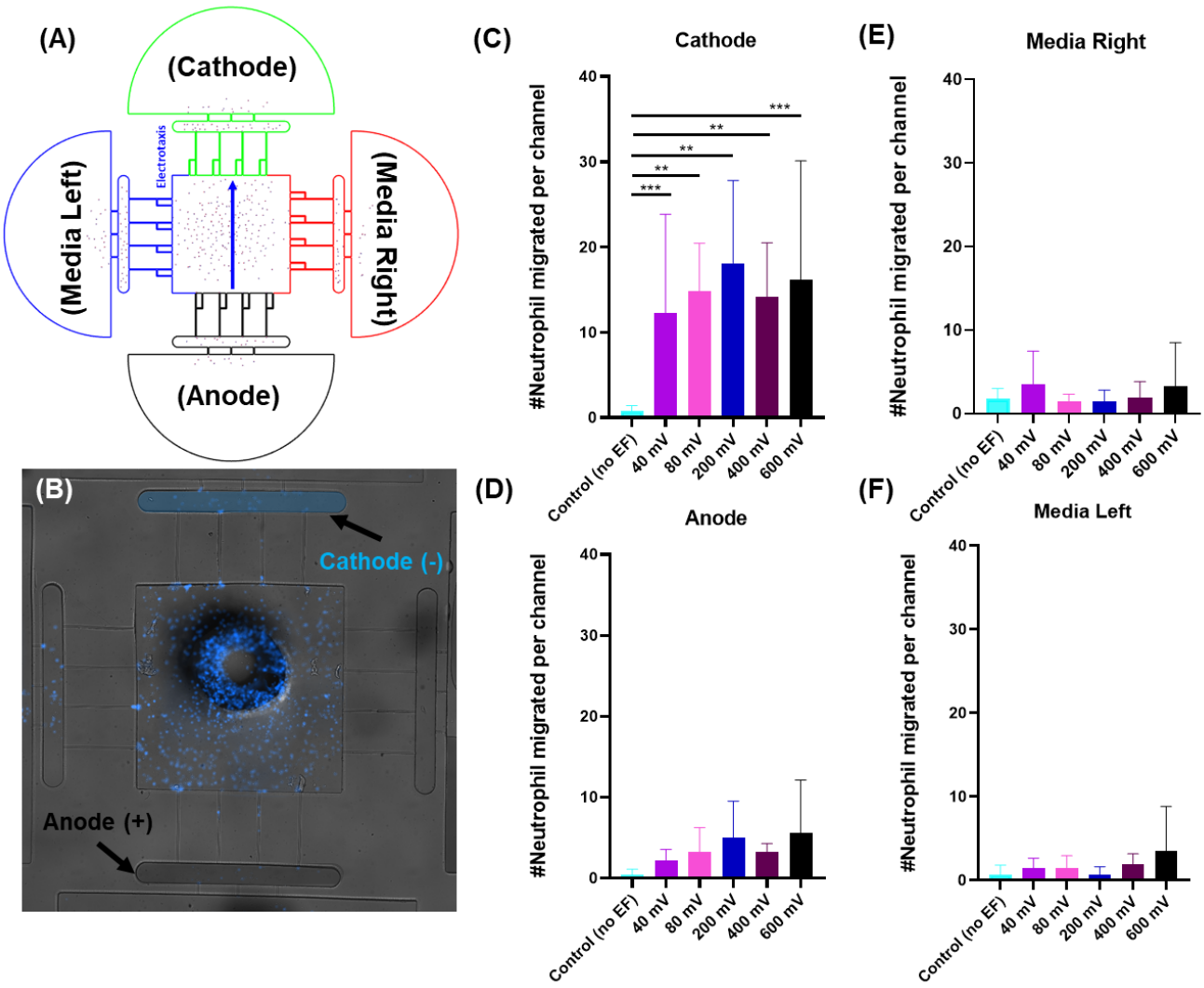

Figure 3.4.1. Neutrophil electromigration under the effect of the DC electric field gradient. **A.** The schematic of the microfluidic experiment design for investigating the effect of electro taxis signal on neutrophil migration without any chemoattractant. **B.** Nikon TiE microscope 20X image of the microfluidic device and stained dHL60 by Hochstein (DAPI fluorescent DNA stains). **C.** Quantification of the number of neutrophils migrated per channel toward the cathode. The result shows a significant increase (65%-80%) in migration by applying different DC electric fields strength (n=4, p-value<0.005). **D.** Quantification of the number of neutrophils migrated per channel toward the anode. The result indicates a significantly low, less than ~5 cells per channel, directional movement of neutrophils toward the anode. **E&F**. Quantification of the number of neutrophils migrated per channel toward the complete media. The result shows approximately no neutrophil migration toward the complete media due to no electrical or chemical signals.

3.4.2. Effect of DC electric fields gradient co-exist with LTB_4 chemoattractant on dHL60 migration

Second, we examined the effect of co-existing pro-inflammatory chemotaxis (LTB_4 gradient) and electrotaxis. LTB_4 [100μM] was added to one side of the device for generating a perpendicular pro-inflammatory chemoattractant gradient to DC electric field gradients to test the neutrophil decision making. The switching direction of neutrophils to LTB_4 chemoattractants was observed in the second set of the experiment. The perpendicular chemoattractant gradient attenuated neutrophils migration toward the cathode. However, the migration of neutrophils toward the cathode significantly increased by applying electric fields. Neutrophil migration toward the cathode showed that 40mV (n=4, p-value=0.0008), 80mV (n=4, p-value<0.0001), 200mV (n=4, p-value=0.0001), 400mV (n=4, p-value<0.0001), and 600mV (n=4, p-value=0.0026) induced a significant migration toward the cathode in the presence of pro-inflammatory chemoattractant gradients in the perpendicular direction (**Figure 3.4.2 C**). The migration of neutrophils toward LTB_4 significantly decreased (60%-70%, n=4, p-value<0.005) by applying 400 mV (n=4, p-value=0.0233) and 600 mV (n=4, p-value=0.0325) electric fields. However, low strength electric field gradient (<400 mV) did not attenuate neutrophil migration toward the cathode (p-value=0.7-0.9) (**Figure 3.4.2 E**). A similar result to the first set experiment was obtained in neutrophil migration toward media due to no electrical or chemical cure in the media chamber(**Figure 3.4.2 D**). Migration toward the anode showed a trend of increased migration by increasing

applied fields. However, neutrophils' movement toward the anode, less than ~15 cells per channel, is not significant.

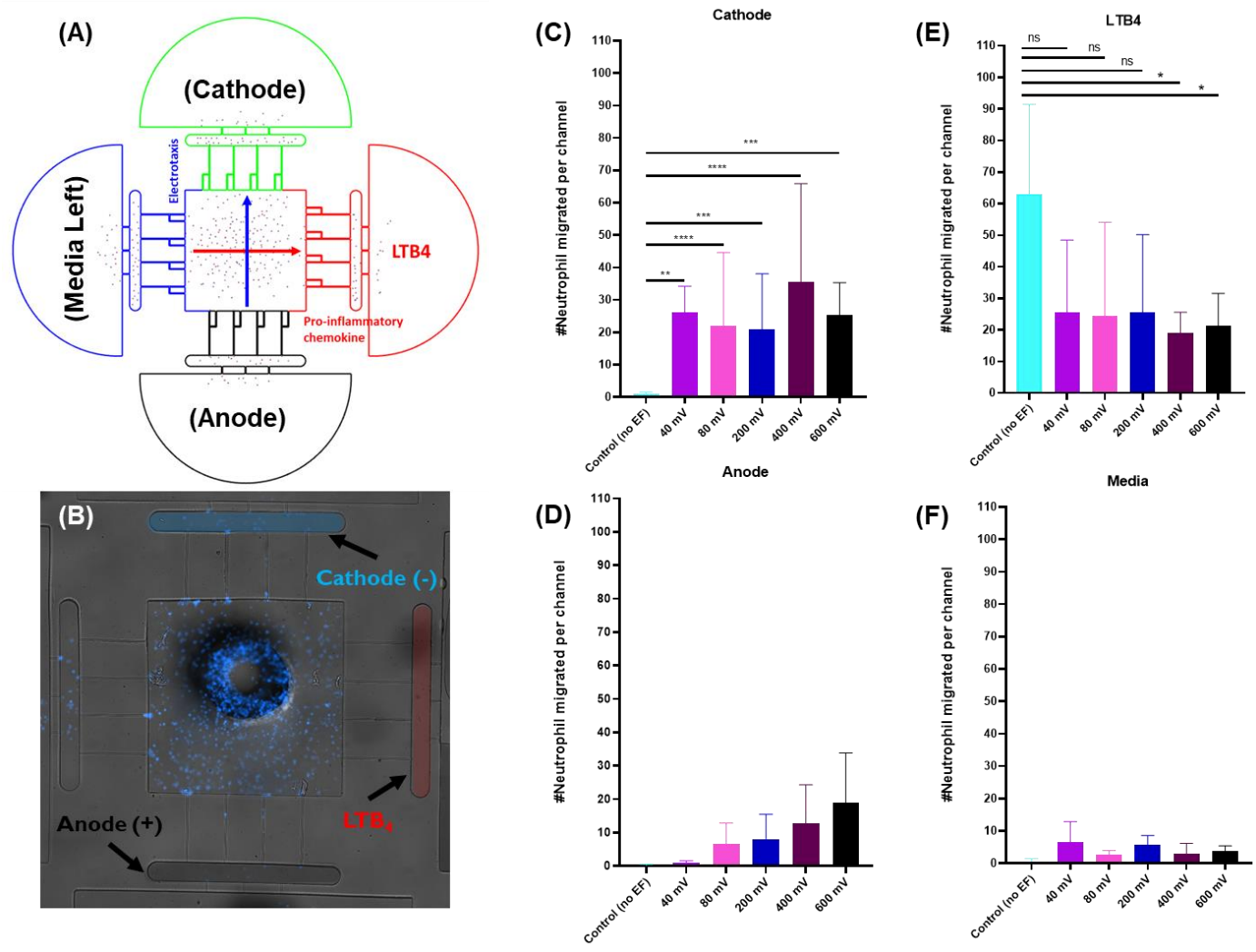

Figure 3.4.2. Neutrophils electromigration under the effect of pro-inflammatory chemoattractant and DC electric field gradient. A. The schematic of the microfluidic experiment design for investigating the effect of pro-inflammatory electro taxis and chemotaxis signals on neutrophil migration. **B.** Nikon TiE microscope 20X image of the microfluidic device and stained dHL60 by Hochstein (DAPI fluorescent DNA stains). **C.** Quantification of the number of neutrophils migrated per channel toward the cathode. The result shows a significant increase (80%-90%) in migration by applying different DC electric fields strength (n=4, p-value<0.005). **D.** Quantification of the number of neutrophils migrated per channel toward the anode. The result indicates a significantly low, less than ~5 cells per channel, directional movement of neutrophils toward the anode. Neutrophil migration toward the anode is around 50% more than neutrophil migration toward a complete media. **E**. Quantification of the number of neutrophils migrated per channel toward the pro-inflammatory chemoattractant gradient (LTB_4). Results show a significant decrease (60%-70%) in neutrophil migration toward LTB_4 by applying external electric fields (400mV (n=4, p-value=0.0233) and 600 mV (n=4, p-value=0.0325)). **F**. Quantification of the number of neutrophils migrated per channel toward the complete media. Results show approximately no neutrophil migration toward the complete media due to no electrical or chemical signals.

3.4.3. Effect of DC electric fields gradient co-exist with fMLP chemoattractant on dHL60 migration

The third scenario was using the usage of neutrophil-like dHL60s' electromigration for increasing neutrophils' directional movement to the cite of infection. 10 µM of fMLP was added to the cathode side of the device, side A, for generating a parallel pro-resolution chemoattractant gradient to the electric field gradient to test the third hypothesis. Applying the electric field enhanced the migration of neutrophils toward fMLP chemoattractant significantly. I some cases such as 80 mV ($n=4$, $p\text{-value}<0.001$) and 600mV ($n=4$, $p\text{-value}<0.001$) the effect of electric field gradient was more significant. In other cases, such as 40 mV ($n=4$, $p\text{-value}<0.005$), 200 mV ($n=4$, $p\text{-value}<0.005$), and 400 mV ($n=4$, $p\text{-value}<0.005$) the significant enhancement in migration was observed (**Figure 3.4.3 C**). As expected, according to the first two scenarios, the migration of neutrophils toward the anode is 86% (600mV), 62% (400 mV), 60% (200 mV), 90% (80 mV), and 42% (40 mV) less than the cathode (**Figure 3.4.3 D**). Sides of the device with the complete media demonstrated no significant migration due to the elimination of electrochemical gradients (**Figure 3.4.3 E&F**)

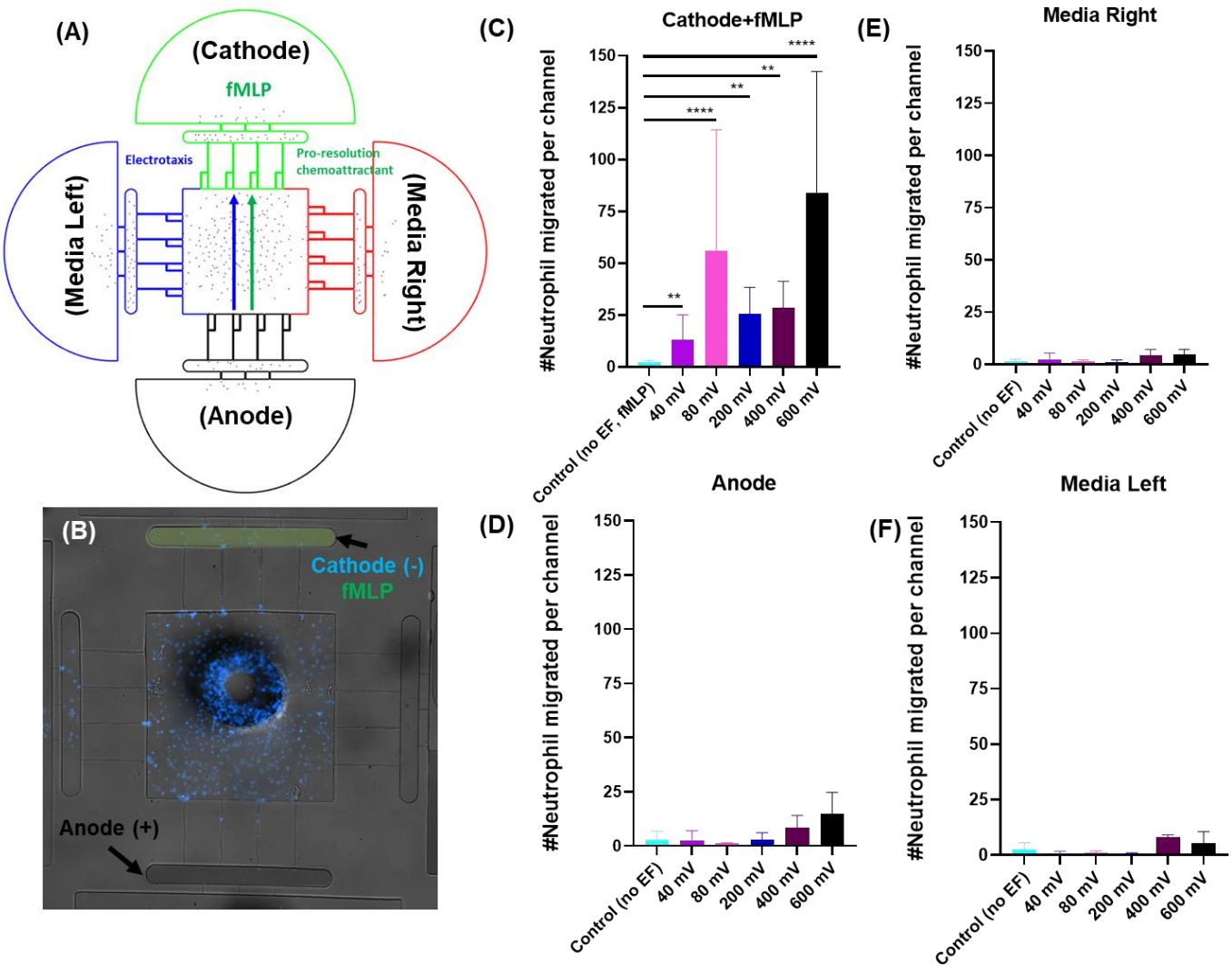

Figure 3.4.3. Neutrophils electromigration under the effect of pro-resolution chemoattractant and DC electric field gradient. A. The schematic of the microfluidic experiment design for investigating the effect of pro-resolution electro taxis and chemotaxis signals on neutrophil migration. **B.** Nikon TiE microscope 20X image of the microfluidic device and stained dHL60 by Hochstein (DAPI fluorescent DNA stains). **C.** Quantification of the number of neutrophils migrated per channel toward the cathode and pro-resolution fMLP chemoattractant. The result shows a significant increase (85%-95%) in migration by applying different DC electric fields strength of 80 mV and 600mV (n=4, p-value<0.001). **D.** Quantification of the number of neutrophils migrated per channel toward the anode. The result indicates a significantly low, less than ~5-10 cells per channel, directional movement of neutrophils toward the anode. **E&F**. Quantification of the number of neutrophils migrated per channel toward the complete media. Results show approximately no neutrophil migration toward the complete media due to no electrical or chemical signals.

Three main findings of the current microfluidics in vitro experiment are 1) Neutrophil migrated toward the cathode of a DC electric field ($n=4$, $p\text{-value}<0.005$). 2) Neutrophil migration towards an inflammatory chemoattractant (LTB_4) reduces significantly ($n=4$, $p\text{-value}<0.005$) by applying perpendicular electric field gradient. 3) Neutrophil migration towards an infection with pro-resolution chemoattractant (fMLP) increased significantly ($n=4$, $p\text{-value}<0.0001$) by applying the concurrent electric field gradient to chemotaxis.

CHAPTER 4

Conclusion and Future Work

4.1. Iontophoresis chemotherapy

Previously iontophoresis was used for delivering drugs into the eye or organs that drug injection is impossible. Current work demonstrates for the first-time an iontophoresis-on-chip platform to mimic the outcome of iontophoretic drug delivery for the treatment of breast cancer. Our device could potentially be used for high-throughput screening of charged drug candidates for the iontophoretic treatment of breast cancer. Our modeling and experimental results show that an applied electric field intensity of 50-70 mV DC electric fields and 3 mA electric current lead to the maximum percentage of dead cells (70%-90%). This low-intensity electric field has been reported to have a minimal side effect on healthy tissues and is reported to be significantly lower than that used for electroporation. The on-chip platform allows us to precisely control the physics of transport phenomena by adjusting the device geometries, boundary conditions, and initial values of drug dose and electric field intensity to match the mathematical model. The predictive models that we developed in this manuscript define the influence of DC electrical fields and electric current on iontophoretic drug delivery to tumors and may assist physicians in designing effective treatment regimens for breast cancer patients [278]. Our device also can vary flow, ECM porosity, electric field intensity, tumor size, and tumor type. This model is a first step towards generating a predictive model for *in vivo* applications. Further improvements to the model for transdermal iontophoretic drug delivery can be made and validated by adding additional components in the microfluidic device, mimicking the skin or human epidermis. Currently, iontophoresis is only used for

transdermal drug delivery to accessible tumors. In the future, endoscopic surgeries may enable the implantation of 3D printed hydrogels and electrodes [324-327] for electrically-controlled drug delivery into rare solid breast tumors.

The design of the iontophoresis on-chip device can be improved in the future by embedding the nanoporous membrane and coculturing epithelial cells for mimicking the skin barrier against iontophoresis chemo delivery. This device has the potential of mimicking combined intravenous and iontophoresis chemotherapy by co-culturing epidermal cells on the embedded membrane between two layers and controlling flow in the device's top layer (**Figure 4.1.1**). 0.4 μm pore size polycarbonate (Corning) membrane was used for mimicking skin pore size in the microfluidic device. The procedure for sandwiching polycarbonate membrane between two PDMS layers (**Figure 4.1.1Cii**) has been described in the literature [100, 328]. Briefly, a liquid PDMS glue, PDMS, and toluene with a 1:1 weight ratio are used for bonding. A clean glass slide is spin-coated (1600 rpm for 60 seconds) with the PDMS glue. The top and bottom PDMS layers placed on the coated glass slide with the features facing down. The PDMS layers are then peeled off the slide, and the polycarbonate membrane cut from a transwell plate (Corning) is embedded between the layers before aligning and bonding the layers together. The assembled device is cured at 65 °C for 10 hours and then punched at inlets and outlets (**Figure 4.1.1C**).

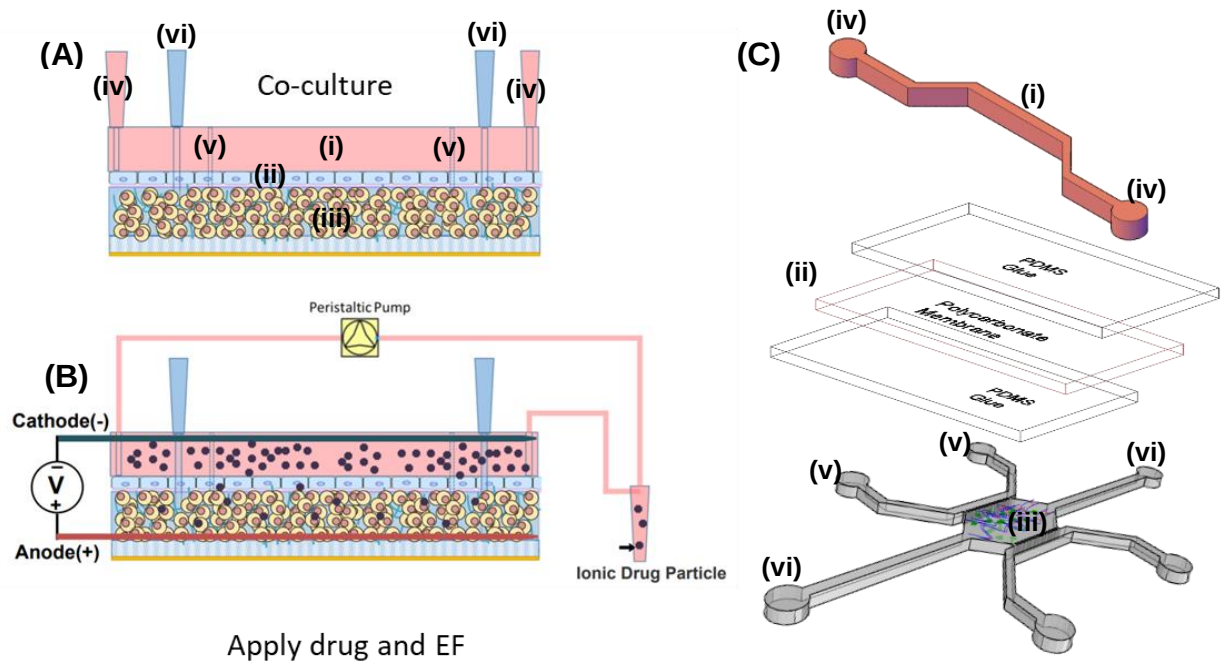

Figure 4.1.1. Chemo-iontophoresis-on-a-chip. (A) breast cancer-epidermal co-culture system for 3D breast cancer culture. **(i)** The microfluidic channel on the top layer of the device mimicking the blood vessel (drug source). **(ii)** Breast epidermal cells cultured on the polycarbonate membrane sandwiched between PDMS glue. **(iii)** 3D cancer cell culture in hydrogel scaffold. **(iv)** Cell medium inlet for the breast epidermal human cells. **(v)** Microfluidic channels are mimicking lymph vessels (drug sink) outlets (**vi)** Breast cancer cells medium inlets. **(B)** Schematic of applying drug and electric field. The flow of drug circulates in the top layer microfluidic cannel. The DC electric field electrodes are inserted to the top layer (cathode) and the bottom layer (anode) to have a horizontal electric field direction to the bottom layer of cancer cells. **(C)** 3D view of breast cancer-epidermal co-culture system. **(i)** The microfluidic channel on the top layer of the device mimicking the blood flow in the blood vessel (drug source). **(ii)** The polycarbonate membrane sandwiched between PDMS glue. **(iii)** 3D cell culture chamber and hydrogel scaffold. **(iv)** Cell medium inlet for the breast epidermal human cells and drug flow inlet and outlets. **(v)** Microfluidic channels are mimicking lymph vessels (drug sink) outlets (**vi)** Breast cancer cells medium inlets.

In the future, the advanced computational fluid dynamics (CFD) model validated with a 3D cell culture system, which is shown in **Figure 4.1.1,** has proven benefits in providing more physiologically relevant conditions and the capability of mimicking biomedical devices for precision cancer treatment. Although many studies have increased our knowledge of the underlying mechanisms of iontophoresis, a computational model

able to predict overall tumor response based on tumor biophysical properties remains elusive. The overarching future goal of the current work is to develop a microfluidic platform and a computational model to define the iontophoresis effects in combination with chemotherapy.

4.2. Cancer electro immunotherapy

Iontophoresis chemotherapy has been recently tested in mice and human models for pancreatic, breast, and skin cancers [90, 329, 330]. Our study shows that the iontophoresis transport model with an *in vitro* microfluidics validation can be used for predicting the outcome of the drug's electro-transport. Besides, the current study also investigates the electromigration of neutrophils toward the inflammation and infection sites. Our study shows that applied electric fields enhanced neutrophil migration toward the cathode, and counter-current electric fields decreased migration toward LTB_4 chemoattractant. The study needs further investigation in the concept of neutrophil cancer cell interaction and how to combine neutrophil electromigration, and iontophoresis chemotherapy to facilitate the local tumor treatment. The iontophoresis on-chip device has the capability of testing new kinds of treatment, such as immune-iontophoresis chemotherapy.

4.3. Sepsis electro-immunotherapy and smart bandage

Sepsis is the severe overaction of the immune system to infections. In this study, we have shown the principles, and *in vitro* investigation of neutrophil electromigration. Smart bandage technology uses an electronic circuit for biosensor and monitoring chronic wounds conditions remotely. Using electric fields for cell migration and drug delivery in wounds can be a novel application of smart bandage in the future, which

facilitates localized delivery of immune cells (e.g., neutrophils) and drug to the site of the infection. Neutrophil isolation with electric field and removal of excess neutrophil form patients can be a novel approach for preventing inflammatory response of immune cells to infection in the healthy tissues

The design of the electro taxis-on- chip microfluidic device should mimic the *in vivo* microenvironment for the use of the microfluidics device in a clinical investigation. In future neutrophil migration *in vitro* studies, researchers can consider other physical migration stimuli such as rheotaxis (fluid flow) and barotaxis (pressure gradient). During the migration of neutrophils toward the chemoattractant, neutrophils squeeze through endothelial cells and microcapillaries due to other migration cues such as rheotaxis or barotaxis. For having a precise investigation of neutrophil migration, the design of electro-chemotaxis on-chip can be improved in future works for addressing the effect combined physical stimuli of neutrophil migration. The design pinches in the individual channels induced pressure and fluid velocity gradient for neutrophils rheotaxis and barotaxis migration and can mimic neutrophil deformation and migration toward physical or chemical stimuli. (**Figure 4.3.1**).

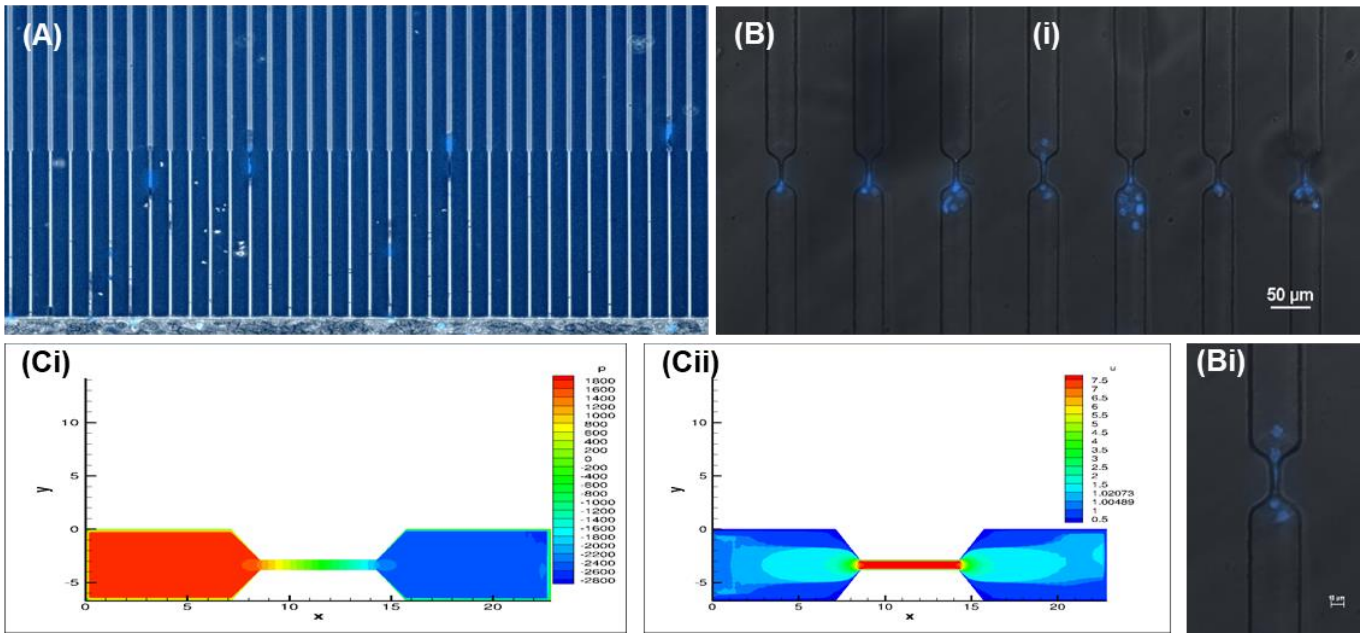

Figure 4.3.1. A. Microfluidic "pinch" device used to measure neutrophil deformability—neutrophils (10-12 µm) have to squeeze through a 2µm channel. Normal neutrophils (blue, DNA stained with Hoechst stain) can deform and squeeze through the channels. **B.** Microfluidic “pinch” device used to measure dHL60 deformability. (i) dHL60 cells squeeze through 7 µm width and 10 µm height. **C.** Computational fluid dynamics modeling of (i) pressure and (ii) fluid velocity in the cell trapping channel using the GENIDLEST finite-difference model code.

Neutrophil deformation and decision making in capillaries vasculature can be investigated by designing a trapping channel and maze in the individual migration channel. First, the CFD simulation in migration channels was preprocessed in the AutoCAD and Pointwise, processed with the GENIDLEST finite-difference model, and post-processed in Techplot **(Figure 4.3.1C)**. Second, the new mold was made by using the photolithography method and PDMS fabrication. Finally, dHL60 was loaded in the microfluidic device using the syringe pump with the defined velocity founded in the CFD simulation **(Figure 4.3.1A&B)**.

REFERENCES

1. Probstein, R.F., *Physicochemical hydrodynamics: an introduction*. 2005: John Wiley & Sons.
2. Kirby, B.J., *Micro-and nanoscale fluid mechanics: transport in microfluidic devices*. 2010: Cambridge university press.
3. Proctor, C.M., et al., *Electrophoretic drug delivery for seizure control.* Science Advances, 2018. **4**(8): p. eaau1291.
4. Pikal, M.J., *The role of electroosmotic flow in transdermal iontophoresis.* Advanced Drug Delivery Reviews, 2001. **46**(1): p. 281-305.
5. Marro, D., et al., *Contributions of electromigration and electroosmosis to iontophoretic drug delivery.* Pharm Res, 2001. **18**(12): p. 1701-8.
6. D'Emanuele, A. and J.N. Staniforth, *Effects of polymer formulation on electrophoretic drug delivery.* International Journal of Pharmaceutics, 1993. **92**(1): p. 225-231.
7. Karpiński, T., *Selected Medicines Used in Iontophoresis.* Pharmaceutics, 2018. **10**(4): p. 204.
8. Cortese, B., et al., *Influence of electrotaxis on cell behaviour.* Integr Biol (Camb), 2014. **6**(9): p. 817-30.
9. Menon, N., et al., *Heparin-based hydrogel scaffolding alters the transcriptomic profile and increases the chemoresistance of MDA-MB-231 triple-negative breast cancer cells.* Biomaterials Science, 2020.
10. Bonazzi, D. and N. Minc, *Dissecting the Molecular Mechanisms of Electrotactic Effects.* Advances in wound care, 2014. **3**(2): p. 139-148.
11. Mycielska, M.E. and M.B. Djamgoz, *Cellular mechanisms of direct-current electric field effects: galvanotaxis and metastatic disease.* Journal of cell science, 2004. **117**(9): p. 1631-1639.
12. Huang, Y.-J., et al., *Electrophoresis of cell membrane heparan sulfate regulates galvanotaxis in glial cells.* J Cell Sci, 2017. **130**(15): p. 2459-2467.
13. Boribong, B.P., A. Rahimi, and C.N. Jones, *Microfluidic Platform to Quantify Neutrophil Migratory Decision-Making.* Methods Mol Biol, 2019. **1960**: p. 113-122.
14. McGuire, M.F., et al., *Formalizing an Integrative, Multidisciplinary Cancer Therapy Discovery Workflow.* Cancer Research, 2013. **73**(20): p. 6111.
15. Enderling, H. and K. Rejniak, *Simulating Cancer: Computational Models in Oncology.* Frontiers in Oncology, 2013. **3**(233).
16. Choe, S.C., et al., *Model for in vivo progression of tumors based on co-evolving cell population and vasculature.* Scientific Reports, 2011. **1**: p. 31.
17. Frieboes, H.B., et al., *Physical Oncology: A Bench-to-Bedside Quantitative and Predictive Approach.* Cancer Research, 2011. **71**(2): p. 298.
18. Liu, C., et al., *Use of mathematical models to understand anticancer drug delivery and its effect on solid tumors.* Pharmacogenomics, 2011. **12**(9): p. 1337-1348.
19. Michor, F., et al., *What does physics have to do with cancer?* Nature Reviews Cancer, 2011. **11**: p. 657.
20. Byrne, H.M., *Dissecting cancer through mathematics: from the cell to the animal model.* Nature Reviews Cancer, 2010. **10**: p. 221.
21. Swierniak, A., M. Kimmel, and J. Smieja, *Mathematical modeling as a tool for planning anticancer therapy.* European Journal of Pharmacology, 2009. **625**(1): p. 108-121.
22. Kim, M., R. Gillies, and K. Rejniak, *Current Advances in Mathematical Modeling of Anti-Cancer Drug Penetration into Tumor Tissues.* Frontiers in Oncology, 2013. **3**(278).
23. Davoodi, P., et al., *Drug delivery systems for programmed and on-demand release.* Advanced drug delivery reviews, 2018. **132**: p. 104-138.

24. Siepmann, J. and F. Siepmann, *Mathematical modeling of drug delivery.* International Journal of Pharmaceutics, 2008. **364**(2): p. 328-343.
25. Aroesty, J., et al., *Tumor growth and chemotherapy: Mathematical methods, computer simulations, and experimental foundations.* Mathematical Biosciences, 1973. **17**(3–4): p. 243-300.
26. Siepmann, J. and F. Siepmann, *Modeling of diffusion controlled drug delivery.* Journal of Controlled Release, 2012. **161**(2): p. 351-362.
27. Mircioiu, C., et al., *Mathematical Modeling of Release Kinetics from Supramolecular Drug Delivery Systems.* Pharmaceutics, 2019. **11**(3): p. 140.
28. Pascal, J., et al., *Mechanistic patient-specific predictive correlation of tumor drug response with microenvironment and perfusion measurements.* Proceedings of the National Academy of Sciences, 2013. **110**(35): p. 14266-14271.
29. Moarefian, M. and J.A. Pascal, *Fundamental mathematical model shows that applied electrical field enhances chemotherapy delivery to tumors.* Mathematical biosciences, 2016. **272**: p. 1-5.
30. Whitesides, G.M., *The origins and the future of microfluidics.* Nature, 2006. **442**(7101): p. 368-373.
31. Nguyen, N.-T., S.T. Wereley, and S.A.M. Shaegh, *Fundamentals and applications of microfluidics*. 2019: Artech house.
32. Gravesen, P., J. Branebjerg, and O.S. Jensen, *Microfluidics-a review.* Journal of Micromechanics and Microengineering, 1993. **3**(4): p. 168-182.
33. Neukermans, A.P., *Microfluidic valve and integrated microfluidic system*. 2000, Google Patents.
34. Jensen, O.S. and P. Gravesen, *Flow characteristics of a micromachined diaphragm valve designed for liquid flows above 1 ml min-1.* Journal of Micromechanics and Microengineering, 1993. **3**(4): p. 236-238.
35. Sobek, D., et al. *A microfabricated flow chamber for optical measurements in fluids*. in *[1993] Proceedings IEEE Micro Electro Mechanical Systems*. 1993.
36. Kamholz, A.E. and P. Yager, *Theoretical analysis of molecular diffusion in pressure-driven laminar flow in microfluidic channels.* Biophysical journal, 2001. **80**(1): p. 155-160.
37. Gass, V., B.H.v.d. Schoot, and N.F.d. Rooij. *Nanofluid handling by micro-flow-sensor based on drag force measurements*. in *[1993] Proceedings IEEE Micro Electro Mechanical Systems*. 1993.
38. Marriott, P.J., et al., *Multidimensional gas chromatography.* TrAC Trends in Analytical Chemistry, 2012. **34**: p. 1-21.
39. Yin, H., et al., *Microfluidic chip for peptide analysis with an integrated HPLC column, sample enrichment column, and nanoelectrospray tip.* Analytical Chemistry, 2005. **77**(2): p. 527-533.
40. Dolník, V., S. Liu, and S. Jovanovich, *Capillary electrophoresis on microchip.* ELECTROPHORESIS: An International Journal, 2000. **21**(1): p. 41-54.
41. Grossman, P.D. and J.C. Colburn, *Capillary electrophoresis: Theory and practice*. 2012: Academic Press.
42. McDonald, J.C., et al., *Fabrication of microfluidic systems in poly(dimethylsiloxane).* ELECTROPHORESIS, 2000. **21**(1): p. 27-40.
43. Schulte, T.H., R.L. Bardell, and B.H. Weigl, *Microfluidic technologies in clinical diagnostics.* Clinica Chimica Acta, 2002. **321**(1): p. 1-10.
44. Wang, Z., et al., *Organ-on-a-chip platforms for drug delivery and cell characterization: A review.* Sens. Mater, 2015. **27**(6): p. 487-506.
45. Zheng, F., et al., *Organ-on-a-Chip Systems: Microengineering to Biomimic Living Systems.* Small, 2016. **12**(17): p. 2253-2282.
46. Lee, H., et al., *A pumpless multi-organ-on-a-chip (MOC) combined with a pharmacokinetic–pharmacodynamic (PK–PD) model.* Biotechnology and Bioengineering, 2017. **114**(2): p. 432-443.

47. Lee, J.B. and J.H. Sung, *Organ-on-a-chip technology and microfluidic whole-body models for pharmacokinetic drug toxicity screening.* Biotechnology Journal, 2013. **8**(11): p. 1258-1266.
48. Selimović, Š., M.R. Dokmeci, and A. Khademhosseini, *Organs-on-a-chip for drug discovery.* Current Opinion in Pharmacology, 2013. **13**(5): p. 829-833.
49. Marimuthu, M., et al., *Multi-size spheroid formation using microfluidic funnels.* Lab on a Chip, 2017.
50. Mu, X., et al., *Engineering a 3D vascular network in hydrogel for mimicking a nephron.* Lab on a Chip, 2013. **13**(8): p. 1612-1618.
51. Kim, C., et al., *A quantitative microfluidic angiogenesis screen for studying anti-angiogenic therapeutic drugs.* Lab on a chip, 2015. **15**(1): p. 301-310.
52. Wang, X.-Y., et al., *Engineering interconnected 3D vascular networks in hydrogels using molded sodium alginate lattice as the sacrificial template.* Lab on a Chip, 2014. **14**(15): p. 2709-2716.
53. Yeon, J.H., et al., *In vitro formation and characterization of a perfusable three-dimensional tubular capillary network in microfluidic devices.* Lab on a Chip, 2012. **12**(16): p. 2815-2822.
54. Kim, S., et al., *Interstitial flow regulates the angiogenic response and phenotype of endothelial cells in a 3D culture model.* Lab on a Chip, 2016. **16**(21): p. 4189-4199.
55. Siegel, R.L., K.D. Miller, and A. Jemal, *Cancer statistics, 2020.* CA: A Cancer Journal for Clinicians, 2020. **70**(1): p. 7-30.
56. Siegel, R., et al., *Cancer statistics, 2014.* CA: a cancer journal for clinicians, 2014. **64**(1): p. 9-29.
57. Yu, T., et al., *Cancer-associated fibroblasts promote non-small cell lung cancer cell invasion by upregulation of glucose-regulated protein 78 (GRP78) expression in an integrated bionic microfluidic device.* Oncotarget, 2016. **7**(18): p. 25593-603.
58. Sleeboom, J.J.F., et al., *Metastasis in context: modeling the tumor microenvironment with cancer-on-a-chip approaches.* Disease Models & Mechanisms, 2018. **11**(3): p. dmm033100.
59. Chung, M., et al., *Biomimetic Model of Tumor Microenvironment on Microfluidic Platform.* Advanced Healthcare Materials, 2017. **6**(15): p. 1700196.
60. Lei, K.F., et al., *Quantitative Study of Cell Invasion Process under Extracellular Stimulation of Cytokine in a Microfluidic Device.* Scientific Reports, 2016. **6**(1): p. 25557.
61. Bischel, L.L., et al., *A microfluidic coculture and multiphoton FAD analysis assay provides insight into the influence of the bone microenvironment on prostate cancer cells.* Integrative Biology, 2014. **6**(6): p. 627-635.
62. Choi, Y., et al., *A microengineered pathophysiological model of early-stage breast cancer.* Lab on a Chip, 2015. **15**(16): p. 3350-3357.
63. Acosta, M.A., et al., *A microfluidic device to study cancer metastasis under chronic and intermittent hypoxia.* Biomicrofluidics, 2014. **8**(5): p. 054117.
64. Kwak, B., et al., *Simulation of complex transport of nanoparticles around a tumor using tumor-microenvironment-on-chip.* Journal of Controlled Release, 2014. **194**: p. 157-167.
65. Lee, H., et al., *Device-assisted transdermal drug delivery.* Adv Drug Deliv Rev, 2018. **127**: p. 35-45.
66. DeSantis, C.E., et al., *Breast cancer statistics, 2019.* CA: A Cancer Journal for Clinicians, 2019. **69**(6): p. 438-451.
67. Kalimutho, M., et al., *Targeted therapies for triple-negative breast cancer: combating a stubborn disease.* Trends in pharmacological sciences, 2015. **36**(12): p. 822-846.
68. Mustacchi, G. and M. De Laurentiis, *The role of taxanes in triple-negative breast cancer: literature review.* Drug design, development and therapy, 2015. **9**: p. 4303-4318.
69. Chacón, R.D. and M.V. Costanzo, *Triple-negative breast cancer.* Breast cancer research : BCR, 2010. **12 Suppl 2**(Suppl 2): p. S3-S3.

70. Kumar, N., *Taxol-induced polymerization of purified tubulin. Mechanism of action.* Journal of Biological Chemistry, 1981. **256**(20): p. 10435-10441.
71. Caplow, M., J. Shanks, and R. Ruhlen, *How taxol modulates microtubule disassembly.* Journal of Biological Chemistry, 1994. **269**(38): p. 23399-23402.
72. Díaz, J.F., I. Barasoain, and J.M. Andreu, *Fast kinetics of taxol binding to microtubules effects of solution variables and microtubule-associated proteins.* Journal of Biological Chemistry, 2003. **278**(10): p. 8407-8419.
73. Díaz, J.F., et al., *Molecular recognition of Taxol by microtubules kinetics and thermodynamics of binding of fluorescent Taxol derivatives to an exposed site.* Journal of Biological Chemistry, 2000. **275**(34): p. 26265-26276.
74. Kuh, H.-J., et al., *Determinants of paclitaxel penetration and accumulation in human solid tumor.* Journal of Pharmacology and Experimental Therapeutics, 1999. **290**(2): p. 871-880.
75. Karginova, O., et al., *Efficacy of Carboplatin Alone and in Combination with ABT888 in Intracranial Murine Models of BRCA-Mutated and BRCA-Wild-Type Triple-Negative Breast Cancer.* Molecular cancer therapeutics, 2015. **14**(4): p. 920-930.
76. Bartelink, I.H., et al., *Heterogeneous drug penetrance of veliparib and carboplatin measured in triple negative breast tumors.* Breast cancer research : BCR, 2017. **19**(1): p. 107-107.
77. Yardley, D.A., et al., *Phase II/III weekly nab-paclitaxel plus gemcitabine or carboplatin versus gemcitabine/carboplatin as first-line treatment of patients with metastatic triple-negative breast cancer (the tnAcity study): study protocol for a randomized controlled trial.* Trials, 2015. **16**: p. 575-575.
78. Ogata, H., et al., *Liver Metastasis of a Triple-Negative Breast Cancer and Complete Remission for 5 Years After Treatment With Combined Bevacizumab/Paclitaxel/Carboplatin: Case Report and Review of the Literature.* Medicine, 2015. **94**(42): p. e1756-e1756.
79. Schmidt, G., et al., *Electrochemotherapy in Breast Cancer: A Review of References.* Geburtshilfe und Frauenheilkunde, 2014. **74**(6): p. 557-562.
80. Yang, W., et al., *Convection enhanced delivery of carboplatin in combination with radiotherapy for the treatment of brain tumors.* Journal of neuro-oncology, 2011. **101**(3): p. 379-390.
81. Di Pasqua, A.J., et al., *Activation of Carboplatin by Carbonate.* Chemical Research in Toxicology, 2006. **19**(1): p. 139-149.
82. Ciancetta, A., et al., *Activation of carboplatin by carbonate: A theoretical investigation*. Vol. 41. 2012. 12960-9.
83. Prausnitz, M.R. and R. Langer, *Transdermal drug delivery.* Nat Biotechnol, 2008. **26**(11): p. 1261-8.
84. Barry, B.W., *Novel mechanisms and devices to enable successful transdermal drug delivery.* European Journal of Pharmaceutical Sciences, 2001. **14**(2): p. 101-114.
85. Lee, H., et al., *Device-assisted transdermal drug delivery.* Advanced drug delivery reviews, 2018. **127**: p. 35-45.
86. Arora, A., M.R. Prausnitz, and S. Mitragotri, *Micro-scale devices for transdermal drug delivery.* International journal of pharmaceutics, 2008. **364**(2): p. 227-236.
87. Paudel, K.S., et al., *Challenges and opportunities in dermal/transdermal delivery.* Therapeutic delivery, 2010. **1**(1): p. 109-131.
88. Mofidfar, M., *POLYMERIC NANOFIBER/ANTIMICROBIAL FORMULATIONS USING A NOVEL CO-EXTRUSION APPROACH COMPARED WITH ELECTROSPINNING FOR TRANSDERMAL DRUG DELIVERY APPLICATIONS*. 2016, Case Western Reserve University School of Graduate Studies.
89. Byrne, J.D., et al., *Local iontophoretic administration of cytotoxic therapies to solid tumors.* Science Translational Medicine, 2015. **7**(273): p. 273ra14.

90. Byrne, J.D., J.J. Yeh, and J.M. DeSimone, *Use of iontophoresis for the treatment of cancer.* Journal of Controlled Release, 2018. **284**: p. 144-151.
91. Tsuji, T., *Bleomycin iontophoretic therapy for verrucous carcinoma.* Archives of dermatology, 1991. **127**(7): p. 973-975.
92. Chang, C.-C., et al., *LIPOSOMAL CURCUMINOIDS FOR TRANSDERMAL DELIVERY: IONTOPHORESIS POTENTIAL FOR BREAST CANCER CHEMOTHERAPEUTICS.* Digest Journal of Nanomaterials & Biostructures (DJNB), 2012. **7**(1).
93. DeSimone, J., J. Tepper, and J. Byrne, *Combined local delivery of therapeutic agents using interventional devices and radiation*. 2020, Google Patents.
94. Neumann, E., et al., *Gene transfer into mouse lyoma cells by electroporation in high electric fields.* The EMBO journal, 1982. **1**(7): p. 841.
95. OKINO, M. and H. MOHRI, *Effects of a high-voltage electrical impulse and an anticancer drug on in vivo growing tumors.* Japanese Journal of Cancer Research GANN, 1987. **78**(12): p. 1319-1321.
96. Orlowski, S., et al., *Transient electropermeabilization of cells in culture: increase of the cytotoxicity of anticancer drugs.* Biochemical pharmacology, 1988. **37**(24): p. 4727-4733.
97. Kennedy, S., et al., *Quantification of electroporative uptake kinetics and electric field heterogeneity effects in cells.* Biophysical journal, 2008. **94**(12): p. 5018-5027.
98. Kennedy, S.M., et al., *Cationic peptide exposure enhances pulsed-electric-field-mediated membrane disruption.* PloS one, 2014. **9**(3): p. e92528.
99. Sadik, M.M., et al., *Quantification of propidium iodide delivery using millisecond electric pulses: experiments.* Biochimica et Biophysica Acta (BBA)-Biomembranes, 2013. **1828**(4): p. 1322-1328.
100. Bonakdar, M., P. Graybill, and R. Davalos, *A microfluidic model of the blood–brain barrier to study permeabilization by pulsed electric fields.* RSC advances, 2017. **7**(68): p. 42811-42818.
101. Bonakdar, M., et al., *Electroporation of Brain Endothelial Cells on Chip toward Permeabilizing the Blood-Brain Barrier.* Biophysical Journal, 2016. **110**(2): p. 503-513.
102. Banerjee, A., et al., *Intestinal iontophoresis from mucoadhesive patches: a strategy for oral delivery.* Journal of Controlled Release, 2019. **297**: p. 71-78.
103. Dalmolin, L.F. and R.F.V. Lopez, *Nanoemulsion as a Platform for Iontophoretic Delivery of Lipophilic Drugs in Skin Tumors.* Pharmaceutics, 2018. **10**(4): p. 214.
104. Liang, H., et al., *Effects of methycobal iontophoresis combined with balance acupuncture on peripheral facial paralysis.* Zhongguo zhen jiu= Chinese acupuncture & moxibustion, 2018. **38**(9): p. 955-960.
105. Banga, A.K., *Electrically assisted transdermal and topical drug delivery*. 1998: CRC Press.
106. Kalia, Y.N., et al., *Iontophoretic drug delivery.* Advanced drug delivery reviews, 2004. **56**(5): p. 619-658.
107. Prausnitz, M.R., *The effects of electric current applied to skin: a review for transdermal drug delivery.* Advanced Drug Delivery Reviews, 1996. **18**(3): p. 395-425.
108. Meer, A.D.v.d., et al., *A microfluidic wound-healing assay for quantifying endothelial cell migration.* American Journal of Physiology-Heart and Circulatory Physiology, 2010. **298**(2): p. H719-H725.
109. McDougall, S., et al., *Fibroblast migration and collagen deposition during dermal wound healing: mathematical modelling and clinical implications.* Philosophical Transactions of the Royal Society A: Mathematical, Physical and Engineering Sciences, 2006. **364**(1843): p. 1385-1405.
110. Zhao, M., *Electrical fields in wound healing-An overriding signal that directs cell migration.* Semin Cell Dev Biol, 2009. **20**(6): p. 674-82.
111. Trapiella-Alfonso, L., et al., *Electromigration separation methodologies for the characterization of nanoparticles and the evaluation of their behaviour in biological systems.* TrAC Trends in Analytical Chemistry, 2016. **84**: p. 121-130.

112. Pasquali, C., I. Fialka, and L.A. Huber, *Subcellular fractionation, electromigration analysis and mapping of organelles.* Journal of Chromatography B: Biomedical Sciences and Applications, 1999. **722**(1): p. 89-102.
113. Yamaguchi, H., J. Wyckoff, and J. Condeelis, *Cell migration in tumors.* Current Opinion in Cell Biology, 2005. **17**(5): p. 559-564.
114. Wolf, K., et al., *Compensation mechanism in tumor cell migration: mesenchymal–amoeboid transition after blocking of pericellular proteolysis.* The Journal of cell biology, 2003. **160**(2): p. 267-277.
115. Sahai, E. and C.J. Marshall, *Differing modes of tumour cell invasion have distinct requirements for Rho/ROCK signalling and extracellular proteolysis.* Nature cell biology, 2003. **5**(8): p. 711-719.
116. Friedl, P. and K. Wolf, *Tumour-cell invasion and migration: diversity and escape mechanisms.* Nature reviews cancer, 2003. **3**(5): p. 362-374.
117. Luster, A.D., R. Alon, and U.H. von Andrian, *Immune cell migration in inflammation: present and future therapeutic targets.* Nature immunology, 2005. **6**(12): p. 1182-1190.
118. Harris, H., *Role of Chemotaxis in Inflammation.* Physiological Reviews, 1954. **34**(3): p. 529-562.
119. Herbison, R.E.H., et al., *Let's go swimming: mermithid-infected earwigs exhibit positive hydrotaxis.* Parasitology, 2019: p. 1-5.
120. Wang, W., et al., *cGMP Signalling Mediates Water Sensation (Hydrosensation) and Hydrotaxis in Caenorhabditis elegans.* Scientific Reports, 2016. **6**: p. 19779.
121. Abed, R.M., et al., *Rapid recovery of cyanobacterial pigments in desiccated biological soil crusts following addition of water.* PLoS One, 2014. **9**(11): p. e112372.
122. Pringault, O. and F. Garcia-Pichel, *Hydrotaxis of cyanobacteria in desert crusts.* Microb Ecol, 2004. **47**(4): p. 366-73.
123. Nakagaki, T., et al., *Action spectrum for sporulation and photoavoidance in the plasmodium of Physarum polycephalum, as modified differentially by temperature and starvation.* Photochem Photobiol, 1996. **64**(5): p. 859-62.
124. Kim, J.Y., et al., *Microfluidic high-throughput selection of microalgal strains with superior photosynthetic productivity using competitive phototaxis.* Sci Rep, 2016. **6**: p. 21155.
125. Lin, F.Y., et al., *Use Microfluidic Chips to Study the Phototaxis of Lung Cancer Cells.* Int J Mol Sci, 2019. **20**(18).
126. Ozasa, K., et al., *Two-dimensional optical feedback control of Euglena confined in closed-type microfluidic channels.* Lab Chip, 2011. **11**(11): p. 1933-40.
127. Sung, Y.J., et al., *Two-Dimensional Microfluidic System for the Simultaneous Quantitative Analysis of Phototactic/Chemotactic Responses of Microalgae.* Anal Chem, 2018. **90**(23): p. 14029-14038.
128. Moreau, H.D., et al., *Macropinocytosis Overcomes Directional Bias in Dendritic Cells Due to Hydraulic Resistance and Facilitates Space Exploration.* Dev Cell, 2019. **49**(2): p. 171-188.e5.
129. Prentice-Mott, H.V., et al., *Biased migration of confined neutrophil-like cells in asymmetric hydraulic environments.* Proc Natl Acad Sci U S A, 2013. **110**(52): p. 21006-11.
130. Simon, P., R. Dupuis, and J. Costentin, *Thigmotaxis as an index of anxiety in mice. Influence of dopaminergic transmissions.* Behav Brain Res, 1994. **61**(1): p. 59-64.
131. Kvist, S.B. and R.K. Selander, *Maze-running and thigmotaxis in mice: applicability of models across the sexes.* Scand J Psychol, 1992. **33**(4): p. 378-84.
132. Svoboda, J., et al., *Comparison of male and female rats in avoidance of a moving object: more thigmotaxis, hypolocomotion and fear-like reactions in females.* Physiol Res, 2012. **61**(6): p. 659-63.
133. Bollmann, L., et al., *Microglia mechanics: immune activation alters traction forces and durotaxis.* Front Cell Neurosci, 2015. **9**: p. 363.

134. Li, S., N.F. Huang, and S. Hsu, *Mechanotransduction in endothelial cell migration.* J Cell Biochem, 2005. **96**(6): p. 1110-26.
135. Lin, X. and B.P. Helmke, *Cell Structure Controls Endothelial Cell Migration under Fluid Shear Stress.* Cell Mol Bioeng, 2009. **2**(2): p. 231-243.
136. Mousavi, S.J., M.H. Doweidar, and M. Doblare, *Cell migration and cell-cell interaction in the presence of mechano-chemo-thermotaxis.* Mol Cell Biomech, 2013. **10**(1): p. 1-25.
137. Ueki, A. and S. Kidoaki, *Manipulation of cell mechanotaxis by designing curvature of the elasticity boundary on hydrogel matrix.* Biomaterials, 2015. **41**: p. 45-52.
138. Valignat, M.P., et al., *Lymphocytes can self-steer passively with wind vane uropods.* Nat Commun, 2014. **5**: p. 5213.
139. Roca-Cusachs, P., R. Sunyer, and X. Trepat, *Mechanical guidance of cell migration: lessons from chemotaxis.* Curr Opin Cell Biol, 2013. **25**(5): p. 543-9.
140. Hadden, W.J., et al., *Stem cell migration and mechanotransduction on linear stiffness gradient hydrogels.* Proc Natl Acad Sci U S A, 2017. **114**(22): p. 5647-5652.
141. Maritzen, T., H. Schachtner, and D.F. Legler, *On the move: endocytic trafficking in cell migration.* Cell Mol Life Sci, 2015. **72**(11): p. 2119-34.
142. Sadati, M., et al., *Collective migration and cell jamming.* Differentiation, 2013. **86**(3): p. 121-5.
143. Yu, S., et al., *Preparation of an Arg-Glu-Asp-Val Peptide Density Gradient on Hyaluronic Acid-Coated Poly(epsilon-caprolactone) Film and Its Influence on the Selective Adhesion and Directional Migration of Endothelial Cells.* ACS Appl Mater Interfaces, 2016. **8**(43): p. 29280-29288.
144. Hader, D.P. and R. Hemmersbach, *Gravitaxis in Euglena.* Adv Exp Med Biol, 2017. **979**: p. 237-266.
145. Katz, D.F. and L. Pedrotti, *Geotaxis by motile spermatozoa: Hydrodynamic reorientation.* J Theor Biol, 1977. **67**(4): p. 723-32.
146. Roberts, A.M., *Geotaxis in motile micro-organisms.* J Exp Biol, 1970. **53**(3): p. 687-99.
147. Stoltenberg, S.F. and J. Hirsch, *Y-chromosome effects on Drosophila geotaxis interact with genetic or cytoplasmic background.* Anim Behav, 1997. **53**(Pt 4): p. 853-64.
148. Weinersmith, K.L., et al., *Euhaplorchis californiensis Cercariae Exhibit Positive Phototaxis and Negative Geotaxis.* J Parasitol, 2018. **104**(3): p. 329-333.
149. Oteiza, P., et al., *A novel mechanism for mechanosensory-based rheotaxis in larval zebrafish.* Nature, 2017. **547**(7664): p. 445-448.
150. Palacci, J., et al., *Artificial rheotaxis.* Sci Adv, 2015. **1**(4): p. e1400214.
151. Peimani, A.R., G. Zoidl, and P. Rezai, *A microfluidic device for quantitative investigation of zebrafish larvae's rheotaxis.* Biomed Microdevices, 2017. **19**(4): p. 99.
152. Ren, L., et al., *Rheotaxis of Bimetallic Micromotors Driven by Chemical-Acoustic Hybrid Power.* ACS Nano, 2017. **11**(10): p. 10591-10598.
153. Zhang, Z., et al., *Human sperm rheotaxis: a passive physical process.* Sci Rep, 2016. **6**: p. 23553.
154. de Araujo, F.F., et al., *Magnetite and magnetotaxis in algae.* Biophys J, 1986. **50**(2): p. 375-8.
155. Frankel, R.B. and R.P. Blakemore, *Magnetite and magnetotaxis in microorganisms.* Bioelectromagnetics, 1989. **10**(3): p. 223-37.
156. Lefevre, C.T. and L.F. Wu, *Evolution of the bacterial organelle responsible for magnetotaxis.* Trends Microbiol, 2013. **21**(10): p. 534-43.
157. Lin, W., et al., *Genomic expansion of magnetotactic bacteria reveals an early common origin of magnetotaxis with lineage-specific evolution.* Isme j, 2018. **12**(6): p. 1508-1519.
158. Monteil, C.L., et al., *Genomic study of a novel magnetotactic Alphaproteobacteria uncovers the multiple ancestry of magnetotaxis.* Environ Microbiol, 2018. **20**(12): p. 4415-4430.

159. Rismani Yazdi, S., et al., *Magnetotaxis Enables Magnetotactic Bacteria to Navigate in Flow.* Small, 2018. **14**(5).
160. Rismani Yazi, S., et al., *Migration of magnetotactic bacteria in porous media.* Biomicrofluidics, 2018. **12**(1): p. 011101.
161. Arocena, M., et al., *A time-lapse and quantitative modelling analysis of neural stem cell motion in the absence of directional cues and in electric fields.* J Neurosci Res, 2010. **88**(15): p. 3267-74.
162. Berthelot, R., K. Doxsee, and S. Neethirajan, *Electroceutical Approach for Impairing the Motility of Pathogenic Bacterium Using a Microfluidic Platform.* Micromachines (Basel), 2017. **8**(7).
163. Feng, J.F., et al., *Guided migration of neural stem cells derived from human embryonic stem cells by an electric field.* Stem Cells, 2012. **30**(2): p. 349-55.
164. Feng, L. and T.J. Kamp, *Electrotaxis leads the way.* Heart Rhythm, 2017. **14**(11): p. 1693-1694.
165. Frederich, B.J., et al., *Electrotaxis of cardiac progenitor cells, cardiac fibroblasts, and induced pluripotent stem cell-derived cardiac progenitor cells requires serum and is directed via PI3'K pathways.* Heart Rhythm, 2017. **14**(11): p. 1685-1692.
166. Gao, R.C., et al., *Different roles of membrane potentials in electrotaxis and chemotaxis of dictyostelium cells.* Eukaryot Cell, 2011. **10**(9): p. 1251-6.
167. Hou, H.S., H.F. Chang, and J.Y. Cheng, *Electrotaxis Studies of Lung Cancer Cells using a Multichannel Dual-electric-field Microfluidic Chip.* J Vis Exp, 2015(106): p. e53340.
168. Jezierska-Wozniak, K., et al., *Migration of human mesenchymal stem cells stimulated with pulsed electric field and the dynamics of the cell surface glycosylation.* Adv Clin Exp Med, 2018. **27**(9): p. 1181-1193.
169. Kao, Y.C., et al., *Modulating chemotaxis of lung cancer cells by using electric fields in a microfluidic device.* Biomicrofluidics, 2014. **8**(2): p. 024107.
170. Kim, M.S., et al., *Golgi polarization plays a role in the directional migration of neonatal dermal fibroblasts induced by the direct current electric fields.* Biochem Biophys Res Commun, 2015. **460**(2): p. 255-60.
171. Kim, M.S., et al., *Effects of direct current electric-field using ITO plate on breast cancer cell migration.* Biomater Res, 2014. **18**: p. 10.
172. Kim, M.S., et al., *Control of neonatal human dermal fibroblast migration on poly(lactic-co-glycolic acid)-coated surfaces by electrotaxis.* J Tissue Eng Regen Med, 2017. **11**(3): p. 862-868.
173. Li, F., et al., *Superoxide mediates direct current electric field-induced directional migration of glioma cells through the activation of AKT and ERK.* PLoS One, 2013. **8**(4): p. e61195.
174. Li, J. and F. Lin, *Microfluidic devices for studying chemotaxis and electrotaxis.* Trends Cell Biol, 2011. **21**(8): p. 489-97.
175. Li, J., et al., *Activated T lymphocytes migrate toward the cathode of DC electric fields in microfluidic devices.* Lab Chip, 2011. **11**(7): p. 1298-304.
176. Li, J., et al., *Microfluidic device for studying cell migration in single or co-existing chemical gradients and electric fields.* Biomicrofluidics, 2012. **6**(2): p. 24121-2412113.
177. Li, L., et al., *Electric fields guide migration of epidermal stem cells and promote skin wound healing.* Wound Repair Regen, 2012. **20**(6): p. 840-51.
178. Li, L., et al., *Caveolin-1-mediated STAT3 activation determines electrotaxis of human lung cancer cells.* Oncotarget, 2017. **8**(56): p. 95741-95754.
179. Li, S., et al., *Electrical Stimulation Activates Fibroblasts through the Elevation of Intracellular Free Ca(2+): Potential Mechanism of Pelvic Electrical Stimulation Therapy.* Biomed Res Int, 2019. **2019**: p. 7387803.
180. Li, Y., et al., *Effects of direct current electric fields on lung cancer cell electrotaxis in a PMMA-based microfluidic device.* Anal Bioanal Chem, 2017. **409**(8): p. 2163-2178.
181. Lin, F., et al., *Lymphocyte electrotaxis in vitro and in vivo.* J Immunol, 2008. **181**(4): p. 2465-71.

182. Lyon, J.G., et al., *Electrotaxis of Glioblastoma and Medulloblastoma Spheroidal Aggregates.* Sci Rep, 2019. **9**(1): p. 5309.
183. Mishra, S., et al., *A novel electro-chemotactic approach to impact the directional migration of transplantable retinal progenitor cells.* Exp Eye Res, 2019. **185**: p. 107688.
184. Mousavi, S.J., M.H. Doweidar, and M. Doblare, *3D computational modelling of cell migration: a mechano-chemo-thermo-electrotaxis approach.* J Theor Biol, 2013. **329**: p. 64-73.
185. Nakajima, K.I., M. Tatsumi, and M. Zhao, *An Essential and Synergistic Role of Purinergic Signaling in Guided Migration of Corneal Epithelial Cells in Physiological Electric Fields.* Cell Physiol Biochem, 2019. **52**(2): p. 198-211.
186. Rezai, P., et al., *Electrical sorting of Caenorhabditis elegans.* Lab Chip, 2012. **12**(10): p. 1831-40.
187. Sato, M.J., et al., *Switching direction in electric-signal-induced cell migration by cyclic guanosine monophosphate and phosphatidylinositol signaling.* Proc Natl Acad Sci U S A, 2009. **106**(16): p. 6667-72.
188. Shibib, K., et al., *Polarization of nerve regeneration (electrotaxis).* Surg Neurol, 1988. **29**(5): p. 372-88.
189. Simpson, M.J., K.Y. Lo, and Y.S. Sun, *Quantifying the roles of random motility and directed motility using advection-diffusion theory for a 3T3 fibroblast cell migration assay stimulated with an electric field.* BMC Syst Biol, 2017. **11**(1): p. 39.
190. Sroka, J., et al., *Electrotaxis: Cell Directional Movement in Electric Fields.* Methods Mol Biol, 2018. **1749**: p. 325-340.
191. Sun, Y.S., *Studying Electrotaxis in Microfluidic Devices.* Sensors (Basel), 2017. **17**(9).
192. Sun, Y.S., S.W. Peng, and J.Y. Cheng, *In vitro electrical-stimulated wound-healing chip for studying electric field-assisted wound-healing process.* Biomicrofluidics, 2012. **6**(3): p. 34117.
193. Sun, Y.S., et al., *Electrotaxis of lung cancer cells in ordered three-dimensional scaffolds.* Biomicrofluidics, 2012. **6**(1): p. 14102-1410214.
194. Tong, J., et al., *Microfluidic-based electrotaxis for on-demand quantitative analysis of Caenorhabditis elegans' locomotion.* J Vis Exp, 2013(75): p. e50226.
195. van West, P., et al., *Oomycete plant pathogens use electric fields to target roots.* Mol Plant Microbe Interact, 2002. **15**(8): p. 790-8.
196. Wu, D., X. Ma, and F. Lin, *DC electric fields direct breast cancer cell migration, induce EGFR polarization, and increase the intracellular level of calcium ions.* Cell Biochem Biophys, 2013. **67**(3): p. 1115-25.
197. Wu, J. and F. Lin, *Recent Developments in Electrotaxis Assays.* Adv Wound Care (New Rochelle), 2014. **3**(2): p. 149-155.
198. Zhao, M., J. Penninger, and R.R. Isseroff, *Electrical Activation of Wound-Healing Pathways.* Adv Skin Wound Care, 2010. **1**: p. 567-573.
199. Zhao, M., et al., *Membrane lipids, EGF receptors, and intracellular signals colocalize and are polarized in epithelial cells moving directionally in a physiological electric field.* Faseb j, 2002. **16**(8): p. 857-9.
200. Zhao, S., et al., *3D arrays for high throughput assay of cell migration and electrotaxis.* Cell Biol Int, 2013. **37**(9): p. 995-1002.
201. Zhao, S., et al., *ElectroTaxis-on-a-Chip (ETC): an integrated quantitative high-throughput screening platform for electrical field-directed cell migration.* Lab Chip, 2014. **14**(22): p. 4398-405.
202. Zhao, Z., et al., *Directed migration of human bone marrow mesenchymal stem cells in a physiological direct current electric field.* Eur Cell Mater, 2011. **22**: p. 344-58.

203. Zimolag, E., et al., *Electric field as a potential directional cue in homing of bone marrow-derived mesenchymal stem cells to cutaneous wounds.* Biochim Biophys Acta Mol Cell Res, 2017. **1864**(2): p. 267-279.
204. Minc, N. and F. Chang, *Electrical control of cell polarization in the fission yeast Schizosaccharomyces pombe.* Current Biology, 2010. **20**(8): p. 710-716.
205. Wang, X., et al., *Highly efficient microfluidic sorting device for synchronizing developmental stages of C. elegans based on deflecting electrotaxis.* Lab on a Chip, 2015. **15**(11): p. 2513-2521.
206. Sato, M.J., et al., *Input–output relationship in galvanotactic response of Dictyostelium cells.* Biosystems, 2007. **88**(3): p. 261-272.
207. Ren, X., et al., *Keratinocyte electrotaxis induced by physiological pulsed direct current electric fields.* Bioelectrochemistry, 2019. **127**: p. 113-124.
208. Saltukoglu, D., et al., *Spontaneous and electric field-controlled front-rear polarization of human keratinocytes.* Mol Biol Cell, 2015. **26**(24): p. 4373-86.
209. Zhang, G., et al., *Kindlin-1 Regulates Keratinocyte Electrotaxis.* J Invest Dermatol, 2016. **136**(11): p. 2229-2239.
210. Siwy, Z., M.E. Mycielska, and M.B. Djamgoz, *Statistical and fractal analyses of rat prostate cancer cell motility in a direct current electric field: comparison of strongly and weakly metastatic cells.* Eur Biophys J, 2003. **32**(1): p. 12-21.
211. Yang, H.Y., T.D. La, and R.R. Isseroff, *Utilizing custom-designed galvanotaxis chambers to study directional migration of prostate cells.* J Vis Exp, 2014(94).
212. Li, Y., et al., *Cell migration microfluidics for electrotaxis-based heterogeneity study of lung cancer cells.* Biosensors and Bioelectronics, 2017. **89**: p. 837-845.
213. Tai, G., et al., *Electrotaxis and Wound Healing: Experimental Methods to Study Electric Fields as a Directional Signal for Cell Migration.* Methods in molecular biology (Clifton, N.J.), 2009. **571**: p. 77-97.
214. Chang, P.C., et al., *Galvanotropic and galvanotaxic responses of corneal endothelial cells.* J Formos Med Assoc, 1996. **95**(8): p. 623-7.
215. Pavesi, A., et al., *Engineering a 3D microfluidic culture platform for tumor-treating field application.* Sci Rep, 2016. **6**: p. 26584.
216. Tzoneva, R., et al., *Angiogenic potential of endothelial and tumor cells seeded on gelatin-based hydrogels in response to electrical stimulations.* Clin Hemorheol Microcirc, 2016. **64**(4): p. 941-949.
217. Pu, J. and M. Zhao, *Golgi polarization in a strong electric field.* Journal of Cell Science, 2005. **118**(6): p. 1117.
218. Witek, M.A., et al., *Cell transport via electromigration in polymer-based microfluidic devices.* Lab on a Chip, 2004. **4**(5): p. 464-472.
219. McCloskey, M.A., Z.Y. Liu, and M.M. Poo, *Lateral electromigration and diffusion of Fc epsilon receptors on rat basophilic leukemia cells: effects of IgE binding.* Journal of Cell Biology, 1984. **99**(3): p. 778-787.
220. Nie, F.-Q., et al., *On-chip cell migration assay using microfluidic channels.* Biomaterials, 2007. **28**(27): p. 4017-4022.
221. Köhidai, L., *Chemotaxis as an Expression of Communication of Tetrahymena*, in *Biocommunication of Ciliates*. 2016, Springer. p. 65-82.
222. Boyden, S., *The chemotactic effect of mixtures of antibody and antigen on polymorphonuclear leucocytes.* The Journal of experimental medicine, 1962. **115**(3): p. 453-466.
223. Zigmond, S.H., *Ability of polymorphonuclear leukocytes to orient in gradients of chemotactic factors.* The Journal of cell biology, 1977. **75**(2): p. 606-616.
224. Toner, M. and D. Irimia, *Blood-on-a-chip.* Annu. Rev. Biomed. Eng., 2005. **7**: p. 77-103.

225. Li Jeon, N., et al., *Neutrophil chemotaxis in linear and complex gradients of interleukin-8 formed in a microfabricated device.* Nature Biotechnology, 2002. **20**(8): p. 826-830.
226. Irimia, D., D.A. Geba, and M. Toner, *Universal Microfluidic Gradient Generator.* Analytical Chemistry, 2006. **78**(10): p. 3472-3477.
227. Keenan, T.M. and A. Folch, *Biomolecular gradients in cell culture systems.* Lab on a Chip, 2008. **8**(1): p. 34-57.
228. Abhyankar, V.V., et al., *Characterization of a membrane-based gradient generator for use in cell-signaling studies.* Lab on a Chip, 2006. **6**(3): p. 389-393.
229. Frevert, C.W., et al., *Measurement of cell migration in response to an evolving radial chemokine gradient triggered by a microvalve.* Lab on a Chip, 2006. **6**(7): p. 849-856.
230. Sugiura, S., K. Hattori, and T. Kanamori, *Microfluidic Serial Dilution Cell-Based Assay for Analyzing Drug Dose Response over a Wide Concentration Range.* Analytical Chemistry, 2010. **82**(19): p. 8278-8282.
231. Lee, K., et al., *Microfluidic network-based combinatorial dilution device for high throughput screening and optimization.* Microfluidics and Nanofluidics, 2010. **8**(5): p. 677-685.
232. Liu, M.C., D. Ho, and Y.-C. Tai, *Monolithic fabrication of three-dimensional microfluidic networks for constructing cell culture array with an integrated combinatorial mixer.* Sensors and Actuators B: Chemical, 2008. **129**(2): p. 826-833.
233. Jeon, N.L., et al., *Generation of Solution and Surface Gradients Using Microfluidic Systems.* Langmuir, 2000. **16**(22): p. 8311-8316.
234. Liu, D., et al., *Parallel microfluidic networks for studying cellular response to chemical modulation.* Journal of Biotechnology, 2007. **131**(3): p. 286-292.
235. Ye, N., et al., *Cell-based high content screening using an integrated microfluidic device.* Lab on a Chip, 2007. **7**(12): p. 1696-1704.
236. Siyan, W., et al., *Application of microfluidic gradient chip in the analysis of lung cancer chemotherapy resistance.* Journal of Pharmaceutical and Biomedical Analysis, 2009. **49**(3): p. 806-810.
237. Walker, G.M., et al., *Effects of flow and diffusion on chemotaxis studies in a microfabricated gradient generator.* Lab on a Chip, 2005. **5**(6): p. 611-618.
238. Nguyen, N.-T., et al., *Design, fabrication and characterization of drug delivery systems based on lab-on-a-chip technology.* Advanced Drug Delivery Reviews, 2013. **65**(11): p. 1403-1419.
239. Jones, C.N., et al., *Microfluidic chambers for monitoring leukocyte trafficking and humanized nano-proresolving medicines interactions.* Proceedings of the National Academy of Sciences, 2012. **109**(50): p. 20560.
240. Hoang, A.N., et al., *Measuring neutrophil speed and directionality during chemotaxis, directly from a droplet of whole blood.* TECHNOLOGY, 2013. **01**(01): p. 49-57.
241. Jones, C.N., et al., *Microfluidic assay for precise measurements of mouse, rat, and human neutrophil chemotaxis in whole-blood droplets.* J Leukoc Biol, 2016. **100**(1): p. 241-7.
242. Jones, C.N., et al., *Spontaneous Neutrophil Migration Patterns during Sepsis after Major Burns.* PLOS ONE, 2014. **9**(12): p. e114509.
243. Ros, E., et al., *Single cell migration profiling on a microenvironmentally tunable hydrogel microstructure device that enables stem cell potency evaluation.* Lab on a Chip, 2020.
244. Allen, G.M., A. Mogilner, and J.A. Theriot, *Electrophoresis of cellular membrane components creates the directional cue guiding keratocyte galvanotaxis.* Curr Biol, 2013. **23**(7): p. 560-8.
245. Arocena, M., et al., *A time-lapse and quantitative modelling analysis of neural stem cell motion in the absence of directional cues and in electric fields.* Journal of Neuroscience Research, 2010. **88**(15): p. 3267-3274.

246. Siegrist, S.E. and C.Q. Doe, *Microtubule-induced cortical cell polarity.* Genes & development, 2007. **21**(5): p. 483-496.
247. Cortese, B., et al., *Influence of electrotaxis on cell behaviour.* Integrative Biology, 2014. **6**(9): p. 817-830.
248. Tai, G., et al., *Electrotaxis and wound healing: experimental methods to study electric fields as a directional signal for cell migration.* Methods Mol Biol, 2009. **571**: p. 77-97.
249. Lin, F. and E.C. Butcher, *T cell chemotaxis in a simple microfluidic device.* Lab on a Chip, 2006. **6**(11): p. 1462-1469.
250. Huang, C.-W., et al., *Electrotaxis of lung cancer cells in a multiple-electric-field chip.* Biosensors and Bioelectronics, 2009. **24**(12): p. 3510-3516.
251. Yang, K., et al., *A dual-docking microfluidic cell migration assay (D2-Chip) for testing neutrophil chemotaxis and the memory effect.* Integrative Biology, 2017. **9**(4): p. 303-312.
252. Cho, H., et al., *On-demand, competing gradient arrays for neutrophil chemotaxis.* Lab on a Chip, 2014. **14**(5): p. 972-978.
253. Moussavi-Harami, S.F., et al., *Simple microfluidic device for studying chemotaxis in response to dual gradients.* Biomedical Microdevices, 2015. **17**(3): p. 51.
254. Nuccitelli, R., *A Role for Endogenous Electric Fields in Wound Healing*, in *Current Topics in Developmental Biology*. 2003, Academic Press. p. 1-26.
255. Lakshmanan, S., et al., *Physical energy for drug delivery; poration, concentration and activation.* Advanced Drug Delivery Reviews, 2014. **71**: p. 98-114.
256. Geboers, B., et al., *High-Voltage Electrical Pulses in Oncology: Irreversible Electroporation, Electrochemotherapy, Gene Electrotransfer, Electrofusion, and Electroimmunotherapy.* Radiology, 2020: p. 192190.
257. Sriskandan, S. and D. Altmann, *The immunology of sepsis.* The Journal of Pathology, 2008. **214**(2): p. 211-223.
258. Hotchkiss, R.S., G. Monneret, and D. Payen, *Sepsis-induced immunosuppression: from cellular dysfunctions to immunotherapy.* Nature reviews. Immunology, 2013. **13**(12): p. 862-874.
259. Sersa, G., et al., *Electrochemotherapy in treatment of tumours.* European Journal of Surgical Oncology (EJSO), 2008. **34**(2): p. 232-240.
260. Wichtowski, M., et al., *Electrochemotherapy in Breast Cancer - Discussion of the Method and Literature Review.* Breast Care, 2017. **12**(6): p. 409-414.
261. Bourke, M.G., et al., *Effective treatment of intractable cutaneous metastases of breast cancer with electrochemotherapy: Ten-year audit of single centre experience.* Breast cancer research and treatment, 2017. **161**(2): p. 289-297.
262. Wichtowski, M., et al., *Electrochemotherapy in the Treatment of Breast Cancer Metastasis to the Skin and Subcutaneous Tissue - Multicenter Experience.* Oncology Research and Treatment, 2019. **42**(1-2): p. 47-51.
263. Potts, R.O. and M.L. Francoeur, *The influence of stratum corneum morphology on water permeability.* Journal of investigative dermatology, 1991. **96**(4): p. 495-499.
264. Shin, J.-H., H.Y. Seok, and Y.-C. Kim, *Biomedical applications of microneedles in therapeutics: recent advancements and implications in drug delivery AU - Rejinold, N. Sanoj.* Expert Opinion on Drug Delivery, 2016. **13**(1): p. 109-131.
265. Park, J., et al., *Enhanced Transdermal Drug Delivery by Sonophoresis and Simultaneous Application of Sonophoresis and Iontophoresis.* AAPS PharmSciTech, 2019. **20**(3): p. 96.
266. Wolinsky, J.B., Y.L. Colson, and M.W. Grinstaff, *Local drug delivery strategies for cancer treatment: Gels, nanoparticles, polymeric films, rods, and wafers.* Journal of Controlled Release, 2012. **159**(1): p. 14-26.

267. Eljarrat-Binstock, E. and A.J. Domb, *Iontophoresis: A non-invasive ocular drug delivery.* Journal of Controlled Release, 2006. **110**(3): p. 479-489.
268. Eljarrat-Binstock, E., et al., *In Vitro and In Vivo Evaluation of Carboplatin Delivery to the Eye Using Hydrogel-Iontophoresis.* Current Eye Research, 2008. **33**(3): p. 269-275.
269. Li, S.K., et al., *In vitro and in vivo comparisons of constant resistance AC iontophoresis and DC iontophoresis.* Journal of controlled release, 2003. **91**(3): p. 327-343.
270. Sylvestre, J.-P., R.H. Guy, and M.B. Delgado-Charro, *In Vitro Optimization of Dexamethasone Phosphate Delivery by Iontophoresis.* Physical Therapy, 2008. **88**(10): p. 1177-1185.
271. Jia, H.-Z. and X.-J. Peng, *Efficacy of iontophoresis-assisted epithelium-on corneal cross-linking for keratoconus.* International journal of ophthalmology, 2018. **11**(4): p. 687-694.
272. Jung, J.H., et al., *Ocular drug delivery targeted by iontophoresis in the suprachoroidal space using a microneedle.* Journal of Controlled Release, 2018. **277**: p. 14-22.
273. Loh, Q.L. and C. Choong, *Three-dimensional scaffolds for tissue engineering applications: role of porosity and pore size.* Tissue engineering. Part B, Reviews, 2013. **19**(6): p. 485-502.
274. Karuppuswamy, P., et al., *Functionalized hybrid nanofibers to mimic native ECM for tissue engineering applications.* Applied surface science, 2014. **322**: p. 162-168.
275. Dogra, P., et al., *Mathematical modeling in cancer nanomedicine: a review.* Biomedical Microdevices, 2019. **21**(2): p. 40.
276. Kim, M., R.J. Gillies, and K.A. Rejniak, *Current advances in mathematical modeling of anti-cancer drug penetration into tumor tissues.* Frontiers in oncology, 2013. **3**.
277. Sung, J.H., C. Kam, and M.L. Shuler, *A microfluidic device for a pharmacokinetic–pharmacodynamic (PK–PD) model on a chip.* Lab on a Chip, 2010. **10**(4): p. 446-455.
278. Calvert, A., et al., *Carboplatin dosage: prospective evaluation of a simple formula based on renal function.* Journal of Clinical Oncology, 1989. **7**(11): p. 1748-1756.
279. Kangwantas, K., et al., *The accuracy of carboplatin area under the curve (AUC) estimated by Calvert formula using Cockcroft-Gault formula and Thai eGFR in Thai cancer patients.* Journal of Clinical Oncology, 2016. **34**(15_suppl): p. e14017-e14017.
280. Lauritsen, J., et al., *Reliability of estimated glomerular filtration rate in patients treated with platinum containing therapy.* International journal of cancer, 2014. **135**(7): p. 1733-1739.
281. Edmondson, R., et al., *Three-Dimensional Cell Culture Systems and Their Applications in Drug Discovery and Cell-Based Biosensors.* Assay and Drug Development Technologies, 2014. **12**(4): p. 207-218.
282. Antoni, D., et al., *Three-dimensional cell culture: a breakthrough in vivo.* International journal of molecular sciences, 2015. **16**(3): p. 5517-5527.
283. Geckil, H., et al., *Engineering hydrogels as extracellular matrix mimics.* Nanomedicine (London, England), 2010. **5**(3): p. 469-484.
284. Huh, D., G.A. Hamilton, and D.E. Ingber, *From 3D cell culture to organs-on-chips.* Trends in Cell Biology, 2011. **21**(12): p. 745-754.
285. Caliari, S.R. and J.A. Burdick, *A practical guide to hydrogels for cell culture.* Nature methods, 2016. **13**(5): p. 405-414.
286. Halldorsson, S., et al., *Advantages and challenges of microfluidic cell culture in polydimethylsiloxane devices.* Biosensors and Bioelectronics, 2015. **63**: p. 218-231.
287. Vadivelu, R.K., et al., *Microfluidic Technology for the Generation of Cell Spheroids and Their Applications.* Micromachines, 2017. **8**(4): p. 94.
288. Achilli, T.-M., J. Meyer, and J.R. Morgan, *Advances in the formation, use and understanding of multi-cellular spheroids.* Expert opinion on biological therapy, 2012. **12**(10): p. 1347-1360.
289. Cui, X., Y. Hartanto, and H. Zhang, *Advances in multicellular spheroids formation.* Journal of the Royal Society, Interface, 2017. **14**(127): p. 20160877.

290. Venning, F.A., L. Wullkopf, and J.T. Erler, *Targeting ECM Disrupts Cancer Progression.* Frontiers in oncology, 2015. **5**: p. 224-224.
291. Masola, V., et al., *Heparanase: A Multitasking Protein Involved in Extracellular Matrix (ECM) Remodeling and Intracellular Events.* Cells, 2018. **7**(12): p. 236.
292. Gattazzo, F., A. Urciuolo, and P. Bonaldo, *Extracellular matrix: A dynamic microenvironment for stem cell niche.* Biochimica et Biophysica Acta (BBA) - General Subjects, 2014. **1840**(8): p. 2506-2519.
293. Jhala, D. and R. Vasita, *A Review on Extracellular Matrix Mimicking Strategies for an Artificial Stem Cell Niche.* Polymer Reviews, 2015. **55**(4): p. 561-595.
294. Chai, Q., Y. Jiao, and X. Yu, *Hydrogels for biomedical applications: their characteristics and the mechanisms behind them.* Gels, 2017. **3**(1): p. 6.
295. Chirani, N., et al., *History and applications of hydrogels.* Journal of biomedical sciences, 2015. **4**(2).
296. Kim, M., et al., *Heparin-based hydrogel as a matrix for encapsulation and cultivation of primary hepatocytes.* Biomaterials, 2010. **31**(13): p. 3596-3603.
297. Senthebane, D.A., et al., *The Role of Tumor Microenvironment in Chemoresistance: To Survive, Keep Your Enemies Closer.* International journal of molecular sciences, 2017. **18**(7): p. 1586.
298. Davalos, R.V., L. Mir, and B. Rubinsky, *Tissue ablation with irreversible electroporation.* Annals of biomedical engineering, 2005. **33**(2): p. 223.
299. Edd, J.F., et al., *In vivo results of a new focal tissue ablation technique: irreversible electroporation.* IEEE Transactions on Biomedical Engineering, 2006. **53**(7): p. 1409-1415.
300. Morshed, B.I., M. Shams, and T. Mussivand, *Investigation of low-voltage pulse parameters on electroporation and electrical lysis using a microfluidic device with interdigitated electrodes.* IEEE Transactions on biomedical engineering, 2014. **61**(3): p. 871-882.
301. Ionescu-Zanetti, C., A. Blatz, and M. Khine, *Electrophoresis-assisted single-cell electroporation for efficient intracellular delivery.* Biomedical microdevices, 2008. **10**(1): p. 113-116.
302. Murdan, S., *Electro-responsive drug delivery from hydrogels.* Journal of Controlled Release, 2003. **92**(1): p. 1-17.
303. Curcio, M., et al., *On demand delivery of ionic drugs from electro-responsive CNT hybrid films.* RSC Advances, 2015. **5**(56): p. 44902-44911.
304. Fujii, T., *PDMS-based microfluidic devices for biomedical applications.* Microelectronic Engineering, 2002. **61**: p. 907-914.
305. Duffy, D.C., et al., *Rapid prototyping of microfluidic systems in poly (dimethylsiloxane).* Analytical chemistry, 1998. **70**(23): p. 4974-4984.
306. Bird, R.B., W.E. Stewart, and E.N. Lightfoot, *Transport phenomena*. 2007: John Wiley & Sons.
307. Geankoplis, C.J., *Transport processes and separation process principles:(includes unit operations)*. 2003: Prentice Hall Professional Technical Reference.
308. Johansson, L., C. Elvingson, and J.E. Loefroth, *Diffusion and interaction in gels and solutions. 3. Theoretical results on the obstruction effect.* Macromolecules, 1991. **24**(22): p. 6024-6029.
309. Boyce, W.E., R.C. DiPrima, and D.B. Meade, *Elementary Differential Equations and Boundary Value Problems, Loose-Leaf Print Companion*. 2017: John Wiley & Sons.
310. Pampel, A., D. Michel, and R. Reszka, *Pulsed field gradient MAS-NMR studies of the mobility of carboplatin in cubic liquid-crystalline phases.* Chemical Physics Letters, 2002. **357**(1): p. 131-136.
311. Gust, R. and B. Schnurr, *Investigations on the stability of carboplatin infusion solutions.* Monatshefte für Chemie/Chemical Monthly, 1999. **130**(5): p. 637-644.
312. Binks, S.P. and M. Dobrota, *Kinetics and mechanism of uptake of platinum-based pharmaceuticals by the rat small intestine.* Biochemical Pharmacology, 1990. **40**(6): p. 1329-1336.

313. Lasdon, L.S., R.L. Fox, and M.W. Ratner, *Nonlinear optimization using the generalized reduced gradient method.* Revue française d'automatique, informatique, recherche opérationnelle. Recherche opérationnelle, 1974. **8**(V3): p. 73-103.
314. Santiago, J.-L., A. Martilli, and F. Martin, *On Dry Deposition Modelling of Atmospheric Pollutants on Vegetation at the Microscale: Application to the Impact of Street Vegetation on Air Quality.* Boundary-Layer Meteorology, 2017. **162**(3): p. 451-474.
315. Soni, M., et al., *A performance evaluation of WRF model using different physical parameterization scheme during winter season over a semi-arid region, India.* International Journal of Earth and Atmospheric Science, 2014. **1**(3): p. 104-114.
316. Brust-Mascher, I. and W.W. Webb, *Calcium waves induced by large voltage pulses in fish keratocytes.* Biophysical journal, 1998. **75**(4): p. 1669-1678.
317. Cortese, B., et al., *Influence of electrotaxis on cell behaviour.* Integrative Biology, 2014. **6**(9): p. 817-830.
318. McCaig, C.D., et al., *Controlling cell behavior electrically: current views and future potential.* Physiological reviews, 2005. **85**(3): p. 943-978.
319. Robinson, K.R. and M.A. Messerli, *Left/right, up/down: the role of endogenous electrical fields as directional signals in development, repair and invasion.* Bioessays, 2003. **25**(8): p. 759-766.
320. Nuccitelli, R., *Physiological electric fields can influence cell motility, growth, and polarity*, in *Advances in Molecular and Cell Biology*. 1988, Elsevier. p. 213-233.
321. Dewald, B. and M. Baggiolini, *Activation of NADPH oxidase in human neutrophils. Synergism between fMLP and the neutrophil products PAF and LTB4.* Biochemical and Biophysical Research Communications, 1985. **128**(1): p. 297-304.
322. Chen, L., et al., *Negative Regulation of Bacterial fMLP-induced Pro-inflammatory Cytokine Gene Ex-pression via MKP-1-dependent Inhibition of NF-κB. J Cell Signal 4: 201. doi: 10.4172/2576-1471.1000201 J Cell Signal, an open access journal to prevent overactive inflammatory responses during bacterial infection. Interestingly, dexamethasone, a glucocorticoid used clinically as an anti-inflammatory agent, inhibited fMLP-induced TNFα in monocytes through increasing MKP-1 expression, which occurs at the level of IKK via the glucocorticoid receptor*. 2019, These studies provide new insight into the molecular mechanism of ….
323. Nierhaus, A., et al., *The Effects of Ex Vivo Administration of Granulocyte-Macrophage Colony-Stimulating Factor and Endotoxin on Cytokine Release of Whole Blood Are Determined by Priming Conditions.* BioMed research international, 2017. **2017**.
324. Simeunovic, A. and D.J. Hoelzle. *Coupled Dynamics of Material Delivery and Robotic Manipulator Axes in Endoscopic Additive Manufacturing*. in *2019 American Control Conference (ACC)*. 2019.
325. Adib, A.A. and D. Hoelzle. *Hybrid System Model of Microextrusion-Based Direct-Write Additive Manufacturing*. in *2019 American Control Conference (ACC)*. 2019.
326. Bloomquist, C.J., et al., *Controlling release from 3D printed medical devices using CLIP and drug-loaded liquid resins.* Journal of Controlled Release, 2018. **278**: p. 9-23.
327. Oh, H.J., et al., *3D Printed Absorber for Capturing Chemotherapy Drugs before They Spread through the Body.* ACS Central Science, 2019. **5**(3): p. 419-427.
328. Chueh, B.-h., et al., *Leakage-Free Bonding of Porous Membranes into Layered Microfluidic Array Systems.* Analytical Chemistry, 2007. **79**(9): p. 3504-3508.
329. Byrne, J.D., et al., *Local iontophoretic administration of cytotoxic therapies to solid tumors.* Science translational medicine, 2015. **7**(273): p. 273ra14-273ra14.
330. Byrne, J.D., et al., *Iontophoretic device delivery for the localized treatment of pancreatic ductal adenocarcinoma.* Proceedings of the National Academy of Sciences, 2016. **113**(8): p. 2200.